INNOVATIVE RESEARCH IN NATURAL SCIENCE AND MATHEMATICS

Editor
Assoc Prof. Ali ÖZDEMİR, Ph.D,

DUVAR

INNOVATIVE RESEARCH IN NATURAL SCIENCE AND MATHEMATICS

Editor

Assoc Prof. Ali ÖZDEMİR, Ph.D,

Innovative Research in Natural Science and Mathematics
Editor: Assoc. Prof. Ali ÖZDEMİR, Ph.D,

Editor in chief: Berkan Balpetek
Cover and Page Design: Duvar Design
Printing : AUGUST-2023
Publisher Certificate No: 49837
ISBN:978-625-6507-13-5

© Duvar Publishing
853 Sokak No:13 P.10 Kemeraltı-Konak/Izmir/ Turkey
Phone: 0 232 484 88 68

www.duvaryayinlari.com
duvarkitabevi@gmail.com

TABLE OF CONTENTS

Chapter 1

On the Actions of Associative Algebras

Ummahan EGE ARSLAN[1]

[1] 1Department of Mathematics and Computer Science, Faculty of Science, Eskisehir Osmangazi University, Eskisehir, Turkiye

ABSTARCT

Introduction

The idea of something acting on something else has many different variations. They are all related to one another. A group action on a set is given by a group homomorphism of a given group into the group of transformations of the set, namely the symmetry group. Similarly, a group action on a mathematical structure is a group homomorphism of a group into the automorphism group of the algebraic structure. It is said that the group acts on the algebraic structure. Since an automorphism group provides the description of an action, any group G can operate on itself by using the group homomorphism G→Aut(G). Other algebraic contexts may require more than only automorphism structure to provide an action. Aut(C) is not an associative algebra for the associative algebra C. The multiplication algebra M(C) of a commutative algebra C and the bimultiplication algebra Bim(C) of an associative algebra C, defined by Mac Lane [Mac Lane 1949], will fulfill the function of an automorphism group in the context of commutative algebra and associative algebra,respectively.

Bimultiplication algebra

We recall the structure of the R-algebra of bimultipliers of C, Bim(C) [Mac Lane 1958,Lue 1968]. Bim(C) consists of all pairs (γ,δ) of R-linear mappings $\gamma,\delta : C \to C$ such that

$$\gamma(cc') = \gamma(c)\cdot c', \delta(cc') = c\cdot\delta c' \text{ and } c\cdot\gamma c' = \delta(c)\cdot c'.$$

Suppose that $\mathrm{Ann}(C) = 0$ or $C^2 = C$. Then $\mathrm{Bim}(C)$ acts on C by

$$\begin{array}{rcll} \mathrm{Bim}(C)\times C & \to & C; & ((\gamma,\delta),c) \mapsto \gamma(c), \\ C\times \mathrm{Bim}(C) & \to & C; & (c,(\gamma,\delta)) \mapsto \delta(c) \end{array}$$

and there is a

$$\begin{array}{rccc} \mu : & C & \longrightarrow & \mathrm{Bim}(C) \\ & c & \longmapsto & (\gamma_c,\delta_c) \end{array}$$

with

$$\gamma_c(x) = c\cdot x \qquad \text{and} \qquad \delta_c(x) = x\cdot c.$$

If C is a commutative R-algebra and $(\gamma,\delta) \in \mathrm{Bim}(C)$, then $\gamma = \delta$. This is because for every $x \in C$:

$$\begin{array}{rcl} x\cdot\delta(c) & = & \delta(c)\cdot x = c\cdot\gamma(x) = \gamma(x)\cdot c \\ & = & \gamma(xc) = \gamma(cx) = \gamma(c)\cdot x = x\cdot\gamma(c). \end{array}$$

Thus $\mathrm{Bim}(C)$ may be identified with the R-algebra $\mathscr{M}(C)$ of multipliers of C. Recall that a multiplier of C is a linear mapping $\lambda : C \longrightarrow C$ such that for all $c, c' \in C$

$$\lambda(cc') = \lambda(c)c'.$$

Also $\mathscr{M}(C)$ is commutative as

$$\lambda'\lambda(xc) = \lambda'(\lambda(x)c) = \lambda(x)\lambda'(c) = \lambda'(c)\lambda(x) = \lambda\lambda'(cx) = \lambda\lambda'(xc)$$

for any $x \in C$.

Bim(C) has an associative algebra structure with following operations:

$(\gamma,\sigma)+(\gamma',\sigma') = (\gamma+\gamma',\sigma+\sigma')$

$(\gamma,\sigma)\circ(\gamma',\sigma') = (\gamma\circ\gamma',\sigma'\circ\sigma)$

$k(\gamma,\sigma) = (k\gamma,k\sigma)$

for $(\gamma,\sigma),(\gamma',\sigma') \in \text{Bim}(G)$, $k \in \mathbf{k}$. [Lavendhomme, Lucas, 1996].

Let $M^2 = M$ or $\text{Ann}(M) = 0$, M and P be an associative k-algebras. The action P on M can also be obtained by the help of $P \to \text{Bim}(M)$ algebra homomorphism. If we consider the following algebra morphisms, then we get the axioms for the action of an associative algebra on the other:

$$\begin{array}{rccl} \phi: & P & \to & \text{Bim}(M) \\ & p & \mapsto & \phi_p = (\gamma_{p,}\sigma_p) \end{array}$$

where $\gamma_{p,}\sigma_p : M \to M, \gamma_p(m) = p\cdot m, \sigma_p(m) = m\cdot p$.

i) Since ϕ is a k-algebra morphism, we get $k\phi(p) = \phi(kp)$. By the following equations

$$\begin{array}{rcl} k\phi(p) & = & k(\gamma_{p,}\sigma_p) \\ & = & (k\gamma_{p,}k\sigma_p) \end{array} \qquad \phi(kp) = (\gamma_{kp},\sigma_{kp})$$

and $k\gamma_p(m) = k(p\cdot m)$ ve $\gamma_{kp}(m) = (kp)\cdot m$, we have

$$k(p\cdot m) = (kp)\cdot m$$

Similarly, by the equations $k\sigma_p(m) = k(m\cdot p)$ and $\sigma_{kp}(m) = m\cdot(kp)$, we have one of the associative action conditions,

$$k(m\cdot p) = m\cdot(kp).$$

Also, since the below equations

$k\phi_p(m) = \phi_p(km)$,

$$\begin{array}{rcl} k\phi_p(m) & = & k(\gamma_p(m),\sigma_p(m)) \\ & = & (k\gamma_p(m),k\sigma_p(m)) \end{array} \qquad \phi_p(km) = (\gamma_p(km),\sigma_p(km))$$

we get $k\gamma_p(m) = k(p\cdot m)$ and $\gamma_p(km) = p\cdot(km)$

That is, the equation

$$k(p\cdot m) = p\cdot(km)$$

is satisfied. Similarly, because of

$k\sigma_p(m) = k(m\cdot p)$ and $\sigma_p(km) = (km)\cdot p$, the equations

$$k(m\cdot p) = (km)\cdot p = m\cdot(kp)$$

are valid.

ii) By using the definition of some necessary function and ϕ being a k-algebra morphism, we get following equations:

$$\begin{array}{rcl}\phi(p+p') & = & (\gamma_{p+p'},\sigma_{p+p'})\end{array} \qquad \begin{array}{rcl}\phi(p)+\phi(p') & = & (\gamma_p,\sigma_p)+(\gamma_{p'},\sigma_{p'}) \\ & = & (\gamma_p+\gamma_{p'},\sigma_p+\sigma_{p'})\end{array}$$

$\gamma_{p+p'}(m) = (p+p')\cdot m$ and $\gamma_p(m)+\gamma_{p'}(m) = p\cdot m + p'\cdot m$.
So,

$$(p+p')\cdot m = p\cdot m + p'\cdot m$$

Similarly, we get
$\sigma_{p+p'}(m) = m\cdot(p+p')$, $\sigma_p(m)+\sigma_{p'}(m) = m\cdot p + m\cdot p'$ and so it seems that

$$m\cdot(p+p') = m\cdot p + m\cdot p'.$$

Also,
$\sigma_{pp'}(m) = m\cdot(pp')$, $(\sigma_{p'}\circ\sigma_p)(m) = \sigma'_p(m\cdot p) = (m\cdot p)\cdot p'$ and so

$$m\cdot(pp') = (m\cdot p)\cdot p'.$$

iii) Because of being ϕ_p k-algebra morphism, we write

$$\phi_p(m+m') = \phi_p(m)+\phi_p(m').$$

By following equations

$$\phi_p(m+m') = (\gamma_p(m+m'),\sigma_p(m+m'))$$

$$\begin{array}{rcl}\phi_p(m)+\phi_p(m') & = & (\gamma_p(m),\sigma_p(m))+(\gamma_p(m'),\sigma_p(m')) \\ & = & (\gamma_p(m)+\gamma_p(m'),\sigma_p(m)+\sigma_p(m')),\end{array}$$

we get $\gamma_p(m+m') = p\cdot(m+m')$, $\gamma_p(m)+\gamma_p(m') = p\cdot m + p\cdot m'$and so it is valid the below equation

$$p\cdot(m+m') = p\cdot m + p\cdot m'.$$

Similarly, by these equations $\sigma_p(m+m') = (m+m')\cdot p$ and $\gamma_p(m'),\sigma_p(m') = m\cdot p + m'\cdot p$, we have

$$(m+m')\cdot p = p\cdot m + p\cdot m'.$$

iv) Since $(\gamma_p,\sigma_p)\in Bim(M)$, we have

$$\begin{array}{rcl}\gamma_p(mm') & = & (\gamma_p(m))m' \\ p\cdot(mm') & = & (p\cdot m)m'\end{array} \text{ and } \begin{array}{rcl}\sigma_p(mm') & = & m(\sigma_p(m')) \\ (mm')\cdot p & = & m(m'\cdot p).\end{array}$$

v) Since ϕ is a k-algebra homomorphism, we write

$$\phi(pp') = \phi(p)\circ\phi(p').$$

Regarding the definition of $\phi, \gamma_{pp'}, \sigma_{pp'}$ and operations, we write the below equations:

$$\phi(pp') = (\gamma_{pp'}, \sigma_{pp'}) \qquad \begin{aligned} \phi(p) \circ \phi(p') &= (\gamma_p, \sigma_p) \circ (\gamma_{p'}, \sigma_{p'}) \\ &= (\gamma_p \circ \gamma_{p'}, \sigma_{p'} \circ \sigma_p) \end{aligned}$$

$\gamma_{pp'}(m) = (pp') \cdot m$ and $(\gamma_p \circ \gamma_{p'})(m) = \gamma_p(p' \cdot m) = p \cdot (p' \cdot m)$. So, we get

$$(pp') \cdot m = p \cdot (p' \cdot m).$$

Analogously, we see that equations

$\sigma_{pp'}(m) = m \cdot (pp')$ and $(\sigma_{p'} \circ \sigma_p)(m) = \sigma'_p(m \cdot p) = (m \cdot p) \cdot p'$ are valid. Thus the desired equation is obtained as

$$m \cdot (pp') = (m \cdot p) \cdot p'.$$

vi) It is enough to get the equation

$$\gamma_p(\sigma_{p'}(m)) = \sigma_{p'}(\gamma_p(m))$$

for the equation $p \cdot (m \cdot p') = (p \cdot m) \cdot p'$.

Since $M^2 = M$, we can take $m = m_1 m_2$ for $m, m_1, m_2 \in M$. Thus, we get following equations:

$$\begin{aligned} \gamma_p(\sigma_{p'}(m_1 m_2)) &= \gamma_p((m_1 m_2) \cdot p') \\ &= \gamma_p(m_1(m_2 \cdot p')) \\ &= p \cdot (m_1(m_2 \cdot p')) \\ &= (p \cdot m_1)(m_2 \cdot p') \\ \sigma_{p'}(\gamma_p(m_1 m_2)) &= \sigma_{p'}(p \cdot (m_1 m_2)) \\ &= \sigma_{p'}((p \cdot m_1) m_2) \\ &= ((p \cdot m_1) m_2) \cdot p' \\ &= (p \cdot m_1)(m_2 \cdot p'). \end{aligned}$$

vii) It is clear that

$$\begin{aligned} m\gamma_p(m') &= \sigma_p(m) m' \\ m(p \cdot m') &= (m \cdot p) m' \end{aligned}$$

for $(\gamma_p, \sigma_p) \in Bim(M)$.

2-Dimensional Algebras: Crossed Modules of Associative Algebras

One method that can be viewed as a generalization of algebras to a higher dimension is the use of crossed modules of associative algebras.

In Whitehead's work [Whitehead,1949] on the algebraic structure of relative homotopy groups, crossed modules are first referenced in the literature. He presented the notion of crossed module as a model for 2-types. This concept has created a wide field of study for scientists over the years.

The notion of crossed modules in associative algebras is defined by Dedecker and Lue in [Dedecker, Lue 1966].

We recall the definition of a crossed module in associative algebras [Ellis 1988].

A crossed module in associative k-algebras is a morphism from a G-algebra C to a k-algebra G, $\delta : C \longrightarrow G$, with two-sided actions of G on C satisfying

CM1) $\delta(g \cdot c) = g\delta(c)$ and $\delta(c \cdot g) = \delta(c)g$,

CM2) $\delta c \cdot c' = cc'$ and $c \cdot \delta c' = cc'$

for all $c \in C, g \in G$. It is denoted by (C, G, δ).

The following are some standard examples of crossed modules in associative algebras:

i. An inclusion map I $\longrightarrow$ G is a crossed module, where I is any two-sided ideal in G. On the other hand, let δ : C $\longrightarrow$ G be any crossed module. Then, we get that δ(C) is a two sided ideal in G by CM1.

ii. Any G-bimodule M has a G-algebra structure with zero multiplication. Thus, we get the crossed module 0 : M $\longrightarrow$ G, 0(m) = 0. Conversely, the kernel of crossed module δ : N $\longrightarrow$ G is an G/δ(N)-bimodule.

According to above examples, the concept of crossed modules in associative algebras is a generalisation the concepts both of a two-sided ideal and that of a bimodule over an algebra. Furthermore, any associative algebra is also considered as a crossed modules by identity map

$$Id : G \longrightarrow G.$$

We get the crossed module A $\longrightarrow$ Bim(A) as a two-dimensional associative algebra via an associative algebra A.

Proposition: Let G be a k-algebra such that Ann $(G) = 0$ or $G^2 = G$. Then, $(\gamma, \sigma) : G \longrightarrow Bim(G)$ defined by $(\gamma, \sigma)(g) = (\gamma'_g, \sigma'_g)$ is a crossed module where $\gamma'_g(g') = gg'$and $\sigma'_g(g') = g'g, g, g' \in G$.

Proof: See [Ege Arslan, Hurmetli, 2021] for details.

Generalization of the concept of bimultiplication will be given the following section:

An Application: Bimultiplication of Crossed Modules

Let (C, G, δ) be a crossed module on associative algebras. A morphism

$$(f, h) = ((\gamma, \sigma), (\gamma', \sigma')) : (C, G, \delta) \longrightarrow (C, G, \delta)$$

satisfying following conditions is called bimultiplier of (C, G, δ) and the set of all this morphism is denoted as $Bim(C, G, \delta)$:

i) $(f = (\gamma, \sigma) : C \longrightarrow C) \in Bim(C)$ and
$(h = (\gamma', \sigma') : G \longrightarrow G) \in Bim(G)$

ii) $h\delta = \delta f$ $(\gamma'\delta = \delta\gamma,\ \sigma'\delta = \delta\sigma)$ and

iii)

$$\begin{aligned}
&\gamma(g\cdot c) = \gamma'(g)\cdot c\\
&\gamma(c\cdot g) = \gamma(c)\cdot g\\
&\sigma(g\cdot c) = g\cdot\sigma(c)\\
&\sigma(c\cdot g) = c\cdot\sigma'(g)\\
&g\cdot\gamma(c) = \sigma'(g)\cdot c\\
&\sigma(c)\cdot g = c\cdot\gamma'(g)
\end{aligned}$$

for all $g \in G$ ve $c \in C$.

Proposition: The set $Bim(C,G,\delta)$ has an associative K-algebra structure with following operations:

$+)$ $(f,h)+(\overline{f},\overline{h}) = (f+\bar{f},h+\overline{h})$

$\cdot)$ $k(f,h) = (kf,kh)$

$\circ)$ $(f,h)\circ(\overline{f},\overline{h}) = (f\bar{f},\overline{h}h) = (f\circ\overline{f},\overline{h}\circ h)$

where $(f,h) = ((\gamma,\sigma),(\gamma',\sigma'))$ and $(\overline{f},\overline{h}) = ((\overline{\gamma},\overline{\sigma}),(\overline{\gamma}',\overline{\sigma}'))$

Proof: See [Hurmetli 2016] for details.

The set of all bimultipliers of crossed modules of associative algebras plays a fundamental role in the construction of various contents, such as the actor-crossed module, the action of crossed modules, the actor tower of crossed modules, and the semi-direct product of crossed modules,the split extension classifier of a crossed module. For more information on these contents, readers are recommended to consult sources [Ege Arslan, Hurmetli, 2021],[Hurmetli 2016] and [Boyacı et al 2015]. Additionally, it can be found in [Arvasi, Ege 2003] the commutative algebra version of similar structures.

Kaynaklar

1. Z. Arvasi, U. Ege, Annihilators, Multipliers and Crossed Modules, Applied Categorical Structures, 11,(2003) 487-506.

2. Y. Boyacı, J. M. Casas, T. Datuashvili, E. O. Uslu, Actions in Modified Categories of Interest with Application Crossed Modules, Theory and Applications of Categories 30(25) (2015) 882–908.

3. P. Dedecker, A. S. -T. Lue, A Nonabelian Two-Dimensional Cohomology for Associative Algebras, Bulletin of the American Mathematical Society 72(6) (1966) 1044–1050.

4. U. Ege Arslan, S. Hurmetli, 2021, Bimultiplications and Annihilators of Crossed Modules in Associative Algebras, 35, 72-90.

5. G. J. Ellis, Higher Dimensional Crossed Modules of Algebras, Journal of Pure and Applied Algebra 52(3) (1988) 277–282.

6. S. Hurmetli, Bimultiplication of Crossed Modules, PhD Dissertation, Eskisehir Osmangazi University, (2016) Eskisehir, Turkey.

7. S. Mac Lane, Extensions and Obstructions for Rings, Illinois Journal of Mathematics 121 (1958) 316–345.

8. R. Lavendhomme, Th.Lucas, 1996, On Modules and Crossed Modules, Journal of Algebra, 179, 936-963.

9. A. S. -T. Lue, Non-Abelian cohomology of Associative Algebras, The Quarterly Journal of Mathematics 19(1) (1968) 159–180

10. J. H. C. Whitehead, Combinatorial Homotopy I, Bulletin of the American Mathematical Society 55 (1949) 231–245.

Chapter 2

Directional Bertrand Curves in Minkowski Space

Gamze TARIM KANDİLCİ[1]

Cumali EKİCİ[2]

Mustafa DEDE[3]

1 Öğr. Gör.; Eskişehir Osmangazi Üniversitesi Fen Bilimleri Enstitüsü Matematik ve Bilgisayar Bilimleri ABD. gamze.kandilci@ogu.edu.tr ORCID No:0000-0003-4056-4751

2 Prof. Dr.; Eskişehir Osmangazi Üniversitesi, Fen Fakültesi, Matematik ve Bilgisayar Bilimleri Bölümü. cekici@ogu.edu.tr ORCID No:0000-0002-3247-5727

3 Prof. Dr.; Kilis 7 Aralık Üniversitesi Fen Fakültesi, Matematik Bölümü. mustafadede@kilis.edu.tr ORCID No: 0000-0003-2652-637X

SUMMARY

This study aims to investigate pairs of directional Bertrand curves in Minkowski space using the q-frame, which is known for its similarity to the Frenet frame. It is known that the Bertrand curve is one of the distinguishing features of the linear relation between curvature and torsion. In this paper, we first generalized the derivative equations of the q-frame for non-null curves in Minkowski 3-space. In addition, the Frenet frame of non-null curves and the relations between the q-frame and the curvatures of these frames are found. Also, the relations between the q-frame and q-curvatures of a pair of non-null directional Bertrand curves are obtained.

Keywords: q-frame, Bertrand Curves, Frenet frame, Minkowski space.

1. Introduction

In differential geometry, parallel plane curves and surfaces are a well-known Notion (Kuhnel, 1999, Çöken et al. 2008, Dede et al., 2015). The similar relationships can be constructed between space curves (Matsuda & Yorozu, 2003, Izumiya & Takeuchi, 2002, Ekmekci & Ilarslan, 2001). Saint Venant posed the query in 1845, "Is the principal normal of a curve the principal normal of another's on the surface produced by the principal normal of the given one?" (Saint Venant, 1845). In a paper that was released in 1850, Bertrand provided an answer to this query (Bertrand, 1850). He showed that a linear relationship between the first and second curvatures of the given original curve should be calculated with constant coefficients; this condition is both necessary and sufficient for the existence of such a second curve. In other words, if we use k_1 and k_2 to represent the first and second curvatures of a given curve, respectively, we get $\lambda k_1 + \mu k_2 = 1, \lambda, \mu \in \mathbb{R}$ (Tuncer & Ünal, 2012). Numerous studies on Bertrand curves have been published in the Computer-Aided Geometric Design (CAGD) field (Ravani & Ku, 1991, Papaioannou & Kiritsis, 1985). Moreover, numerous academics have investigated Bertrand curves and their characterizations in Euclidean space, Minkowski 3-space, and Minkowski space-time (Ekmekci & İlarslan, 2001, Choi et al., 2012, Öztekin & Bektaş, 2010, Ilarslan & Kılıç, 2017, Balgetir et al., 2004, Balgetir et al., 2004a, Gök et al., 2014, Jin, 2008, Kahraman et al., 2014, Whittemore, 1940).

The Frenet frame has the following definitions:

$$\boldsymbol{t} = \frac{\alpha'}{||\alpha'||}, \boldsymbol{b} = \frac{\alpha' \wedge \alpha''}{||\alpha' \wedge \alpha''||}, \quad \boldsymbol{n} = \boldsymbol{b} \wedge \boldsymbol{t} \tag{1}$$

The definitions of curvature $\kappa = k_1$ and torsion $\tau = k_2$ are as follows:

$$\kappa = \frac{||\alpha' \wedge \alpha''||}{||\alpha'||^3}, \qquad \tau = \frac{\det(\alpha', \alpha'', \alpha''')}{||\alpha' \wedge \alpha''||^2}.$$

Following is a definition of the well-known Frenet formula:

$$\begin{bmatrix} \boldsymbol{t}' \\ \boldsymbol{n}' \\ \boldsymbol{b}' \end{bmatrix} = v \begin{bmatrix} 0 & k_1 & 0 \\ -k_1 & 0 & k_2 \\ 0 & -k_2 & 0 \end{bmatrix} \begin{bmatrix} \boldsymbol{t} \\ \boldsymbol{n} \\ \boldsymbol{b} \end{bmatrix} \tag{2}$$

where $v = ||\alpha'(s)||$. Frenet frames do, however, have a number of shortcomings in practical use. Frenet frame, for instance, is undefinable anywhere the curvature disappears. Additionally, the Frenet frame's primary flaw is an unfavorable

rotation about the tangent vector (Bloomenthal, 1990). In order to better fit applications, a new frame was created by Bishop (Bishop, 1975) for a space curve. However, it is generally known that calculating Bishop frames is a difficult operation (Wang et al., 2008). The quasi-normal vector of a space curve was first presented by Coquillart in order to construct the 3D curve offset (Coquillart, 1987). The q-frame was subsequently introduced by Dede et al. (2015) and (2015a) using a space curve and a quasi-normal vector. The three orthonormal vectors that make up the q-frame for a particular space curve $\alpha(s)$ are the unit tangent vector **t**, the quasi-normal vector $\mathbf{n}_q$, and the quasi-binormal vector $\mathbf{b}_q$. The q-frame $\{\boldsymbol{t}, \mathbf{n}_q, \boldsymbol{b}_q, \boldsymbol{k}\}$ is supplied by

$$\boldsymbol{t} = \frac{\alpha'}{||\alpha'||}, \mathbf{n}_q = \frac{\boldsymbol{t} \wedge \boldsymbol{k}}{||\boldsymbol{t} \wedge \boldsymbol{k}||}, \quad \mathbf{b}_q = \boldsymbol{t} \wedge \mathbf{n}_q \tag{3}$$

where **k** is the projection vector, according to Dede et al. (2015).

Two vectors $\mathbf{u} = (u_1, u_2, u_3)$ and $\mathbf{v} = (v_1, v_2, v_3) \in \mathbb{R}_1^3$ have a dot product and cross product that are specified as

$$< u, v >= u_1 v_1 + u_2 v_2 - u_3 v_3 \tag{4}$$

and

$$\mathbf{u} \wedge \mathbf{v} = (u_3 v_2 - u_2 v_3, u_1 v_3 - u_3 v_1, u_1 v_2 - u_2 v_1) \tag{5}$$

in the three-dimensional Minkowski space $\mathbb{R}_1^3$,

where $\boldsymbol{e}_1 \wedge \boldsymbol{e}_2 = \boldsymbol{e}_3, \boldsymbol{e}_2 \wedge \boldsymbol{e}_3 = -\boldsymbol{e}_1, \boldsymbol{e}_3 \wedge \boldsymbol{e}_1 = -\boldsymbol{e}_2$ respectively (Akutagawa & Nishikawa, 1990). $\mathbf{u} \wedge \mathbf{v}$ is a spacelike vector if **u** and **v** are timelike vectors (Oneill, 1983).

The **u** vector's norm is defined by the expression

$$\|\mathbf{u}\| = \sqrt{|< u, u >|}. \tag{6}$$

If $< \mathbf{u}, \mathbf{u} >> 0$, $< \mathbf{u}, \mathbf{u} >= 0$ and $\mathbf{u} \neq 0, < \mathbf{u}, \mathbf{u} >< 0$, respectively, a Lorentzian vector **u** is said to be spacelike, lightlike, or timelike. The vector **u** =0 in particular is spacelike.

If all of the velocity vectors $\alpha'(s)$ of an arbitrary curve, $\alpha(s)$ in $\mathbb{R}_1^3$, are, respectively, spacelike, timelike, or null (lightlike), then the curve can be locally classified as spacelike, timelike, or null (O'Neill, 1983). A null curve α is parameterized by pseudo-arc s if $\langle \alpha''(s), \alpha''(s) \rangle = 1$. However, if

$\langle \alpha'(s), \alpha'(s) \rangle = \pm 1$, then the arc-length parameter s is parameterized for a non-null curve (Bonnor, 1969, Otsuki, 1961).
Then, a curve's Frenet formulae can be represented as ,

$$\begin{bmatrix} \boldsymbol{t}' \\ \boldsymbol{n}' \\ \boldsymbol{b}' \end{bmatrix} = \begin{bmatrix} 0 & \kappa & 0 \\ -\varepsilon_0\varepsilon_2\kappa & 0 & \tau \\ 0 & -\varepsilon_2\varepsilon_3\tau & 0 \end{bmatrix} \begin{bmatrix} \boldsymbol{t} \\ \boldsymbol{n} \\ \boldsymbol{b} \end{bmatrix} \tag{7}$$

where $\langle \boldsymbol{t}, \boldsymbol{t} \rangle = \varepsilon_0, \langle \boldsymbol{n}, \boldsymbol{n} \rangle = \varepsilon_2$ and $\langle \boldsymbol{b}, \boldsymbol{b} \rangle = \varepsilon_3 = \varepsilon_0\varepsilon_2$.

Curve $\alpha(s)$'s Minkowski curvature and torsion are found by, respectively,

$$\kappa = \|\boldsymbol{t}'\|, \qquad \tau = \langle \boldsymbol{n}', \boldsymbol{b} \rangle \tag{8}$$

(Akutagawa & Nishikawa, 1990, Oneill, 1983).

In this paper, firstly, we define a new adapted frame (q-frame) by using the quasi-normal vector along a space curve. Then we obtain the differential geometry properties of the Bertrand curves by using the q-frame. Compared to other frames, the q-frame has a number of advantages (Frenet, Bishop). For example, the q-frame can even be defined along the line ($\kappa = 0$) and whether or not the space curve has unit speed has no effect on how the q-frame is built. The q-frame can also be computed with ease.

2. q-frame Along a Space Curve

Here, instead of the Frenet frame, we define a new altered frame, the q-frame, along a space curve in Minkowski space. The q-frame, given a regular space curve $\alpha(s)$, is made up of three orthonormal vectors: the unit tangent vector $\boldsymbol{t}$, the quasi-normal $\mathbf{n}_q$ and the quasi-binormal $\mathbf{b}_q$. The q-frame $\{ \boldsymbol{t}, \mathbf{n}_q, \boldsymbol{b}_q, \boldsymbol{k} \}$ along $\alpha(s)$ is defined as

$$\boldsymbol{t} = \frac{\alpha'}{||\alpha'||}, \mathbf{n}_q = \frac{\boldsymbol{t} \wedge \boldsymbol{k}}{||\boldsymbol{t} \wedge \boldsymbol{k}||}, \quad \mathbf{b}_q = \boldsymbol{t} \wedge \mathbf{n}_q. \tag{9}$$

Figure 1 depicts a q-frame along a space curve.

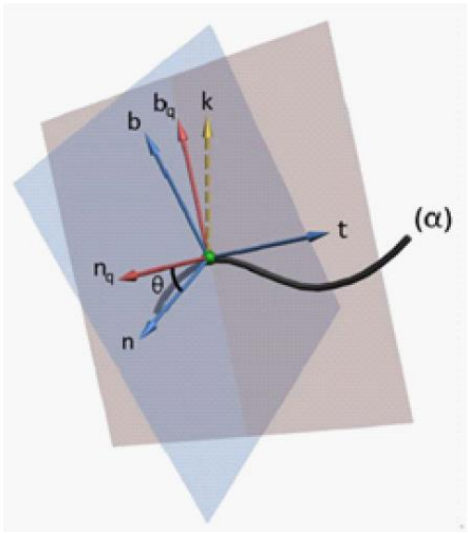

Figure 1. the quasi frame and Frenet frame

The projection vector $\boldsymbol{k}$ should be chosen so that $\boldsymbol{t}$ and $\boldsymbol{k}$ are not parallel.

Theorem 2.1. Let $\alpha(s)$ be a non-null curve with arc length s as a parameter. The directional q-frame's variation equations are provided by

$$\begin{bmatrix} \boldsymbol{t}' \\ \boldsymbol{n}_q' \\ \boldsymbol{b}_q' \end{bmatrix} = \begin{bmatrix} 0 & \varepsilon_1 k_1 & -\varepsilon_0\varepsilon_1 k_2 \\ -\varepsilon_0 k_1 & 0 & -\varepsilon_0\varepsilon_1 k_3 \\ -\varepsilon_0 k_2 & -\varepsilon_1 k_3 & 0 \end{bmatrix} \begin{bmatrix} \boldsymbol{t} \\ \boldsymbol{n}_q \\ \boldsymbol{b}_q \end{bmatrix} \tag{10}$$

where $\langle \boldsymbol{t}, \boldsymbol{t} \rangle = \varepsilon_0$, $\langle \boldsymbol{n}_q, \boldsymbol{n}_q \rangle = \varepsilon_1$, $\langle \boldsymbol{b}_q, \boldsymbol{b}_q \rangle = \varepsilon_4$, $\langle \boldsymbol{n}, \boldsymbol{n} \rangle = \varepsilon_2, \langle \boldsymbol{b}, \boldsymbol{b} \rangle = \varepsilon_3$ and the q-curvatures are written in the following format:

$$k_1 = \langle \boldsymbol{t}', \boldsymbol{n}_q \rangle, k_2 = \langle \boldsymbol{t}', \boldsymbol{b}_q \rangle, k_3 = \langle \boldsymbol{n}_q', \boldsymbol{b}_q \rangle \tag{11}$$

Proof. Since it is

$$\langle \boldsymbol{b}, \boldsymbol{b} \rangle = \langle \boldsymbol{t} \wedge \boldsymbol{n}, \boldsymbol{t} \wedge \boldsymbol{n} \rangle = -\langle \boldsymbol{t}, \boldsymbol{t} \rangle \langle \boldsymbol{n}, \boldsymbol{n} \rangle + \langle \boldsymbol{t}, \boldsymbol{n} \rangle^2 = -\varepsilon_0\varepsilon_2$$

according to the Lagrange's identity, $\varepsilon_3 = -\varepsilon_0\varepsilon_2$ is obtained.
Thus, The derivatives of Frenet vectors in terms of Frenet vectors may be written as (7). The derivatives of q-frame vectors in terms of q-frame vectors may be written as

$$\begin{aligned} \boldsymbol{t}' &= a_{11}\boldsymbol{t} + a_{12}\boldsymbol{n}_q + a_{13}\boldsymbol{b}_q \\ \boldsymbol{n}_q' &= a_{21}\boldsymbol{t} + a_{22}\boldsymbol{n}_q + a_{23}\boldsymbol{b}_q \\ \boldsymbol{b}_q' &= a_{31}\boldsymbol{t} + a_{32}\boldsymbol{n}_q + a_{33}\boldsymbol{b}_q. \end{aligned} \tag{12}$$

Using the equations (12) and Lorentz dot product

$$\begin{array}{lll} \langle \boldsymbol{t}', \boldsymbol{t}\rangle = \varepsilon_0 a_{11} & \langle \boldsymbol{t}', \boldsymbol{n}_q\rangle = \varepsilon_1 a_{12} & \langle \boldsymbol{t}', \boldsymbol{b}_q\rangle = \varepsilon_4 a_{13} \\ \langle \boldsymbol{n}_q', \boldsymbol{t}\rangle = \varepsilon_0 a_{21} & \langle \boldsymbol{n}_q', \boldsymbol{n}_q\rangle = \varepsilon_1 a_{22} & \langle \boldsymbol{n}_q', \boldsymbol{b}_q\rangle = \varepsilon_4 a_{23} \\ \langle \boldsymbol{b}_q', \boldsymbol{t}\rangle = \varepsilon_0 a_{31} & \langle \boldsymbol{b}_q', \boldsymbol{n}_q\rangle = \varepsilon_1 a_{32} & \langle \boldsymbol{b}_q', \boldsymbol{b}_q\rangle = \varepsilon_4 a_{33} \end{array} \tag{13}$$

is found.

Moreover, differentiating $\langle \boldsymbol{t}, \boldsymbol{n}_q\rangle = 0$ equation with respect to$s$ and using (13), we get

$$a_{12} = \varepsilon_1 k_1, a_{21} = -\varepsilon_0 k_1.$$

Similarly it becomes

$$a_{23} = \varepsilon_4 k_3, a_{32} = -\varepsilon_1 k_3$$

and

$$a_{13} = \varepsilon_4 k_2, a_{31} = -\varepsilon_0 k_2.$$

Since it is

$$\langle \boldsymbol{b}_q, \boldsymbol{b}_q\rangle = \langle \boldsymbol{t} \wedge \boldsymbol{n}_q, \boldsymbol{t} \wedge \boldsymbol{n}_q\rangle = -\langle \boldsymbol{t}, \boldsymbol{t}\rangle\langle \boldsymbol{n}_q, \boldsymbol{n}_q\rangle + \langle \boldsymbol{t}, \boldsymbol{n}_q\rangle^2 = -\varepsilon_0\varepsilon_1$$

according to the Lagrange's identity $\varepsilon_4 = -\varepsilon_0\varepsilon_1$ is obtained. Thus,

$$\begin{bmatrix} \boldsymbol{t}' \\ \boldsymbol{n}_q' \\ \boldsymbol{b}_q' \end{bmatrix} = \begin{bmatrix} 0 & \varepsilon_1 k_1 & -\varepsilon_0\varepsilon_1 k_2 \\ -\varepsilon_0 k_1 & 0 & -\varepsilon_0\varepsilon_1 k_3 \\ -\varepsilon_0 k_2 & -\varepsilon_1 k_3 & 0 \end{bmatrix} \begin{bmatrix} \boldsymbol{t} \\ \boldsymbol{n}_q \\ \boldsymbol{b}_q \end{bmatrix}$$

is obtained. ■

Theorem 2.2. In Minkowski space, where $\boldsymbol{t}$ is the unit tangent vector spacelike, $\boldsymbol{k}$ is the projection vector timelike (spacelike), $\boldsymbol{n}_q$ is the quasi-normal vector and $\boldsymbol{n}$ is the normal vector spacelike (timelike), $\boldsymbol{b}_q$ is the quasi-binormal vector and $\boldsymbol{b}$ is the binormal vector timelike (spacelike), the relationship between

the $\{\boldsymbol{t}, \mathbf{n}_q, \boldsymbol{b}_q\}$ q-frame and the $\{\boldsymbol{t}, \boldsymbol{n}, \boldsymbol{b}\}$ Frenet frame along the spacelike curve is

$$\begin{bmatrix} \boldsymbol{t} \\ \boldsymbol{n}_q \\ \boldsymbol{b}_q \end{bmatrix} = \begin{bmatrix} 1 & 0 & 0 \\ 0 & \varepsilon_1\varepsilon_2 cosh\theta & sinh\theta \\ 0 & sinh\theta & \varepsilon_1\varepsilon_2 cosh\theta \end{bmatrix} \begin{bmatrix} \boldsymbol{t} \\ \boldsymbol{n} \\ \boldsymbol{b} \end{bmatrix}$$

and

$$\begin{bmatrix} \boldsymbol{t} \\ \boldsymbol{n} \\ \boldsymbol{b} \end{bmatrix} = \begin{bmatrix} 1 & 0 & 0 \\ 0 & \varepsilon_1\varepsilon_2 cosh\theta & -sinh\theta \\ 0 & -sinh\theta & \varepsilon_1\varepsilon_2 cosh\theta \end{bmatrix} \begin{bmatrix} \boldsymbol{t} \\ \boldsymbol{n}_q \\ \boldsymbol{b}_q \end{bmatrix}.$$

Where θ is the angle between $\boldsymbol{n}_q$ and $\boldsymbol{n}$, and

$$\langle \boldsymbol{t}, \boldsymbol{t} \rangle = \varepsilon_0, \qquad \langle \boldsymbol{n}_q, \boldsymbol{n}_q \rangle = \varepsilon_1, \qquad \langle \boldsymbol{n}, \boldsymbol{n} \rangle = \varepsilon_2,$$
$$\langle \boldsymbol{b}, \boldsymbol{b} \rangle = -\varepsilon_0\varepsilon_2, \quad \langle \boldsymbol{b}_q, \boldsymbol{b}_q \rangle = -\varepsilon_0\varepsilon_1.$$

Proof. i) Since, $\boldsymbol{b}_q$ is in the plane spanned by the vectors $\boldsymbol{n}$ and $\boldsymbol{b}$,

$$\boldsymbol{b}_q = \lambda\boldsymbol{n} + \mu\boldsymbol{b} \tag{14}$$

written. Since $\boldsymbol{b}$ and $\boldsymbol{b}_q$ are in the same timecone, $\langle \boldsymbol{b}, \boldsymbol{b}_q \rangle = -cosh\theta$ is written. Using this, along with the equations $\langle \boldsymbol{b}, \boldsymbol{b} \rangle = -\varepsilon_0\varepsilon_2$ and $\langle \boldsymbol{b}, \boldsymbol{n} \rangle = 0$ then

$$\mu = \varepsilon_0\varepsilon_2\, cosh\theta$$

is found. Similarly, by using $\langle \boldsymbol{b}_q, \boldsymbol{b}_q \rangle = -\varepsilon_0\varepsilon_1, \langle \boldsymbol{n}, \boldsymbol{n} \rangle = \varepsilon_2,\ \langle \boldsymbol{n}, \boldsymbol{b} \rangle = 0$ and $\langle \boldsymbol{b}, \boldsymbol{b} \rangle = -\varepsilon_0\varepsilon_2$,

$$\lambda = sinh\theta$$

is obtained.

Accordingly, it is found as

$$\boldsymbol{b}_q = sinh\theta\boldsymbol{n} + \varepsilon_0\varepsilon_2 cosh\theta\boldsymbol{b}$$

Using (9) and $\boldsymbol{t} \wedge \boldsymbol{b}_q = \boldsymbol{n}_q$, we obtained as

$$\boldsymbol{n}_q = \varepsilon_0\varepsilon_2 cosh\theta\boldsymbol{n} + sinh\theta\boldsymbol{b}$$

ii) Since, $\boldsymbol{n}_q$ is in the plane spanned by the vectors $\boldsymbol{n}$ and $\boldsymbol{b}$,

$$\boldsymbol{n}_q = \lambda\boldsymbol{n} + \mu\boldsymbol{b} \tag{15}$$

written. Since $\boldsymbol{n}$ and $\boldsymbol{n}_q$ are in the same timecone,

$$\langle \boldsymbol{n}, \boldsymbol{n}_q \rangle = -cosh\theta$$

is written. Using this, along with the equations $\langle \boldsymbol{n}, \boldsymbol{n} \rangle = \varepsilon_2$ and $\langle \boldsymbol{b}, \boldsymbol{n} \rangle = 0$ then

$$\lambda = -\varepsilon_2 cosh\theta$$

is found. Similarly, by using $\langle \boldsymbol{n}_q, \boldsymbol{n}_q \rangle = \varepsilon_1, \langle \boldsymbol{n}, \boldsymbol{n} \rangle = \varepsilon_2,\ \langle \boldsymbol{n}, \boldsymbol{b} \rangle = 0$ and $\langle \boldsymbol{b}, \boldsymbol{b} \rangle = -\varepsilon_0\varepsilon_2$,

$$\mu = sinh\theta$$

is obtained.

Accordingly, it is found as

$$\boldsymbol{n}_q = -\varepsilon_2 cosh\theta\boldsymbol{n} + sinh\theta\boldsymbol{b}.$$

Using (9) and $\boldsymbol{n}_q \wedge \boldsymbol{t} = \boldsymbol{b}_q$, we obtained as

$$\boldsymbol{b}_q = sinh\theta\boldsymbol{n} - \varepsilon_2 cosh\theta\boldsymbol{b}.$$

Hence, if $\varepsilon_1\varepsilon_2 = \varepsilon_0\varepsilon_2$ is used for frame vectors, the relation between Frenet frame and q-frame is found as

$$\begin{bmatrix} \boldsymbol{t} \\ \boldsymbol{n}_q \\ \boldsymbol{b}_q \end{bmatrix} = \begin{bmatrix} 1 & 0 & 0 \\ 0 & \varepsilon_1\varepsilon_2 cosh\theta & sinh\theta \\ 0 & sinh\theta & \varepsilon_1\varepsilon_2 cosh\theta \end{bmatrix} \begin{bmatrix} \boldsymbol{t} \\ \boldsymbol{n} \\ \boldsymbol{b} \end{bmatrix}. \tag{16}$$

Using (16), we obtain

$$\boldsymbol{n} = \varepsilon_0\varepsilon_2 cosh\theta\boldsymbol{n}_q - sinh\theta\boldsymbol{b}_q$$

and

$$\boldsymbol{b} = -sinh\theta\boldsymbol{n}_q + \varepsilon_0\varepsilon_2 cosh\theta\boldsymbol{b}_q.$$

The calculations which have been done are written in the form of matrix and

$$\begin{bmatrix} \boldsymbol{t} \\ \boldsymbol{n} \\ \boldsymbol{b} \end{bmatrix} = \begin{bmatrix} 1 & 0 & 0 \\ 0 & \varepsilon_1\varepsilon_2 cosh\theta & -sinh\theta \\ 0 & -sinh\theta & \varepsilon_1\varepsilon_2 cosh\theta \end{bmatrix} \begin{bmatrix} \boldsymbol{t} \\ \boldsymbol{n}_q \\ \boldsymbol{b}_q \end{bmatrix} \tag{17}$$

is obtained. ■

Theorem 2.3. In Minkowski space, where $\boldsymbol{t}$ is the unit tangent vector spacelike, $\boldsymbol{k}$ is the projection vector timelike(spacelike), $\boldsymbol{n}_q$ is the quasi-normal vector and $\boldsymbol{n}$ is the normal vector spacelike(timelike), $\boldsymbol{b}_q$ is the quasi-binormal vector and $\boldsymbol{b}$ is the binormal vector timelike(spacelike), the relationship betweenthe curvatures of both the $\{\boldsymbol{t}, \mathbf{n}_q, \boldsymbol{b}_q\}$ q-frame and the $\{\boldsymbol{t}, \boldsymbol{n}, \boldsymbol{b}\}$ Frenet frame along the spacelike curve is

$$k_1 = \varepsilon_2\kappa cosh\theta, k_2 = \varepsilon_0\varepsilon_2\kappa sinh\theta, k_3 = -\varepsilon_0(\varepsilon_2 d\theta + \varepsilon_1\tau).$$

Where

$$\begin{aligned} &\langle \boldsymbol{t}, \boldsymbol{t} \rangle = \varepsilon_0, && \langle \boldsymbol{n}_q, \boldsymbol{n}_q \rangle = \varepsilon_1, && \langle \boldsymbol{n}, \boldsymbol{n} \rangle = \varepsilon_2, \\ &\langle \boldsymbol{b}, \boldsymbol{b} \rangle = -\varepsilon_0\varepsilon_2, && \langle \boldsymbol{b}_q, \boldsymbol{b}_q \rangle = -\varepsilon_0\varepsilon_1. \end{aligned}$$

Proof. Using (7) and (17),

$$\boldsymbol{t}' = \kappa\, cosh\theta \boldsymbol{n}_q - \kappa\varepsilon_1\varepsilon_2 sinh\theta \boldsymbol{b}_q$$

is obtained. From (11), k_1 is obtained as

$$k_1 = \kappa\varepsilon_2 cosh\theta.$$

On the other hand, by using (16) gives

$$\boldsymbol{n}_q = \varepsilon_1\varepsilon_2 cosh\theta \boldsymbol{n} + sinh\theta \boldsymbol{b}. \tag{18}$$

By substituting (7) and (17) in this equation and differentiating (18) with regard to s,

$$\begin{aligned}\boldsymbol{n}_q' = \quad & \boldsymbol{n}_q(sinh\theta cosh\theta d\theta + \varepsilon_0\varepsilon_1\varepsilon_2\tau sinh\theta cosh\theta \\ & -\varepsilon_1\varepsilon_2\tau sinh\theta cosh\theta - sinh\theta cosh\theta d\theta) \\ & +\boldsymbol{t}(-\varepsilon_0\varepsilon_1\kappa cosh\theta) + \boldsymbol{b}_q(-\varepsilon_1\varepsilon_2 sinh^2\theta d\theta \\ & -\varepsilon_0\tau sinh^2\theta d\theta + \tau sinh^2\theta + \varepsilon_1\varepsilon_2 cosh^2\theta d\theta)\end{aligned}$$

is found.

Using (11) and $\langle \boldsymbol{b}_q, \boldsymbol{b}_q \rangle = -\varepsilon_0\varepsilon_1$,$k_2$ and k_3 are found as follows

$$k_2 = \varepsilon_0\varepsilon_1\kappa sinh\theta, k_3 = -\varepsilon_0(\varepsilon_2 d\theta + \varepsilon_1\tau).$$

Consequently, the proof is complete.■

Theorem 2.4. In Minkowski space, where $\boldsymbol{t}$ is the unit tangent vector spacelike, $\boldsymbol{k}$ is the projection vector timelike (spacelike), $\boldsymbol{n}_q$ is the quasi-normal vector and $\boldsymbol{b}$ is the binormal vector spacelike (timelike), $\boldsymbol{b}_q$ is the quasi-binormal vector and $\boldsymbol{n}$ is the normal vector timelike (spacelike), the relationship between the $\{\boldsymbol{t}, \mathbf{n}_q, \boldsymbol{b}_q\}$ q-frame and the $\{\boldsymbol{t}, \boldsymbol{n}, \boldsymbol{b}\}$ Frenet frame along the spacelike curve is

$$\begin{bmatrix} \boldsymbol{t} \\ \boldsymbol{n}_q \\ \boldsymbol{b}_q \end{bmatrix} = \begin{bmatrix} 1 & 0 & 0 \\ 0 & -\varepsilon_1 sinh\theta & \varepsilon_2 cosh\theta \\ 0 & -\varepsilon_2 cosh\theta & \varepsilon_1 sinh\theta \end{bmatrix} \begin{bmatrix} \boldsymbol{t} \\ \boldsymbol{n} \\ \boldsymbol{b} \end{bmatrix}$$

and

$$\begin{bmatrix} \boldsymbol{t} \\ \boldsymbol{n} \\ \boldsymbol{b} \end{bmatrix} = \begin{bmatrix} 1 & 0 & 0 \\ 0 & \varepsilon_1 sinh\theta & -\varepsilon_2 cosh\theta \\ 0 & \varepsilon_2 cosh\theta & -\varepsilon_1 sinh\theta \end{bmatrix} \begin{bmatrix} \boldsymbol{t} \\ \boldsymbol{n}_q \\ \boldsymbol{b}_q \end{bmatrix}.$$

Where

$$\begin{aligned} &\langle \boldsymbol{t}, \boldsymbol{t} \rangle = \varepsilon_0, \quad && \langle \boldsymbol{n}_q, \boldsymbol{n}_q \rangle = \varepsilon_1, \quad && \langle \boldsymbol{n}, \boldsymbol{n} \rangle = \varepsilon_2, \\ &\langle \boldsymbol{b}, \boldsymbol{b} \rangle = -\varepsilon_0\varepsilon_2, \quad && \langle \boldsymbol{b}_q, \boldsymbol{b}_q \rangle = -\varepsilon_0\varepsilon_1. \end{aligned}$$

Proof. Here, the proof is easily obtained using similar steps as in the proof of Theorem 2.2.■

Theorem 2.5. In Minkowski space, where $\boldsymbol{t}$ is the unit tangent vector spacelike, $\boldsymbol{k}$ is the projection vector timelike (spacelike), $\boldsymbol{n}_q$ is the quasi-normal vector and $\boldsymbol{b}$ is the binormal vector spacelike (timelike), $\boldsymbol{b}_q$ is the quasi-binormal vector and $\boldsymbol{n}$ is the normal vector timelike (spacelike), the relationship

between the curvatures of both the $\{\boldsymbol{t}, \mathbf{n}_q, \boldsymbol{b}_q\}$ q-frame and the $\{\boldsymbol{t}, \boldsymbol{n}, \boldsymbol{b}\}$ Frenet frame along the spacelike curve is

$$k_1 = \kappa sinh\theta, k_2 = \varepsilon_0\varepsilon_1\varepsilon_2\kappa cosh\theta, k_3 = \varepsilon_0(-\varepsilon_2 d\theta + \varepsilon_1\tau).$$

Where

$$\langle \boldsymbol{t}, \boldsymbol{t}\rangle = \varepsilon_0, \quad \langle \boldsymbol{n}_q, \boldsymbol{n}_q\rangle = \varepsilon_1, \quad \langle \boldsymbol{n}, \boldsymbol{n}\rangle = \varepsilon_2,$$
$$\langle \boldsymbol{b}, \boldsymbol{b}\rangle = -\varepsilon_0\varepsilon_2, \quad \langle \boldsymbol{b}_q, \boldsymbol{b}_q\rangle = -\varepsilon_0\varepsilon_1.$$

Proof. Applying the same steps to Theorem 2.3 completes the proof.■

Theorem 2.6. In Minkowski space, where $\boldsymbol{t}$ is the unit tangent vector timelike, $\boldsymbol{k}$ is the projection vector spacelike, $\boldsymbol{n}_q$ is the quasi-normal vector and $\boldsymbol{n}$ is the normal vector spacelike, $\boldsymbol{b}_q$ is the quasi-binormal vector and $\boldsymbol{b}$ is the binormal vector spacelike, the relationship between the $\{\boldsymbol{t}, \mathbf{n}_q, \boldsymbol{b}_q\}$ q-frame and the $\{\boldsymbol{t}, \boldsymbol{n}, \boldsymbol{b}\}$ Frenet frame along the timelike curve is

$$\begin{bmatrix} \boldsymbol{t} \\ \boldsymbol{n}_q \\ \boldsymbol{b}_q \end{bmatrix} = \begin{bmatrix} 1 & 0 & 0 \\ 0 & cos\theta & sin\theta \\ 0 & -sin\theta & cos\theta \end{bmatrix} \begin{bmatrix} \boldsymbol{t} \\ \boldsymbol{n} \\ \boldsymbol{b} \end{bmatrix}$$

and

$$\begin{bmatrix} \boldsymbol{t} \\ \boldsymbol{n} \\ \boldsymbol{b} \end{bmatrix} = \begin{bmatrix} 1 & 0 & 0 \\ 0 & cos\theta & -sin\theta \\ 0 & sin\theta & cos\theta \end{bmatrix} \begin{bmatrix} \boldsymbol{t} \\ \boldsymbol{n}_q \\ \boldsymbol{b}_q \end{bmatrix}.$$

Where

$$\langle \boldsymbol{t}, \boldsymbol{t}\rangle = \varepsilon_0, \quad \langle \boldsymbol{n}_q, \boldsymbol{n}_q\rangle = \varepsilon_1, \quad \langle \boldsymbol{n}, \boldsymbol{n}\rangle = \varepsilon_2,$$
$$\langle \boldsymbol{b}, \boldsymbol{b}\rangle = -\varepsilon_0\varepsilon_2, \quad \langle \boldsymbol{b}_q, \boldsymbol{b}_q\rangle = -\varepsilon_0\varepsilon_1.$$

Proof. Applying the same steps to Theorem 2.2 completes the proof.■

Theorem 2.7. In Minkowski space, where $\boldsymbol{t}$ is the unit tangent vector timelike, $\boldsymbol{k}$ is the projection vector spacelike, $\boldsymbol{n}_q$ is the quasi-normal vector and $\boldsymbol{n}$ is the normal vector spacelike, $\boldsymbol{b}_q$ is the quasi-binormal vector and $\boldsymbol{b}$ is the binormal vector spacelike, the relationship between the curvatures of both the $\{\boldsymbol{t}, \mathbf{n}_q, \boldsymbol{b}_q\}$ q-frame and the $\{\boldsymbol{t}, \boldsymbol{n}, \boldsymbol{b}\}$ Frenet frame along the timelike curve is

$$k_1 = \kappa cos\theta, k_2 = -\kappa sin\theta, k_3 = d\theta + \tau.$$

Where

$$\langle \boldsymbol{t}, \boldsymbol{t} \rangle = \varepsilon_0, \quad \langle \boldsymbol{n}_q, \boldsymbol{n}_q \rangle = \varepsilon_1, \quad \langle \boldsymbol{n}, \boldsymbol{n} \rangle = \varepsilon_2,$$
$$\langle \boldsymbol{b}, \boldsymbol{b} \rangle = -\varepsilon_0\varepsilon_2, \quad \langle \boldsymbol{b}_q, \boldsymbol{b}_q \rangle = -\varepsilon_0\varepsilon_1.$$

Proof. Here, the proof is easily obtained using similar steps as in the proof of Theorem 2.3.■

3. Directional Bertrand Curves

By utilizing the curves, we introduce the directional Bertrand curves in this section. The tangent vector $\boldsymbol{t}$, the quasi-normal vector $\boldsymbol{n}_q$, the quasi-binormal vector $\boldsymbol{b}_q$, and the projection vector $\boldsymbol{k}$ are present in this case. If there is a one-to-one correspondence between the points of a pair of curves such that the curves are referred to as directional Bertrand mates when they have a similar principal quasi-normal at their respective locations.

Proposition 3.1. Let $\alpha(s)$ be a space curve in Minkowski space with arc length parameter s. The following is true if a curve $\beta(s)$ parameterized by arc length function s_1 is directional Bertrand mate of $\alpha(s)$:

(a) there is a constant distance between the directional Bertrand mates' corresponding points.

(b) if $k_3 = 0$, the tangent vectors at the corresponding points of the directional Bertrand mates have a constant angle between them.

Proof. (a) Let's use the notation $\{ \boldsymbol{t}, \mathbf{n}_q, \boldsymbol{b}_q \}$ and $\{ \boldsymbol{t}^\lambda, \boldsymbol{n}_q^\lambda, \boldsymbol{b}_q^\lambda \}$ respectively, to represent the q-frames of α and β. The position vectors of α and β have a relationship as

$$\beta(s) = \alpha(s) + \lambda \mathbf{n}_q, \tag{19}$$

then. By differentiating (19) respect to $s$gives

$$\boldsymbol{t}^\lambda \frac{ds_1}{ds} = (1 - \lambda\varepsilon_0 k_1)\boldsymbol{t} + \lambda' \mathbf{n}_q - \lambda\varepsilon_0\varepsilon_1 k_3 \mathbf{b}_q \tag{20}$$

Thus $\boldsymbol{t}^\lambda$ is ortogonal to $\mathbf{n}_q$, since it is clear that

$$\lambda' = 0, \tag{21}$$

which means that $\lambda = constant$, the distance between α and β 's corresponding points

$$\|\beta(s) - \alpha(s)\| = \lambda \tag{22}$$

is constant. That concludes the proof.

(b) From (20) and (21), we get

$$\frac{ds_1}{ds} = \pm\sqrt{|\varepsilon_0(1-\lambda\varepsilon_0 k_1)^2 - \lambda^2\varepsilon_0\varepsilon_1 k_3^2|} \tag{23}$$

Thus, (20) reduces to

$$\boldsymbol{t}^{\lambda} = \pm\frac{(1-\lambda\varepsilon_0 k_1)\boldsymbol{t} - \lambda\varepsilon_0\varepsilon_1 k_3 \mathbf{b}_q}{\sqrt{|\varepsilon_0(1-\lambda\varepsilon_0 k_1)^2 - \lambda^2\varepsilon_0\varepsilon_1 k_3^2|}} \tag{24}$$

i) Let φ stand for the angle formed by the tangent vectors that are spacelike, $\boldsymbol{t}$ and $\boldsymbol{t}^{\lambda}$.

As a result, we can write

$$\langle \boldsymbol{t}^{\lambda}, \boldsymbol{t}\rangle = -cos\varphi$$

Where

$$cos\varphi = \pm\frac{\varepsilon_0 - \lambda k_1}{\sqrt{|\varepsilon_0(1-\lambda\varepsilon_0 k_1)^2 - \lambda^2\varepsilon_0\varepsilon_1 k_3^2|}}. \tag{25}$$

ii) The hyperbolic angle between the timelike tangent vectors $\boldsymbol{t}$ and $\boldsymbol{t}^{\lambda}$ is denoted by φ. As a result, we can write

$$\langle \boldsymbol{t}^{\lambda}, \boldsymbol{t}\rangle = -cos\varphi$$

where

$$cos\varphi = \pm\frac{\varepsilon_0 - \lambda k_1}{\sqrt{|\varepsilon_0(1-\lambda\varepsilon_0 k_1)^2 - \lambda^2\varepsilon_0\varepsilon_1 k_3^2|}}. \tag{26}$$

In view of equations (25) and (26). Since $cos\varphi = +1$ and $cos\varphi = -1$ if $k_3 = 0$, it follows that the angle φ between the tangent vectors is constant. ■

Theorem 3.1. Let $\alpha(s)$ be a space curve with arc length parameter s in Minkowski space. The relationship between the q-frames of α and β can be expressed as

$$\begin{bmatrix} \boldsymbol{t}^{\lambda} \\ \boldsymbol{n}_q^{\lambda} \\ \boldsymbol{b}_q^{\lambda} \end{bmatrix} = \pm\frac{1}{\sqrt{\Delta}}\begin{bmatrix} 1-\lambda\varepsilon_0 k_1 & 0 & -\lambda\varepsilon_0\varepsilon_1 k_3 \\ 0 & \sqrt{\Delta} & 0 \\ \pm\lambda\varepsilon_0 k_3 & 0 & \pm(1-\lambda\varepsilon_0 k_1) \end{bmatrix}\begin{bmatrix} \boldsymbol{t} \\ \boldsymbol{n}_q \\ \boldsymbol{b}_q \end{bmatrix} \tag{27}$$

if the curve $\beta(s)$ is directional Bertrand mate of $\alpha(s)$, where $\Delta = \left|\varepsilon_0(1-\lambda\varepsilon_0 k_1)^2 - \lambda^2\varepsilon_0\varepsilon_1 k_3^2\right|$.

Proof. We get

$$\boldsymbol{t}^{\lambda} \wedge \boldsymbol{k} = \pm\frac{(1-\lambda\varepsilon_0 k_1)(\boldsymbol{t}\wedge\boldsymbol{k}) - \lambda\varepsilon_0\varepsilon_1 k_3(\mathbf{b}_q \wedge \boldsymbol{k})}{\sqrt{|\varepsilon_0(1-\lambda\varepsilon_0 k_1)^2 - \lambda^2\varepsilon_0\varepsilon_1 k_3^2|}} \tag{28}$$

by using (9), and (24). However, the use of Lagrange's identity and $\langle \boldsymbol{k}, \boldsymbol{k}\rangle = \varepsilon_5$ implies that

$$\|\boldsymbol{t}\wedge\boldsymbol{k}\| = \sqrt{|-\varepsilon_0\varepsilon_5 + \langle \boldsymbol{t}, \boldsymbol{k}\rangle^2|} = \sqrt{|-\varepsilon_0\varepsilon_5 + \mu^2|} \tag{29}$$

where μ is the second component of the $\alpha(s)$ curve's tangent vector.

Likewise, a easy calculation implies that

$$\begin{aligned} \boldsymbol{b}_q \wedge \boldsymbol{k} = \left(\boldsymbol{t}\wedge\boldsymbol{n}_q\right)\wedge\boldsymbol{k} &= -\langle \boldsymbol{t}, \boldsymbol{k}\rangle\boldsymbol{n}_q + \langle \boldsymbol{n}_q, \boldsymbol{k}\rangle\boldsymbol{t} \\ &= -\varepsilon_0\varepsilon_1\varepsilon_5\mu\boldsymbol{n}_q. \end{aligned} \tag{30}$$

Substituting (29) and (30) into (28) gives

$$\boldsymbol{t}^{\lambda} \wedge \boldsymbol{k} = \pm\frac{((1-\lambda\varepsilon_0 k_1)\sqrt{|-\varepsilon_0\varepsilon_5 + \mu^2|} + \lambda\mu\varepsilon_5 k_3)\mathbf{n}_q}{\sqrt{|\varepsilon_0(1-\lambda\varepsilon_0 k_1)^2 - \lambda^2\varepsilon_0\varepsilon_1 k_3^2|}}. \tag{31}$$

Thus, we have the quasi-normal vector $\boldsymbol{n}_q^\lambda$ of β in the following form

$$\boldsymbol{n}_q^\lambda = \frac{\boldsymbol{t}^\lambda \wedge \boldsymbol{k}}{\|\boldsymbol{t}^\lambda \wedge \boldsymbol{k}\|} = \pm \boldsymbol{n}_q. \tag{32}$$

Be aware that the aforementioned equation implies that the timelike directional Bertrand mates' quasi-normal vectors $\boldsymbol{n}_q$ and $\boldsymbol{n}_q^\lambda$ are always linearly dependent. By using (9), and (24), one may get

$$\boldsymbol{b}_q^\lambda = \pm \frac{-\lambda\varepsilon_0 k_3 \boldsymbol{t} + (1-\lambda\varepsilon_0 k_1)\mathbf{b}_q}{\sqrt{|\varepsilon_0(1-\lambda\varepsilon_0 k_1)^2 - \lambda^2\varepsilon_0\varepsilon_1 k_3^2|}} \tag{33}$$

the quasi-binormal of $\beta(s)$. Consequently, we state the main corollary that follows.■

Theorem 3.2. Let s be the arc length parameter for the space curve $\alpha(s)$. It is expessed the relationships between the q -curvatures of the Bertrand mates $\alpha(s)$ and $\beta(s)$ as

$$k_1^\lambda = \frac{\lambda\varepsilon_0\varepsilon_1 k_3^2 \boldsymbol{t} + (1-\lambda\varepsilon_0 k_1)k_1}{\sqrt{|\varepsilon_0(1-\lambda\varepsilon_0 k_1)^2 - \lambda^2\varepsilon_0\varepsilon_1 k_3^2|}}, \tag{34}$$

$$k_2^\lambda = \pm \frac{\lambda k_3'(1-\lambda\varepsilon_0 k_1) + \lambda^2\varepsilon_0 k_1' k_3 + ((1-\lambda\varepsilon_0 k_1)^2 - \lambda^2\varepsilon_1 k_3^2)k_2}{|\varepsilon_0(1-\lambda\varepsilon_0 k_1)^2 - \lambda^2\varepsilon_0\varepsilon_1 k_3^2|} \tag{35}$$

and

$$k_3^\lambda = \pm \frac{k_3}{\sqrt{|\varepsilon_0(1-\lambda\varepsilon_0 k_1)^2 - \lambda^2\varepsilon_0\varepsilon_1 k_3^2|}}, \tag{36}$$

if a curve $\alpha(s)$ has a directional Bertrand mate $\beta(s)$, where k_1^λ, k_2^λ and k_3^λ are the q-curvatures of the curve $\beta(s)$.

$$\langle \boldsymbol{t}, \boldsymbol{t} \rangle = \varepsilon_0, \quad \langle \boldsymbol{n}_q, \boldsymbol{n}_q \rangle = \varepsilon_1, \quad \langle \boldsymbol{n}, \boldsymbol{n} \rangle = \varepsilon_2,$$
$$\langle \boldsymbol{b}, \boldsymbol{b} \rangle = -\varepsilon_0\varepsilon_2, \quad \langle \boldsymbol{b}_q, \boldsymbol{b}_q \rangle = -\varepsilon_0\varepsilon_1.$$

Proof. By differentiating (24) and substituting (10) into the results gives

$$\begin{aligned}\boldsymbol{t}^{\lambda'} = \pm\frac{\mathbf{1}}{(\varepsilon_0(1-\lambda\varepsilon_0 k_1)^2-\lambda^2\varepsilon_0\varepsilon_1 k_3^2)^{3/2}}[&(\varepsilon_0\varepsilon_1 k_1+\lambda k_3^2\\ &-3\lambda\varepsilon_1 k_1^2+2\lambda^3 k_1^2 k_3^2+3\lambda^2\varepsilon_0\varepsilon_1 k_1^2-3\lambda^2\varepsilon_0\varepsilon_1 k_3^2\\ &-\lambda^3\varepsilon_1 k_1^4-\lambda^3\varepsilon_1 k_3^4)\mathbf{n}_q+(\lambda\varepsilon_0\varepsilon_1 k_2 k_3+\lambda^3\varepsilon_1 k_1' k_3^2\\ &-2\lambda^2\varepsilon_1 k_1 k_2 k_3+\lambda^3\varepsilon_0\varepsilon_1 k_1^2 k_2 k_3-\lambda^3\varepsilon_0 k_2 k_3^3\\ &+\lambda^2\varepsilon_0\varepsilon_1 k_3 k_3'-\lambda^3\varepsilon_1 k_1 k_3 k_3')\boldsymbol{t}+(\lambda^2 k_2 k_3^2\\ &+2\lambda^2\varepsilon_0\varepsilon_1 k_1 k_3'+\lambda^3\varepsilon_0\varepsilon_1 k_1^3 k_2-\lambda^3\varepsilon_1 k_1^2 k_3'\\ &-\lambda^3\varepsilon_0 k_1 k_2 k_3^2+3\lambda\varepsilon_0\varepsilon_1 k_1 k_2-3\lambda^2\varepsilon_1 k_1^2 k_2\\ &-\lambda\varepsilon_1 k_3'-\varepsilon_1 k_2-\lambda^2\varepsilon_0\varepsilon_1 k_1' k_3+\lambda^3\varepsilon_1 k_1 k_1' k_3)\mathbf{b}_q]\end{aligned} \tag{37}$$

From (11) and (37), we have

$$k_1^\lambda=\frac{\lambda\varepsilon_0\varepsilon_1 k_3^2+(1-\lambda\varepsilon_0 k_1)k_1}{\sqrt{|\varepsilon_0(1-\lambda\varepsilon_0 k_1)^2-\lambda^2\varepsilon_0\varepsilon_1 k_3^2|}}. \tag{38}$$

By the similar method, the q-curvatures $k_2^\lambda=\langle \boldsymbol{t}^{\lambda'}, \boldsymbol{b}_q^\lambda\rangle$ can be obtained by

$$k_2^\lambda=\pm\frac{\lambda k_3'(1-\lambda\varepsilon_0 k_1)+\lambda^2\varepsilon_0 k_1' k_3+((1-\lambda\varepsilon_0 k_1)^2-\lambda^2\varepsilon_1 k_3^2)k_2}{|\varepsilon_0(1-\lambda\varepsilon_0 k_1)^2-\lambda^2\varepsilon_0\varepsilon_1 k_3^2|}. \tag{39}$$

Substituting (10) and (33) into (11) gives

$$k_3^\lambda=\pm\frac{k_3}{\sqrt{|\varepsilon_0(1-\lambda\varepsilon_0 k_1)^2-\lambda^2\varepsilon_0\varepsilon_1 k_3^2|}}, \tag{40}$$

That concludes the proof.■

4. Examples

In this part, some comparative examples are presented to demonstrate the effectiveness and stability of the timelike directional Bertrand mate.

Example 4.1. In this instance, we obtained the timelike directional Bertrand mate of a parametrized space curve with

$$\alpha(s) = (s, \sqrt{2}coshs, \sqrt{2}sinhs).$$

The line's q-frame is found as

$$\boldsymbol{t} = (1, \sqrt{2}sinhs, \sqrt{2}coshs)$$
$$\mathbf{n}_q = (-\frac{\sqrt{2}sinhs}{\sqrt{cosh2s}}, \frac{1}{\sqrt{cosh2s}}, 0)$$

and

$$\mathbf{b}_q = \left(-\frac{\sqrt{2}coshs}{\sqrt{cosh2s}}, \frac{-sinh2s}{\sqrt{cosh2s}}, -\sqrt{cosh2s}\right)$$

by using (1.1) and $\boldsymbol{k} = (0,0,1)$. It follows that the q-curvatures are calculated by

$$\mathrm{k}_1 = \frac{\sqrt{2}coshs}{\sqrt{cosh2s}} \tag{41}$$

and

$$\begin{aligned} \mathrm{k}_2 &= \frac{-\sqrt{2}coshs.sinh2s + \sqrt{2}sinhs.cosh2s}{\sqrt{cosh2s}} \\ \mathrm{k}_3 &= \frac{2cosh^2 s}{cosh2s}. \end{aligned} \tag{42}$$

The curve's timelike directional Bertrand mate is parametrized as

$$\beta(s) = \left(s - \frac{\sqrt{2}sinhs}{\sqrt{cosh2s}}, \sqrt{2}coshs + \frac{1}{\sqrt{cosh2s}}, \sqrt{2}sinhs\right)$$

for $\lambda = 1$. Using (41), (42) and Theorem 3.2, q-curvatures of the timelike directional Bertrand mate of the curve are

$$k_1^{\lambda} = \frac{\sqrt{2}\left(1+\frac{\sqrt{2}coshs}{\sqrt{cosh2s}}\right)cosh^{3/2}2s.coshs - 4cosh^4 s}{cosh2s\sqrt{\left|\frac{4cosh^4 s}{cosh^2 2s} - \left(1+\frac{\sqrt{2}coshs}{\sqrt{cosh2s}}\right)^2\right|}},$$

$$k_2^{\lambda} = \pm\frac{\sqrt{2}sinhs\left(\frac{4\sqrt{2}cosh^3 s}{cosh^2 2s} - \frac{1}{\sqrt{cosh2s}}\right)}{\sqrt{\left|\frac{4cosh^4 s}{cosh^2 2s} - \left(1+\frac{\sqrt{2}coshs}{\sqrt{cosh2s}}\right)^2\right|}} \pm \frac{\sqrt{2}sinhs}{\sqrt{cosh2s}},$$

$$k_3^{\lambda} = \pm\frac{2cosh^2 s}{cosh2s\sqrt{\left|\frac{4cosh^4 s}{cosh^2 2s} - \left(1+\frac{\sqrt{2}coshs}{\sqrt{cosh2s}}\right)^2\right|}}.$$

The $\alpha(s)$ timelike curve and its directional timelike Bertrand mate $\beta(s)$ are plotted in Figure 2.

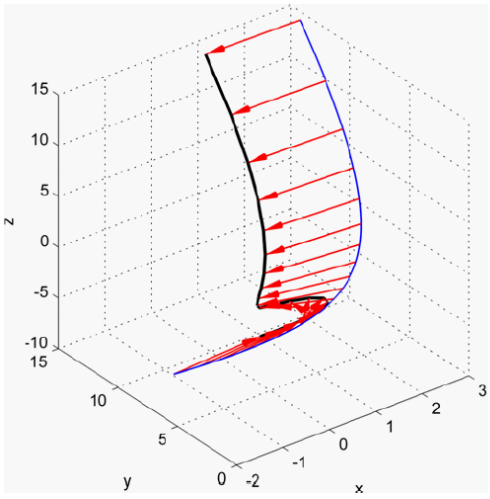

Figure 2: Timelike directional Bertrand mate (black) and timelike curve (blue). The red vectors are the quasi-normal vectors.

Example 4.2. The directional Bertrand mate of a line parametrized by

$$\alpha(s) = (1 + s, s, 3s)$$

was obtained in this instance.

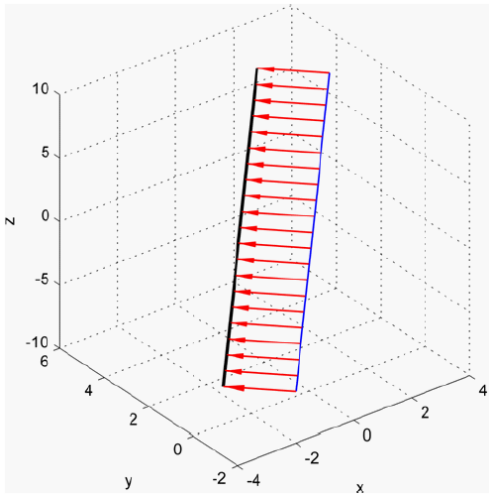

Figure 3: The directional Bertrand mate (black) and timelike curve (blue). The red vectors are the quasi-normal vectors.

The line's q-frame is found as

$$\boldsymbol{t} = \left(\frac{1}{\sqrt{7}}, \frac{1}{\sqrt{7}}, \frac{3}{\sqrt{7}}\right)$$
$$\mathbf{n}_q = \left(-\frac{1}{\sqrt{2}}, \frac{1}{\sqrt{2}}, 0\right)$$

and

$$\mathbf{b}_q = \left(-\frac{3}{\sqrt{14}}, -\frac{3}{\sqrt{14}}, -\frac{2}{\sqrt{14}}\right)$$

by using (9) and $\boldsymbol{k} = (0,0,1)$. It follows that the q-curvatures of the line are calculated by

$$\mathrm{k}_1 = \mathrm{k}_2 = \mathrm{k}_3 = 0. \qquad (43)$$

The line's directional Bertrand mate is parametrized as

$$\beta(s) = (s - \frac{1}{\sqrt{2}}, s + \frac{1}{\sqrt{2}}, 3s)$$

for $\lambda = 1$. Using (43) and Theorem 3.2, the curve's directional Bertrand mate's q-curvatures are

$$k_1^\lambda = k_2^\lambda = k_3^\lambda = 0.$$

5. Conclusions

In this study, firstly, using the non-null space curve and projection vector in Minkowski space, q-frame in equation (9) and the derivative equations of q-frame vectors in equation (10) are given in detail. Then, for the non-null curves the relations between q-frame and Frenet frame and their curvatures are found. Afterward, certain characteristic properties related to the directional Bertrand mate of a non-null space curve are obtained. In equation (34) are given the relations between the curve and its directional Bertrand mate q-frames and in Theorem 3.2 are also given the relations between their curvatures. Similar relations could be studied in future works in in higher-dimensional spaces.

6. Acknowledgements

The Research Projects Funding Unit of Eskisehir Osmangazi University in Eskisehir, Turkey, provided funding for this study (Project no. ESOGU-BAP: 2016-1189).

7. References

Akutagawa, K. & Nishikawa, S. (1990). The Gauss map and spacelike surfaces with prescribed mean curvature in Minkowski 3-space, Tohoku Mathematical Journal, 42, 67-82.

Balgetir, H., Bektaş, M. & Inoguchi, J. (2004). Null Bertrand curves in Minkowski 3-space and their characterizations, Note di Matematica, 23(1), 7-13.

Balgetir, H., Bektaş, M. & Ergüt, M. (2004a). Bertrand curves for nonnull curves in 3- dimensional Lorentzian space, Hadronic Journal, 27, 229-236.

Bertrand, J. M. (1850). Memoire sur la theorie des courbes a double courbure, Journal de Mathematiques Pures Et Appliquees, 15, 332-350.

Bishop, R. L. (1975). There is more than one way to frame a curve, Amer. Math. Monthly 82, 246-251.

Bloomenthal, J. (1990). Calculation of reference frames along a space curve, In Graphics Gems, 567-571.

Bonnor, W. B. (1969). Null curves in a Minkowski space-time, Tensor, 20, 229-242.

Choi, J. H., Kang, T. H. & Kim, Y. H. (2012). Bertrand curves in 3-dimensional space forms, Applied Mathematics and Computation 219, 1040-1046.

Coquillart, S. (1987). Computing offsets of B-spline curves, Computer-Aided Design, 19(6), 305-309.

Çöken, A. C., Çiftçi, Ü. & Ekici, C. (2008). On Parallel Timelike Ruled Surfaces with Timelike Rulings, KJSE- Kuwait Journal of Science & Engineering, 3, 21-31.

Dede, M., Ekici, C. & Tozak, H. (2015). Directional Tubular Surfaces, International Journal of Algebra, 9, 527-535.

Dede, M., Ekici, C. & Görgülü, A. (2015a). Directional q-frame along a space curve, IJARCSSE, 5(12), 775-780.

Ekmekçi, N. & Ilarslan, K. (2001). On Bertrand curves and their characterization, Differential Geometry Dynamical System 3, 17-24.

Gök, İ., Nurkan, S. K. & İlarslan, K. (2014). On Pseudo Null Bertrand Curves in Minkowski Space-Time, Kyungpook Mathematical Journal, 54(4), 685-697.

Izumiya, S. & Takeuchi, N. (2002). Generic properties of helices and Bertrand curves, J. of Geometry, 74, 97-109.

İlarslan, K. & Kılıç, N. (2017). On spacelike Bertrand curves in Minkowski 3-space, Konuralp Journal of Mathematics, 5(1), 214-222.

Jin, D. H. (2008). Null Bertrand curves in a Lorentz manifold, Journal of the Korean Society of Mathematical Education Series B: The Pure and Applied Mathematics, 15(3), 209-215.

Kahraman, F., Gök, İ. & İlarslan, K. (2014). Generalized Null Bertrand Curves in Minkowski Space-Time, Annals of th Alexandru Ioan Cuza University-Mathematics (N.S.), 60(2), 489-502.

Kuhnel, W. (1999). Differential geometry: curves-surfaces-manifolds, Braunscheweig, Weisbaden.

Matsuda, H. & Yorozu, S. (2003). Notes on bertrand curves, Yokohama Mathematical Journal 50, 41-58.

O'Neill, B. (1983). Semi-Riemannian Geometry with Applications to Relativity, Academic Press.

Otsuki, T. (1961). Differential Geometry (Japanese), Asakura Shoten, Tokyo.

Öztekin, H. B. & Bektaş, M. (2010). Representation Formulae for Bertrand Curves in the Minkowski 3-space, Scientia Magna, 6, 89-96.

Papaioannou, S. G. & Kiritsis, D. (1985). An application of Bertrand curves and surface to CAD/CAM, Computer-Aided Design, 8(17), 348-352.

Ravani, B. & Ku, T. S. (1991). Bertrand Offsets of ruled and developable surfaces, Comp. Aided Geom. Design, 23(2), 145-152.

Saint Venant, B. (1845). Memoire sur les lignes courbes non planes, Journal de I' Ecole Polytecnique, 18, 1-76.

Tunçer, Y. & Ünal, S. (2012). New representations of Bertrand pairs in Euclidean 3-space, Applied Mathematics and Computation, 219, 1833-1842.

Wang, W., Jüttler, B., Zheng, D. & Liu, Y. (2008). Computation of rotation minimizing frame, ACM Trans. Graph, 27(1), 18 pages.

Whittemore, J. K. (1940). Bertrand curves and helices, Duke Mathematical Journal, 6, 235-245.

Chapter 3

New Enhanced Methods for System Reliability Bounds

Mehmet YILMAZ[1]

[1] Prof. Dr.; Ankara University, Faculty of Science, Department of Statistics, Ankara-TÜRKİYE.
e-mail: scimehmet@gmail.com (ORCID: 0000-0002-9762-6688)

ABSTRACT

INTRODUCTION

System reliability bounds refer to the theoretical limits or upper bounds on the reliability of a complex system. In engineering and reliability analysis, a system is considered reliable when it performs its intended functions satisfactorily over a specified time. System reliability is crucial in various fields, including aerospace, electronics, telecommunications, and critical infrastructure, where failures can have significant consequences.

Determining the exact reliability of a complex system can be challenging due to the interdependencies and interactions between its components. In many cases, it is impractical or even impossible to analyze all possible failure scenarios and calculate the exact reliability of the entire system.

To address this challenge, researchers and engineers use system reliability bounds as an approximation or estimation of the system's overall reliability. These bounds provide insight into the best- and worst-case scenarios for system reliability under certain assumptions.

Overall, system reliability bounds are a valuable tool in the evaluation and optimization of complex systems, providing insights into their performance and resilience.

The literature on system reliability bounds, particularly the works of Barlow and Proschan, is well regarded in the field of reliability engineering. "Statistical Theory of Reliability and Life Testing" is an influential work by Barlow and Proschan (1975). It covers statistical aspects of reliability engineering, including system reliability bounds. "Probabilistic Risk Assessment and Management for Engineers and Scientists" by Henley and Kumamoto (1996): This book covers risk assessment, including system reliability bounds, and has garnered significant attention in related research. "System Reliability Theory: Models, Statistical Methods, and Applications" by Rausand and Hoyland (2003): This book delves into various aspects of system reliability theory, including bounds and their applications, and has been cited widely in reliability research. "Reliability and Availability Engineering" by Trivedi and Bobbio (2017): This book provides a comprehensive treatment of reliability engineering, including discussions on reliability bounds for complex systems, and has garnered numerous citations. These works, among others, have been instrumental in shaping the field of reliability engineering and have influenced numerous researchers and practitioners interested in system reliability bounds and related topics. To obtain the most current and accurate information on highly cited articles, I recommend checking academic databases for citation statistics.

The purpose of this section is to introduce the bounds found in most system reliability books and to observe their advantages and disadvantages. Besides, two

new methods are proposed to obtain bounds using the Fréchet lower bound introduced by Fréchet (1951) and the monotony of system reliability. All the methods are studied in detail in the well-known example of a bridge structure.

BASIC CONCEPTS AND DEFINITIONS

Let $X_1, X_2, \cdots, X_n$ be binary random variables representing the operating states of the components of an n-component system. In addition, the operating state of the components should be independent of each other. In this case, the structure function showing the state of the system is also a bivariate random variable, and the operating state is a function of the operating states of the components. Thus, the structure function is expressed as

$$\phi(X_1, X_2, \cdots, X_n) = \begin{cases} 1, & \text{system is functioning} \\ 0, & \text{not functioning} \end{cases} \tag{1}$$

In this case, the system reliability is as follows:

$$h(\boldsymbol{p}) = h(p_1, p_2, \cdots, p_n) = \Pr(\phi(X_1, X_2, \cdots, X_n) = 1) \tag{2}$$

Here p_i $(i = 1,2, \cdots, n)$ represent component reliability.

It may be necessary to give the notation that we will use frequently:

$$(\cdot_i, x) = (x_1, x_2, \cdots, x_{i-1}, \ \cdot \ , x_{i+1}, x_{i+2}, \cdots, x_n) \tag{3}$$

Here the operating state of the component is expressed instead of the *i*th point.

Irrelevant Component

For all state vector x if *i*th component holds

$$\phi(1_i, x) = \phi(0_i, x), \tag{4}$$

component i is called an irrelevant component.

Two properties of the reliability function that we will use frequently are given below.

Pivotal Decomposition of the Reliability Function

Pivotal decomposition by component i is

$$h(\boldsymbol{p}) = p_i h(1_i, p) + (1 - p_i) h(0_i, p) \tag{5}$$

where $h(1_i, p) = \Pr(\phi(1_i, x) = 1)$ and $h(0_i, p) = \Pr(\phi(0_i, x) = 1)$.

Full pivotal decomposition is in the form of

$$h(\boldsymbol{p}) = \sum_{\boldsymbol{y}} \left(\prod_{j=1}^{n} p_j^{y_j} (1 - p_j)^{1-y_j} \right) \quad \phi(\boldsymbol{y}) \tag{6}$$

Here, the sum is taken over 2^n state vectors.

Monotonicity of the Reliability Function

Assuming that there is no outside interference in the operating state of the system, $h(\mathbf{0}) = 0$ and $h(\mathbf{1}) = 1$. It is also a non-decreasing function in each of its components. From equation (5), it is seen that the support set of $\boldsymbol{p}$ is assumed to be continuous then $\frac{\partial h(\boldsymbol{p})}{\partial p_j} \geq 0$. Logically, this property should also be provided for coherent systems due to its nature.

Minimal Path and Cut Representations of The Reliability Function

Let the system have minimal paths such as $\mathcal{P}_1$,$\mathcal{P}_2$,⋯,$\mathcal{P}_r$. The structure function corresponding to j. minimal path is represented by ρ_j. Then, the reliability function is expressed as

$$h(\boldsymbol{p}) = Pr\left(\coprod_{j=1}^{r} \rho_j(X) = 1 \right) = Pr\left(\coprod_{j=1}^{r} \prod_{l \in \mathcal{P}_j} X_l = 1 \right) \tag{7}$$

The system has minimal cuts such as $\mathcal{K}_1$ $\mathcal{K}_2$, ⋯ . $\mathcal{K}_m$ and the structure function corresponding to j. The minimal cut is denoted by k_j. Then the form of the reliability function can be written as

$$h(\boldsymbol{p}) = Pr\left(\prod_{j=1}^{m} k_j(X) = 1 \right) = Pr\left(\prod_{j=1}^{m} \coprod_{l \in \mathcal{K}_j} X_l = 1 \right) \tag{8}$$

Here, minimal path and minimal intersection sets have common elements as long as each of them does not contain a single element. $\rho_1, \rho_2, \cdots, \rho_r$ and $k_1, k_2, \cdots, k_m$ are sets of associated random variables. Therefore, the above

probabilities are difficult to write clearly. However, these equations can help obtain the lower and upper bounds for reliability.

RELIABILITY BOUNDS

The Inclusion-Exclusion Method

Let A_j denote the event that components in the jth minimal path are all successfully functioning state or jth minimal path is functioning state. The operation of the system is equivalent to the operation of at least one of the r minimal paths, that is, it depends on the occurrence of at least one of the events A_1,A_2,⋯,A_r. In this case, system reliability is represented by the union of these events such as

$$h(\boldsymbol{p}) = P\,r\left(\bigcup_{j=1}^{r} A_j\right) \tag{9}$$

According to probability theory, the following equation can be written for the probability of combining more than two events.

$$\begin{aligned}\Pr\left(\bigcup_{j=1}^{r} A_j\right) = &\sum_{j=1}^{r}\Pr(A_j) - \sum\sum_{i<j}\Pr(A_i \cap A_j) \\ &+ \sum\sum\sum_{i<j<k}\Pr(A_i \cap A_j \cap A_k) \\ &- \cdots (-1)^{r-1}\Pr\left(\bigcap_{j=1}^{r} A_j\right)\end{aligned} \tag{10}$$

Here, each probability included in the sum is calculated as follows:

$$\Pr(A_j) = \prod_{l\in\mathcal{P}_j} p_l \tag{11}$$

$$\Pr(A_i \cap A_j) = \prod_{l\in\mathcal{P}_i\cup\mathcal{P}_j} p_l \tag{12}$$

$$\Pr(A_i \cap A_j \cap A_k) = \prod_{l\in\mathcal{P}_i\cup\mathcal{P}_j\cup\mathcal{P}_k} p_l \tag{13}$$

$$\Pr\left(\bigcap_{j=1}^{r} A_j\right) = \prod_{l=1}^{n} p_l \tag{14}$$

The proof is based on combinatorial and binomial expansion (see, Dudewicz and Mishra, 1988). Accordingly, with reference to probability theory, the following expression can be written for the initial upper bound:

$$h(\boldsymbol{p}) \leq \sum_{j=1}^{r} \Pr(A_j) = S_1 \tag{15}$$

Then the lower bound is

$$S_1 - S_2 = \sum_{j=1}^{r} \Pr(A_j) - \sum\sum_{i<j} \Pr(A_i \cap A_j) \leq h(\boldsymbol{p}) \tag{16}$$

The second upper bound is

$$S_1 - S_2 \leq h(\boldsymbol{p}) \leq S_1 - S_2 + \sum\sum\sum_{i<j<k} \Pr(A_i \cap A_j \cap A_k) \tag{17}$$

The inclusion-exclusion process continues until a meaningful bound is obtained (the distance between the upper bound and the lower bound is narrow).

If a significant bound cannot be obtained, the bounds can also be obtained using the minimal cut sets.

The event B_j shall be defined as the failure of all components in the jth minimal cut set or the failure of jth minimal cut set. The failure of the system is equivalent to the failure of m minimal cut sets; that is, it depends on the occurrence of at least one of the events $B_1, B_2, \cdots, B_m$. Similarly the unreliability of the system is in the form of

$$1 - h(p) = \Pr\left(\bigcup_{j=1}^{m} B_j\right) \tag{18}$$

$$\Pr\left(\bigcup_{j=1}^{m} B_j\right) = \sum_{j=1}^{m} \Pr(B_j) - \sum\sum_{i<j} \Pr(B_i \cap B_j) + \sum\sum\sum_{i<j<k} \Pr(B_i \cap B_j \cap B_k) - \cdots (-1)^{m-1} \Pr\left(\bigcap_{j=1}^{m} B_j\right) \quad (19)$$

Here, probability calculations for unreliability respectively are

$$\Pr(B_j) = \prod_{l \in \mathcal{K}_j} q_l \quad (20)$$

$$\Pr(B_i \cap B_j) = \prod_{l \in \mathcal{K}_i \cup \mathcal{K}_j} q_l \quad (21)$$

$$\Pr(B_i \cap B_j \cap B_k) = \prod_{l \in \mathcal{K}_i \cup \mathcal{K}_j \cup \mathcal{K}_k} q_l \quad (22)$$

$$\Pr\left(\bigcap_{j=1}^{m} B_j\right) = \prod_{l=1}^{n} q_l \quad (23)$$

The lower and upper bounds can be obtained by an inclusion-exclusion method similar to the above.

Advantages

- Utilizing minimal paths and cut sets in the inclusion-exclusion principle provides a structured approach to estimate system reliability bounds. This approach can be computationally more efficient than considering all possible combinations of components.
- When employing the Fréchet lower bound in the construction of the control mechanism, a decision can be made regarding whether to traverse through the minimal cut or the minimal path.

Disadvantages

- In situations where the system reliability is high, the upper bound obtained with the minimal path approach may exceed one and the lower

bound may become negative. In such cases, it is advisable to favor the utilization of minimal cuts as an alternative approach.

- Extensive computations might be required. For instance, in a 4-out-of-5 system with high component reliabilities, it is beneficial to opt for the minimal cuts approach to establish bounds for unreliability. In this scenario, considering the presence of 10 minimal cuts, if a significant bound can be obtained in the first step, subsequent calculations involving 10+45=55 probabilities would be necessary. the number of components and minimal path (or cut) sets increases, the computational complexity can still become a challenge, especially for large and complex systems. In such cases, engineers may employ approximation techniques or advanced algorithms to efficiently estimate the reliability bounds.

Esary-Proschan Bounds

Let us define event D_j as the occurrence where at least one component in the jth minimal path fails to function, or jth minimal path fails to operate. In the context of the system's failure, it can be expressed as the intersection of events $D_1, D_2, \cdots, D_r$, signifying the non-operation of all r minimal paths. Accordingly, the unreliability of the system can be expressed as follows:

$$1 - h(p) = \Pr\left(\bigcap_{j=1}^{r} D_j\right) \tag{24}$$

With the help of conditional probability, we have

$$\Pr\left(\bigcap_{j=1}^{r} D_j\right) = \Pr(D_1)\Pr(D_2|D_1)\Pr(D_3|D_1 \cap D_2) \cdots \Pr(D_r|D_1 \cap D_2 \cap D_3 \cap \cdots \cap D_{r-1}) \tag{25}$$

On the other hand,

$$\Pr(D_2) = \Pr(D_2|D_1)\Pr(D_1) + \Pr(D_2|D_1^c)\Pr(D_1^c) \tag{26}$$

The upper bound for $\Pr(D_2|D_1^c)$ can be logically expressed as follows:

$$\Pr(D_2|D_1^c) = \coprod_{\substack{l\in\mathcal{P}_2 \\ l\notin\mathcal{P}_1}} q_l \leq \coprod_{l\in\mathcal{P}_2} q_l = \Pr(D_2) \tag{27}$$

If this result is substituted in the above equation (26) we have

$$\Pr(D_2) \leq \Pr(D_2|D_1)\Pr(D_1) + \Pr(D_2)\Pr(D_1^c) \tag{28}$$

Hence,

$$\Pr(D_2|D_1) \geq \Pr(D_2) \tag{29}$$

It is valid for all conditional probabilities in equation (25) and the lower bound for unreliability is

$$1 - h(\boldsymbol{p}) = \Pr\left(\bigcap_{j=1}^{r} D_j\right) \geq \prod_{j=1}^{r} \Pr(D_j) \tag{30}$$

Therefore, the upper bound for $h(\boldsymbol{p})$ is

$$h(\boldsymbol{p}) \leq 1 - \prod_{j=1}^{r} \Pr(D_j) = \coprod_{j=1}^{r} \Pr(D_j^c) = \coprod_{j=1}^{r} \prod_{l\in P_j} p_l \tag{31}$$

Let event E_j be defined as the occurrence where at least one component in the jth minimal cut set function, or the entire jth minimal cut set operates. The system's success corresponds to the operation of all m minimal cut sets, i.e., it is equivalent to the intersection of events $E_1, E_2, \cdots, E_m$. The system reliability can be expressed as follows:

$$h(\boldsymbol{p}) = \Pr\left(\bigcap_{j=1}^{m} E_j\right) \tag{32}$$

When the above results are used, a lower bound for $h(\boldsymbol{p})$ is obtained as follows:

$$h(\boldsymbol{p}) = \Pr\left(\bigcap_{j=1}^{m} E_j\right) \geq \prod_{j=1}^{m} \Pr(E_j) = \prod_{j=1}^{m} \coprod_{l \in \mathcal{K}_j} p_l$$
$$= \prod_{j=1}^{m} \left(1 - \prod_{l \in \mathcal{K}_j} (1 - p_l)\right) \tag{33}$$

Thus, we have Esary-Proschan (EP) lower and upper bounds for $h(\boldsymbol{p})$

$$\ell_{E-P}(\boldsymbol{p}) = \prod_{j=1}^{m} \left(1 - \prod_{l \in \mathcal{K}_j} (1 - p_l)\right) \leq h(\boldsymbol{p})$$
$$\leq 1 - \prod_{j=1}^{r} \left(1 - \prod_{l \in \mathcal{P}_j} p_l\right) = u_{E-P}(\boldsymbol{p}) \tag{34}$$

The the above-mentioned bounds have now been incorporated into almost all text books on reliability (see for example Barlow and Proschan, 1975 and Ross, 2014)

Advantages

- It is easy to calculate.
- The Esary-Proschan bounds can be applied to a wide range of systems with various configurations, including series, parallel, and complex interconnected systems. This flexibility allows them to be used in diverse engineering applications, such as electronics, aerospace, telecommunications, etc.

Disadvantages

- In cases of high reliability, the upper bound can expand, yet it remains significant.
- In situations of low reliability, the lower bound may turn out to be small; however, it remains significant.

Fu and Koutras (1995) employ the Esary-Proschan bounds, a computationally efficient approach, to estimate both upper and lower bounds on system reliability.

To overcome the mentioned disadvantages of Esary-Proschan bounds, the authors of the study have developed enhanced bounds.

Min-Max Method (with Fréchet Upper Bound)

The Fréchet bounds, based on the probability of the intersection of n events, are expressed as follows:

$$\max\left\{\sum \Pr(A_j) - n + 1,0\right\} \leq \Pr\left(\bigcap_{j=1}^{n} A_j\right) \leq \min\{\Pr(A_j)\} \tag{35}$$

(see, Fréchet, 1951). Considering the expression of the system reliability with minimal cut sets, i.e. equation (8), it corresponds to the intersection of m events m events. Then we have

$$\Pr(\phi(X) = 1) = \Pr\left(\prod_{j=1}^{m} k_j(X) = 1\right) = \Pr\left(\bigcap_{j=1}^{m}\{k_j(X) = 1\}\right) \tag{36}$$

The bound known as the Fréchet upper bound is

$$\min\{\Pr(k_1(X) = 1), \Pr(k_2(X) = 1), \cdots \Pr(k_m(X) = 1)\} \tag{37}$$

The probabilities of the events in the intersection (the jth-minimal cut is in a functioning state) are calculated as

$$\Pr(k_j(X) = 1) = 1 - \prod_{l\in\mathcal{K}_j} q_l = \coprod_{l\in\mathcal{K}_j} p_l \tag{38}$$

Accordingly, the upper bound is as follows:

$$\mathrm{h}(\mathbf{p}) \leq \min_{1\leq j\leq m}\left\{\coprod_{l\in\mathcal{K}_j} p_l\right\} = \mathcal{u}^{+}_{min-max}\ (\boldsymbol{p}) \tag{39}$$

Now let us remember the representation of the reliability of the system with a minimal path;

$$\Pr(\phi(X)=1)=\Pr\left(\coprod_{j=1}^{r}\rho_j(X)=1\right)=1-\Pr\left(\coprod_{j=1}^{r}\rho_j(X)=0\right) \quad (40)$$

Then, the probability on the right-hand side of (40) can be written as the intersection of r events such

$$\Pr\left(\coprod_{j=1}^{r}\rho_j(X)=0\right)=\Pr\left(\bigcap_{j=1}^{r}\{\rho_j(X)=0\}\right) \quad (41)$$

An upper bound for unreliability from the Fréchet upper bound can be written as follows:

$$\min\{\Pr(\rho_1(X)=0),\Pr(\rho_2(X)=0),\cdots,\Pr(\rho_r(X)=0)\} \quad (42)$$

The probability of each event (j.th minimal path not working) included in the intersection is calculated as follows:

$$\Pr\big(\rho_j(X)=0\big)=1-\Pr\big(\rho_j(X)=1\big)=1-\prod_{l\in\mathcal{P}_j}p_l \quad (43)$$

In this case, the lower bound for reliability is

$$\Pr(\phi(X)=1)\geq 1-\min_{1\leq j\leq r}\left\{1-\prod_{l\in\mathcal{P}_j}p_l\right\} \quad (44)$$

If the right-hand side of inequality (44) is rewritten with a more meaningful expression, it is obtained in the form of

$$\mathrm{h}(\mathbf{p})\geq \max_{1\leq j\leq r}\left\{\prod_{l\in\mathcal{P}_j}p_l\right\}=\ell^{+}_{\min-\max}(\boldsymbol{p}) \quad (45)$$

Advantages

- It can be calculated easily.

Disadvantages

- In very high and very low probabilities, the range of the bounds can be expanded.

Min-Max Method (with Fréchet Lower Bound)

Here we propose a new boundary. There will also be a control mechanism for the inclusion-exclusion method.

When equation (36) is taken into account, the lower bound of reliability obtained with the Fréchet lower bound is in the form of

$$\Pr\left(\bigcap_{j=1}^{m}\{k_j(X)=1\}\right) \geq \max\left\{\sum_{j=1}^{m}\Pr\left(\{k_j(X)=1\}\right)-m+1,0\right\} = \max\left\{1-\sum_{j=1}^{m}\left(\prod_{l\in K_j}q_l\right),0\right\} = \ell^{-}_{min-max}(\boldsymbol{p}) \tag{46}$$

Considering equation (36) again, the lower bound for unreliability is as follows:

$$\Pr\left(\bigcap_{j=1}^{r}\{\rho_j(X)=0\}\right) \geq \max\left\{\sum_{j=1}^{r}\Pr\left(\{\rho_j(X)=0\}\right)-r+1,0\right\} = \max\left\{1-\sum_{j=1}^{r}\left(\prod_{l\in \mathcal{P}_j}p_l\right),0\right\} \tag{47}$$

Hence, the upper bound for reliability can be obtained from Eq. (47) as follows:

$$h(\boldsymbol{p}) \leq 1-\max\left\{1-\sum_{j=1}^{r}\left(\prod_{l\in \mathcal{P}_j}p_l\right),0\right\} = min\left\{\sum_{j=1}^{r}\left(\prod_{l\in \mathcal{P}_j}p_l\right),1\right\} = \mathcal{u}^{-}_{min-max}(\boldsymbol{p}) \tag{48}$$

Accordingly, the reliability bounds obtained using the Fréchet lower bound are as follows:

$$\ell_{min-max}^{-}(\boldsymbol{p}) = \max\left\{1 - \sum_{j=1}^{m}\left(\prod_{l\in\mathcal{K}_j} q_l\right), 0\right\} \le h(\boldsymbol{p}) \le min\left\{\sum_{j=1}^{r}\left(\prod_{l\in\mathcal{P}_j} p_l\right), 1\right\} = u_{min-max}^{-}(\boldsymbol{p}) \tag{49}$$

Advantages

- Since it is expressed as the sum of individual probabilities in the inclusion-exclusion method, it can be effectively utilized as long as it is within the range of 0 and 1, providing a straightforward and concise representation.

Disadvantages

- It can provide non-significant bounds; however, when Fréchet upper and lower bounds are used together, it can yield more accurate results

New Reliability Boundary Proposal

Since $h(p)$ is a non-decreasing function in each component $\forall i$ the inequality

$$h(0_i, p) \le h(\boldsymbol{p}) \le h(1_i, p) \tag{50}$$

is valid. The improved reliability bound is obtained by considering the largest of the lower bounds and the smallest of the upper bounds across all components, as indicated by the last inequality. Accordingly, we have the following new bounds:

$$\min_{1\le i\le n}\{h(0_i, p)\} \le h(\boldsymbol{p}) \le \max_{1\le i\le n}\{h(1_i, p)\} \tag{51}$$

Advantages

- Unless there is a serial and parallel system, the lower limit does not reach zero and the upper limit does not reach 1.
- System boundaries are formed according to the reliability contribution of each component to the system.

Disadvantages

- When component reliabilities are low, the upper bound may not yield good results and when they are high, the lower bound may not yield good results.
- Taking into account the conditions when each component exactly works and when it does not work, it is necessary to repeatedly reconsider the system structure and perform reliability calculations multiple times.

APPLICATION TO THE BRIDGE EXAMPLE

This section discusses a well-known reliability system, namely bridge structures. The calculations of reliability boundaries and the full reliability assessment of the system will be performed and compared in cases of high component reliabilities, low component reliabilities, mixed component reliabilities, and when the reliabilities are equal.

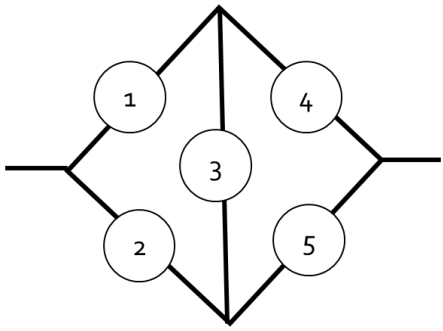

Figure1: Bridge Structure

The minimal paths of the system $\mathcal{P}_1 = \{1,4\}$are , $\mathcal{P}_2 = \{1,3,5\}$, $\mathcal{P}_3 = \{2,5\}$and $\mathcal{P}_4 = \{2,3,4\}$ and the minimal cuts are $\mathcal{K}_1 = \{1,2\}$, $\mathcal{K}_2 = \{2,3,4\}$, $\mathcal{K}_3 = \{1,3,5\}$and $\mathcal{K}_4 = \{4,5\}$.

Case 1 (High Component Reliabilities) Let the component reliability vector be respectively $\boldsymbol{p} = [0.98\ .99\ .995\ .97\ .96]'$.

Inclusion-Exclusion Method (Minimal Path)

Considering the above equations (11)-(14), the calculations are as follows: $S_1 = \sum_{j=1}^{4}\left(\prod_{l\in\mathcal{P}_j} p_l\right) = 3.7925945$, $S_2 = \sum\sum_{i<j}\left(\prod_{l\in\mathcal{P}_i\cup\mathcal{P}_j} p_l\right) = 5.490798478799999$, $S_3 = \sum\sum\sum_{i<j<k}\left(\prod_{l\in\mathcal{P}_i\cup\mathcal{P}_j\cup\mathcal{P}_k} p_l\right) = 3.595731955199999$and $S_4 = \prod_{l=1}^{5} p_l = 0.8989329888$. So the first bound is

$$S_1 - S_2 = -1.6982039788 \leq h(\boldsymbol{p}) \leq S_1 = 3.7925945 \quad (52)$$

It is a rather meaningless bound. Due to high reliabilities, improvement for the upper bound would be meaningless:

$$S_1 - S_2 = -1.6982039788 \leq h(\boldsymbol{p}) \leq S_1 - S_2 + S_3 = 1.8975279764. \quad (53)$$

In the next step, since the system's full reliability has been achieved, the method for obtaining boundaries through minimal paths did not yield good results.

$$h(\boldsymbol{p}) = S_1 - S_2 + S_3 - S_4 = 0.9985949876 \quad (54)$$

Inclusion-Exclusion Method (Minimal Cut)

Considering the above equations (20)-(23), the calculations are as follows:

$S_1 = \sum_{j=1}^{4}\left(\prod_{l\in\mathcal{K}_j} q_l\right) = 0.0014055$, $S_2 = \sum\sum_{i<j}\left(\prod_{l\in\mathcal{K}_i\cup\mathcal{K}_j} q_l\right) = 4.912000000000018 * 10^{-7}$, $S_3 = \sum\sum\sum_{i<j<k}\left(\prod_{l\in\mathcal{K}_i\cup\mathcal{K}_j\cup\mathcal{K}_k} q_l\right) = 4.800000000000021 * 10^{-9}$and $S_4 = \prod_{l=1}^{5} q_l = 1.200000000000005 * 10^{-9}$. So the first bound is

$$1 - S_1 = 0.9985945 \leq h(\boldsymbol{p}) \leq 1 - S_1 + S_2 = 0.9985949912 \quad (55)$$

As can be seen immediately, in the first step, significant values have been obtained for both lower and upper bounds.

E-P Bounds

For this initial case, we can state that the following equation can be written based on the above equations (30), (33) and (34) for the example of the bridge structure. In subsequent consecutive cases only the calculated values will be provided.

$$\ell_{E-P}(\boldsymbol{p}) = (1 - q_1q_2)(1 - q_1q_3q_5)(1 - q_2q_3q_4)(1 - q_4q_5) \quad (56)$$

as a result of calculations we have $\ell_{E-P}(\boldsymbol{p}) = 0.998594747704672$.

$$u_{E-P}(\boldsymbol{p}) = 1 - (1 - p_1p_4)(1 - p_1p_3p_5)(1 - p_2p_3p_4)(1 - p_2p_5) \quad (57)$$

It is obtained after calculations as $\mathcal{u}_{E-P}(\boldsymbol{p}) = 0.999993031949035$. Then E-P bounds are

$$0.998594747704672 \leq h(\boldsymbol{p}) \leq 0.999993031949035 \tag{58}$$

Min-Max Bounds (Fréchet Upper Bound)

Considering the above equations (39) and (45), we have

$$\ell^{+}_{\min-\max}(\boldsymbol{p}) = \max\{p_1p_4, p_1p_3p_5, p_2p_3p_4, p_2p_5\} \tag{59}$$

After calculations,

$$\begin{aligned}\ell^{+}_{\min-\max}(\boldsymbol{p}) &= \max\{0.9506, 0.936096, 0.9554985, 0.9504\} \\ &= 0.9554985\end{aligned} \tag{60}$$

The upper bound is obtained in the form of

$$\begin{aligned}\mathcal{u}^{+}_{min-max}(\boldsymbol{p}) &= \min_{1\leq j\leq 4}\left\{\coprod_{l\in\mathcal{K}_j} p_l\right\} = 1 - \max_{1\leq j\leq 4}\left\{\prod_{l\in\mathcal{K}_j} q_l\right\} \\ &= 1 - \max\{q_1q_2, q_1q_3q_5, q_2q_3q_4, q_4q_5\}\end{aligned} \tag{61}$$

If calculations are made using the equation above, $\max\{2.000000000000004 * 10^{-4}, 4.000000000000011 * 10^{-6}, 1.500000000000004 * 10^{-6}, 0.0012\} = 0.0012$. We have $\mathcal{u}^{+}_{min-max}(\boldsymbol{p}) = 0.9988$. Reliability bounds are obtained using the Fréchet upper bound as

$$0.9554985 \leq h(\boldsymbol{p}) \leq 0.9988 \tag{62}$$

Min-Max Bounds (Fréchet Lower Bound)

From Eqs. (46)-(49), we have the following calculations

$$\begin{aligned}\ell^{-}_{min-max}(\boldsymbol{p}) &= \max\left\{1 - \sum_{j=1}^{4}\left(\prod_{l\in K_j} q_l\right), 0\right\} = 1 - 0.0014055 \\ &= 0.9985945\end{aligned} \tag{63}$$

$$u_{min-max}^{-}(\boldsymbol{p}) = min\left\{\sum_{j=1}^{4}\left(\prod_{l\in\mathcal{P}_j} p_l\right), 1\right\} = \min\{3.7925945, 1\} = 1 \quad (64)$$

Here, the upper bound obtained using the Fréchet lower bound was not significant. (The first sum calculated using the inclusion-exclusion method with minimal paths is equal to this value.) It was obvious during the inclusion-exclusion calculation that the bound would not yield good results. In this case the limit

$$0.9985945 \leq h(\boldsymbol{p}) \leq \mathbf{1} \quad (65)$$

New Bounds

First, let us try to reveal the structure of the system when each component is considered to work individually:

$$\phi(1_1, \boldsymbol{X}) = X_4 \coprod (X_3X_5) \coprod (X_2X_3X_4) \coprod (X_2X_5) \quad (66)$$

The subsystem $X_2X_3X_4$ is redundant part as the 4th component is directly effective on the operation of the system alone. When this subsystem is discarded we have

$$\phi(1_1, \boldsymbol{X}) = X_4 \coprod (X_3X_5) \coprod (X_2X_5) = X_4 \coprod \big(X_5(X_2 \coprod X_3)\big) \quad (67)$$

Accordingly, reliability is

$$h(1_1, \boldsymbol{p}) = 1 - q_4(1 - p_2p_5 - p_3p_5 + p_2p_3p_5). \quad (68)$$

When the second component is definitely in operation, the structure function is as follows:

$$\phi(1_2, \boldsymbol{X}) = (X_1X_4) \coprod (X_1X_3X_5) \coprod (X_3X_4) \coprod X_5 \quad (69)$$

Here, the subsystem $X_1X_3X_5$ is redundant. According to that, when the redundant part is also removed, the structure function becomes as follows:

$$\phi(1_2, \boldsymbol{X}) = (X_1X_4) \coprod (X_3X_4) \coprod X_5 = X_5 \coprod \big(X_4(X_1 \coprod X_3)\big) \quad (70)$$

And reliability is

$$h(1_2, \boldsymbol{p}) = 1 - q_5(1 - p_1p_4 - p_3p_4 + p_1p_3p_4). \quad (71)$$

When the third component exactly works, the structure function is as follows:

$$\phi(1_3, \boldsymbol{X}) = (X_1X_4)\coprod(X_1X_5)\coprod(X_2X_4)\coprod(X_2X_5) = (X_1\coprod X_2)(X_4\coprod X_5) \quad (72)$$

The reliability of this system is

$$h(1_3, \boldsymbol{p}) = (p_1 + p_2 - p_1p_2)(p_4 + p_5 - p_4p_5) \quad (73)$$

Since the process steps are similar to the case when the first component is in operation, calculations for the fourth and fifth components proceed sequentially as follows:

$$\phi(1_4, \boldsymbol{X}) = X_1\coprod(X_1X_3X_5)\coprod(X_2X_3)\coprod(X_2X_5) = X_1\coprod\big(X_2(X_3\coprod X_5)\big) \quad (74)$$

And

$$h(1_4, \boldsymbol{p}) = 1 - q_1(1 - p_2p_3 - p_2p_5 + p_2p_3p_5). \quad (75)$$

$$\phi(1_5, \boldsymbol{X}) = (X_1X_4)\coprod(X_1X_3)\coprod(X_2X_3X_4)\coprod X_2 = X_2\coprod\big(X_1(X_3\coprod X_4)\big) \quad (76)$$

And

$$h(1_5, \boldsymbol{p}) = 1 - q_2(1 - p_1p_3 - p_1p_4 + p_1p_3p_4) \quad (77)$$

Now let us consider that the components are not working individually. The structure functions and corresponding reliabilities are as follows

$$\begin{gathered}\phi(0_1, \boldsymbol{X}) = (X_2X_3X_4)\coprod(X_2X_5), \\ h(0_1, \boldsymbol{p}) = p_2p_5 + p_2p_3p_4 - p_2p_3p_4p_5.\end{gathered} \quad (78)$$

And

$$\begin{gathered}\phi(0_2, \boldsymbol{X}) = (X_1X_4)\coprod(X_1X_3X_5), \\ h(0_2, \boldsymbol{p}) = p_1p_4 + p_1p_3p_5 - p_1p_3p_4p_5.\end{gathered} \quad (79)$$

and

$$\phi(0_3, \boldsymbol{X}) = (X_1X_4)\coprod(X_2X_5),$$
$$h(0_3, \boldsymbol{p}) = p_1p_4 + p_2p_5 - p_1p_2p_4p_5. \quad (80)$$

And

$$\phi(0_4, \boldsymbol{X}) = (X_1X_3X_5)\coprod(X_2X_5),$$
$$h(0_4, \boldsymbol{p}) = p_2p_5 + p_1p_3p_5 - p_1p_2p_3p_5. \quad (81)$$

And

$$\phi(0_5, \boldsymbol{X}) = (X_1X_4)\coprod(X_2X_3X_4),$$
$$h(0_5, \boldsymbol{p}) = p_1p_4 + p_2p_3p_4 - p_1p_2p_3p_4 \quad (82)$$

In this case, the lower bound is

$$\max\{h(0_1, \boldsymbol{p}), h(0_2, \boldsymbol{p}), h(0_3, \boldsymbol{p}), h(0_4, \boldsymbol{p}), h(0_5, \boldsymbol{p})\} \quad (83)$$

If necessary calculations are made, the calculated value of (83) is obtained as $\max\{0.98861994, 0.97868288, 0.99754976, 0.95976096, 0.96970997\} = 0.98861994$

For the upper bound we use

$$\min\{h(1_1, \boldsymbol{p}), h(1_2, \boldsymbol{p}), h(1_3, \boldsymbol{p}), h(1_4, \boldsymbol{p}), h(1_5, \boldsymbol{p})\} \quad (84)$$

When necessary calculations are made from eqs. (66)-(77) and (84), we have $\min\{0.99879856, 0.99879612, 0.99860024, 0.99979604, 0.99979853\} = 0.99860024$. Then reliability bounds

$$0.98861994 \leq h(\boldsymbol{p}) \leq 0.99860024. \quad (85)$$

Case 2 (Low Component Reliabilities) Let be the component reliability vector $\boldsymbol{p} = [0.1\ 0.2\ 0.01\ 0.3\ 0.05]'$.

Inclusion-Exclusion Method (Minimal Path)

$S_1 = 0.04065$, $S_2 = 0.000418$, $S_3 = 0.000012$ and $S_4 = 0.000003$. Accordingly, the first bound is as follows

$$S_1 - S_2 = 0.040232 \leq h(\boldsymbol{p}) \leq S_1 = 0.04065 \quad (86)$$

It is a very significant limit. It can be left as it without the need for second boundary improvement. According to the numerical values of summands, the complete reliability of the system is calculated as $h(\boldsymbol{p}) = S_1 - S_2 + S_3 - S_4 = 0.040241$.

Inclusion-Exclusion Bounds (Minimal Cut)

$S_1 = \sum_{j=1}^{4} \left(\prod_{l\in\mathcal{K}_j} q_l\right) = 2.78585$, $S_2 = \sum\sum_{i<j} \left(\prod_{l\in\mathcal{K}_i\cup\mathcal{K}_j} q_l\right) = 3.248127$, $S_3 = \sum\sum\sum_{i<j<k} \left(\prod_{l\in\mathcal{K}_i\cup\mathcal{K}_j\cup\mathcal{K}_k} q_l\right) = 1.896048$ and $S_4 = \prod_{l=1}^{5} q_l = 0.474012$. So the first bound is

$$1 - S_1 = -1.78585 \le h(\boldsymbol{p}) \le 1 - S_1 + S_2 = 1.462277 \tag{87}$$

It is a rather meaningless border. At the next bound improvement, the upper bound reaches system reliability. Even if the term S_3 is removed for improvement at the lower bound, we have to interrupt the processes here because it is negative.

E-P Bounds

We use the result of numerical calculations with the help of equations (56) and (57), then E-P bounds are obtained as follows:

$$0.006417972344 \le h(\boldsymbol{p}) \le 0.040324166191 \tag{88}$$

Min-Max Bounds (Fréchet Upper Bound)

From Eq. (59), $\ell^{+}_{\min-\max}$ is obtained in the form of

$$\ell^{+}_{\min-\max}(\boldsymbol{p}) = \max\{0.03, 0.00005, 0.0006, 0.01\} = 0.03 \tag{89}$$

Accordingly, from Eq. (61) $u^{+}_{min-max}$ is calculated as

$$u^{+}_{min-max}(\boldsymbol{p}) = 1 - \max\{0.72, 0.84645, 0.5544, 0.665\} = 0.15355 \tag{90}$$

Reliability bounds obtained using the Fréchet upper limit can be summarized as

$$0.03 \le h(\boldsymbol{p}) \le 0.15355 \tag{91}$$

Min-Max Bounds (Fréchet Lower Bound)

From the eq. (46), (48) and (49) lower and upper bounds can be determined directly as

$$\ell^{-}_{min-max}(\boldsymbol{p}) = 1 - 2.78585 = -1.78585 \tag{92}$$

$$u^{-}_{min-max}(\boldsymbol{p}) = \min\{0.04065,1\} = 0.04065 \tag{93}$$

Here, the lower bound obtained using the Fréchet lower bound was not significant. (The first sum calculated using inclusion-exclusion method with minimal intercepts is equal to this value.) It was obvious during processing the inclusion-exclusion calculations that the bound would not yield good results. In this case the limit

$$\mathbf{0} \leq h(\boldsymbol{p}) \leq 0.04065 \tag{94}$$

New Bounds

The calculated lower bound is $\max\{0.01057, 0.030035, 0.0397, 0.01004, 0.03054\} = 0.0397$. When the necessary calculations for the upper limit are made, we have $\min\{0.30728, 0.081065, 0.0938, 0.11071, 0.22456\} = 0.081065$. Reliability bounds are combined as

$$0.0397 \leq h(\boldsymbol{p}) \leq 0.081065. \tag{95}$$

Case 3 (Mixed Component Reliabilities) Let be the component reliability vector $\boldsymbol{p} = [0.1\ 0.9\ 0.5\ 0.8\ 0.2]'$.

Inclusion-Exclusion Bounds (Minimal Path)

$S_1 = 0.63$, $S_2 = 0.1466$, $S_3 = 0.0288$ and $S_4 = 0.0072$. So the first bound is

$$S_1 - S_2 = 0.4834 \leq h(\boldsymbol{p}) \leq S_1 = 0.63 \tag{96}$$

It is an acceptable bound. If an improvement is made for the upper bound

$$0.4834 \leq h(\boldsymbol{p}) \leq S_1 - S_2 + S_3 = 0.5122. \tag{97}$$

In the next step, the full reliability of the system is reached as

$$h(\boldsymbol{p}) = S_1 - S_2 + S_3 - S_4 = 0.505 \tag{98}$$

Inclusion-Exclusion Bounds (Minimal Cut)

$S_1 = 0.62$, $S_2 = \sum\sum_{i<j}\left(\prod_{l\in\mathcal{K}_i\cup\mathcal{K}_j} q_l\right) = 0.1466$, $S_3 = 0.0288$ and $S_4 = 0.0072$. Then the first bounds are

$$1 - S_1 = 0.38 \le h(\boldsymbol{p}) \le 1 - S_1 + S_2 = 0.5266 \tag{99}$$

It is a very significant limit. If improvement is made for the lower bound, bounds are given by

$$1 - S_1 + S_2 - S_3 = 0.4978 \le h(\boldsymbol{p}) \le 1 - S_1 + S_2 = 0.5266 \tag{100}$$

E-P Bounds

From equations (56) and (57), $\ell_{E-P}(\boldsymbol{p}) = 0.48432384$ and $\mathcal{u}_{E-P}(\boldsymbol{p}) = 0.52201216$. Then we have

$$0.48432384 \le h(\boldsymbol{p}) \le 0.52201216 \tag{101}$$

Min-Max Bounds (Fréchet Upper Bound)

$$\ell^{+}_{\min-\max}(\boldsymbol{p}) = \max\{0.08, 0.01, 0.36, 0.18\} = 0.36 \tag{102}$$

And

$$\mathcal{u}^{+}_{min-max}(\boldsymbol{p}) = 1 - \max\{0.09, 0.36, 0.01, 0.16\} = 0.63 \tag{103}$$

Reliability bounds are obtained using the Fréchet upper limit as

$$0.36 \le h(\boldsymbol{p}) \le 0.63 \tag{104}$$

Min-Max Bounds (Fréchet Lower Bound)

The result is reached using previous calculations as

$$\ell^{-}_{min-max}(\boldsymbol{p}) = 1 - 0.62 = 0.38 \tag{105}$$

$$u^{-}_{min-max}(\boldsymbol{p}) = \min\{0.63,1\} = 0.63 \tag{106}$$

In this case, the bounds are

$$0.38 \leq h(\boldsymbol{p}) \leq 0.63. \tag{107}$$

New Bounds

The value of the lower bound is obtained as $\max\{0.468, 0.082, 0.2456, 0.181, 0.404\} = 0.468$. When the necessary calculations for the upper limit are made, we have $\min\{0.838, 0.552, 0.7644, 0.586, 0.909\} = 0.552$. Hence we have followed bounds

$$0.468 \leq h(\boldsymbol{p}) \leq 0.552. \tag{108}$$

Case 4 (Equal Component Reliabilities) Under this situation, the calculations of the bounds will be obtained as a function of p. Let the component reliability be equal $\boldsymbol{p} = [p\ p\ p\ p\ p]'$.

Inclusion-Exclusion Bounds (Minimal Path)

$S_1 = 2p^2 + 2p^3$, $S_2 = 5p^4 + p^5$, $S_3 = 4p^5$ and $S_4 = p^5$. Then we have

$$\begin{gathered} 2p^2 + 2p^3 - 5p^4 - p^5 \leq h(p) \\ \leq \min\{2p^2 + 2p^3, 2p^2 + 2p^3 - 5p^4 + 3p^5\} \end{gathered} \tag{109}$$

The complete reliability of the system is $h(p) = 2p^2 + 2p^3 - 5p^4 + 2p^5$.

Inclusion-Exclusion Bounds (Minimal Cut)

$S_1 = 2q^2 + 2q^3$, $S_2 = 5q^4 + q^5$, $S_3 = 4q^5$ and $S_4 = q^5$ are obtained. Accordingly, the reliability bounds are

$$\begin{gathered} \max\{1 - 2q^2 - 2q^3, 1 - 2q^2 - 2q^3 + 5q^4 - 3q^5\} \leq h(p) \\ \leq 1 - 2q^2 - 2q^3 + 5q^4 + q^5 \end{gathered} \tag{110}$$

E-P Bounds

With the help of eqs. (56) and (57) $\ell_{E-P}(\boldsymbol{p}) = (1-q^2)^2(1-q^3)^2$ and $\mathcal{u}_{E-P}(\boldsymbol{p}) = 1-(1-p^2)^2(1-p^3)^2$ are obtained. Hence we have

$$(1-q^2)^2(1-q^3)^2 \leq h(\boldsymbol{p}) \leq 1-(1-p^2)^2(1-p^3)^2 \tag{111}$$

Min-Max Bounds (Fréchet Upper Bound)

$$\ell^{+}_{\min-\max}(\boldsymbol{p}) = \max\{p^2, p^3, p^3, p^2\} = p^2 \tag{112}$$

And

$$\mathcal{u}^{+}_{min-max}(\boldsymbol{p}) = 1-\max\{q^2, q^3, q^3, q^2\} = 1-q^2 \tag{113}$$

Reliability bounds are obtained using the Fréchet upper limit as

$$p^2 \leq h(\boldsymbol{p}) \leq 1-q^2 \tag{114}$$

Min-Max Bounds (Fréchet Lower Bound)

$$\ell^{-}_{min-max}(\boldsymbol{p}) = \max\{1-2q^2-2q^3, 0\} \tag{115}$$

$$\mathcal{u}^{-}_{min-max}(\boldsymbol{p}) = min\{2p^2+2p^3, 1\}\#(119)$$

$$\max\{1-2q^2-2q^3, 0\} \leq h(\boldsymbol{p}) \leq min\{2p^2+2p^3, 1\}. \tag{116}$$

New Bounds

$$h(1_1, \boldsymbol{p}) = h(1_2, \boldsymbol{p}) = h(1_4, \boldsymbol{p}) = h(1_5, \boldsymbol{p}) = 1-q(1-2p^2+p^3). \tag{117}$$

$$h(1_3, \boldsymbol{p}) = (2p-p^2)^2 \tag{118}$$

$$h(0_1, \boldsymbol{p}) = h(0_2, \boldsymbol{p}) = h(0_4, \boldsymbol{p}) = h(0_5, \boldsymbol{p}) = p^2+p^3-p^4. \tag{119}$$

$$h(0_3, \boldsymbol{p}) = 2p^2-p^4. \tag{120}$$

In this case, the lower bound is

$$\max\{p^2+p^3-p^4, 2p^2-p^4\} = 2p^2-p^4 \tag{121}$$

The upper bound is obtained as

$$\min\{1 - q(1 - 2p^2 + p^3), (2p - p^2)^2\} = (2p - p^2)^2 \qquad (122)$$

Then we have

$$2p^2 - p^4 \leq h(\boldsymbol{p}) \leq (2p - p^2)^2. \qquad (123)$$

Boundary calculations obtained from Case1-3 are summarized in Table1:

Table1: Reliability Bounds for Bridge Structure

Methods	Bounds
Case1	
Inclusion-Exclusion (Minimal Path)	--------
Inclusion-Exclusion (Minimal Cut)	[0.998594500000000, **0.998594991200000**]
E-P	[0.998594747704672, 0.999993031949035]
Min-Max (Fréchet upper bound)	[0.955498500000000, 0.998800000000000]
Min-Max (Fréchet lower bound)	[0.998594500000000, 1.000000000000000*]
New	[**0.988619940000000**, 0.998600240000000]
Case2	
Inclusion-Exclusion (Minimal Path)	[**0.040232000000**, 0.040650000000]
Inclusion-Exclusion (Minimal Cut)	--------
E-P	[0.006417972344, **0.040324166191**]
Min-Max (Fréchet upper bound)	[0.030000000000, 0.153550000000]
Min-Max (Fréchet lower bound)	[0.000000000000*, 0.040650000000]
New	[0.039700000000, 0.081065000000]
Case3	
Inclusion-Exclusion (Minimal Path)	[0.48340000, **0.51220000**]
Inclusion-Exclusion (Minimal Cut)	[**0.49780000**, 0.52660000]
E-P	[0.48432384, 0.52201216]
Min-Max (Fréchet upper bound)	[0.36000000, 0.63000000]
Min-Max (Fréchet lower bound)	[0.38000000, 0.63000000]
New	[0.46800000, 0.55200000]

*Appropriate value could not be obtained.

For Case 1, the new method has shown superior results for the lower bound, while the Inclusion-Exclusion (Minimal Cut) method has demonstrated superior results for the upper bound compared to others. For Case 2, the Inclusion-Exclusion (Minimal Path) method has provided more successful results for the lower bound, while the E-P method has demonstrated superior results for the upper bound compared to others. For Case 3, the Inclusion-Exclusion (Minimal Cut) method performs better for the lower bound, whereas the Inclusion-Exclusion (Minimal Path) method exhibits more significant results for the upper bound compared to other methods.

Since the graphical representation will gain more meaning for the interpretation of case 4, it is given as Figure 2-3 below.

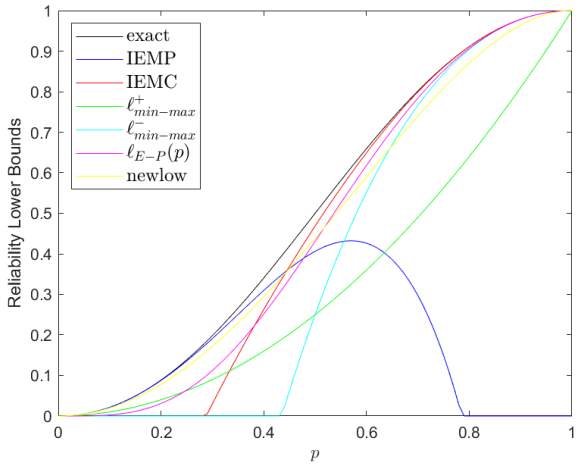

Figure2: Lower Bounds for the Bridge Structure

Inclusion-Exclusion with Minimal Path (IEMP) and new lower bound (newlow) give better results at small values of p. At large values of p, inclusion-exclusion with minimal cut (IEMC) and ℓ_{E-P} give better results, while IEMP and $\ell^{+}_{min-max}$ does not give better results.

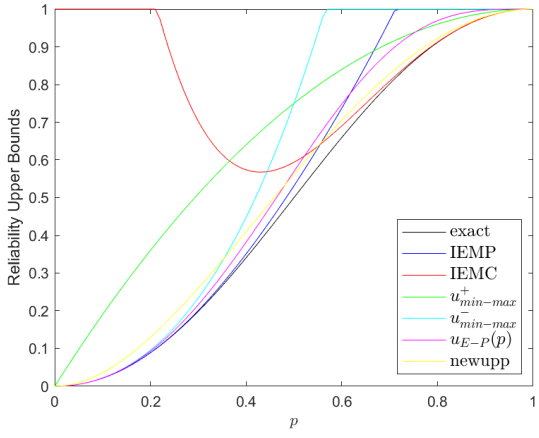

Figure3: Upper Bounds for the Bridge Structure

$u^{+}_{min-max}$, new upper bound (newupp) and $u^{-}_{min-max}$ does not give better results at small values of p. At large values of p, inclusion-exclusion with minimal cut (IEMC) and newupp give better results.

REFERENCES

Barlow, R. E., and Proschan, F. (1975). *Statistical theory of reliability and life testing: probability models* (Vol. 1). New York: Holt, Rinehart and Winston.

Dudewicz, E. J., and S. A. Mishra. (1988). *Modern Mathematical Statistics*. Wiley, New York

Fu, J. C., and Koutras, M. V. (1995). Reliability bounds for coherent structures with independent components. Statistics & probability letters, 22(2), 137-148.

Fréchet, M. (1951). Sur les tableaux de corrélation dont les marges sont données. Annales de l'Université de Lyon. Section A: Sciences mathématiques et astronomie 9: 53–77.

Henley, E. J., and Kumamoto, H. (1996). *Probabilistic risk assessment and management for engineers and scientists*. In IEEE Press.

Rausand, M., and Hoyland, A. (2003). *System reliability theory: models, statistical methods, and applications* (Vol. 396). John Wiley & Sons.

Ross, S. M. (2014). *Introduction to probability models*. Academic press.

Trivedi, K. S., and Bobbio, A. (2017). *Reliability and availability engineering: modeling, analysis, and applications*. Cambridge University Press.

Chapter 4

Animations in Chemistry Teaching

Aysel AYDIN KOCAEREN[1]

[1] Assoc. Prof. Dr; Çanakkale Onsekiz Mart University, Faculty of Education, Department of Mathematics and Science Education. aysel.kocaeren@comu.edu.tr, ORCID No: 0000-0003-4113-0517

ABSTRACT

INTRODUCTION

Many textbooks define what chemistry means in the introduction part of the course. In this section, the issues related to the fact that chemistry is an applied science rather than its definitions will be discussed in detail. It is mentioned that there is an applied science (chemisrty) at the end of the definitions made by centering the concept of matter. We can see this situation more clearly when we look at the output of the science of chemistry.

Chemistry Science and Teaching

In the early days, humans survived by trial and error methods. Some substances are harmful, some are useful, people firstly interacted with the substance at that time. The chemisrty science includes the development of techniques such as cooking and processing by people who use plants and animals as food. “How can I teach?” by transferring to other individuals of the knowledge learned during the education process or “How can I teach better?” the questions arise. As people developed, those who undertake the educational work in societies have developed a wide variety of methods and techniques for the teaching process. Teaching methods and techniques used in the education of chemistry are classified according to the time periods in which they are used in the field of education, taking into account the teaching of chemistry. For example, before the 1950s, after, and today. Since these methods and techniques are mentioned in the chemistry teaching programs or chemistry teaching courses of the programs that provide chemistry education, there is no need to explain in this section.

There are many published studies in the literature that the subjects inside units in the chemistry course are usually explained by the method of oral expression while transferring them to the student. In addition to this, it is very important in terms of learning how much the information explained is understandable by the recipient (student). In particular, to concretize abstract chemistry subjects, to make them understandable and to increase the memorability of the information facilitates the teacher's work in terms of teaching about the using of visual materials. According to the studies, all the steps taken to facilitate teaching and the used different methods lead to an increase in student success and a longer permanence of knowledge. Therefore, the quality and effectiveness of the materials that teachers can use are important during teaching chemistry.

While transferring the necessary information about the science of chemistry to the students, the students are passive in these methods. In order for learning to be more permanent and faster, it is necessary to ensure that the student

becomes active in order to receive the information. Many studies in recent years have shown that active learning methods within the framework of instructional technologies provide this.

The nature of chemistry includes the research process. Each individual creates this process in a unique way. In active learning, a research topic or question given to the student plays a role in reaching the targeted information. Inquiry-based learning provides opportunities for teachers and students to explore the natural world and use the obtained evidence that they obtain to test their perceptions (Alouf *et al*., 2003). In classrooms where inquiry-based learning is carried out, the student should be an active participant, not a passive listener. The most important behavior that students want to gain is that they learn to learn and grow up as lifelong learners, researchers and questioners (Sakar, 2010).

There are studies showing that students have difficulties in learning of chemistry. It is important to be informed about the readiness level of the student along with the method of expression applied in understanding of the subjects. The determination of this level at the beginning of each unit of the teacher will support the processing of the subjects in a planned and efficient manner. For example, some concepts and expressions such as molality, molarity, dissolution in the subject of solubility cannot be fully understood by the students. The fact that such conceptual expressions are not settled in the minds of the students is closely related to the inability to understand the subjects in the chemistry courses they take at higher levels, such as the construction of a building. Therefore, giving the concepts concrete in the early education period and taking into account the individual learning characteristics of the students will contribute to their solid-based chemistry learning.

Similarly, it was revealed that some conceptual expressions about acids and bases could not be understood by the students and they had misconceptions. In the textbooks published under the Ministry of National Education, the subject specified in the relevant unit is conveyed very well with visual materials and it is a research question why such problems are still experienced when it is explained by associating it with daily life.

Misconceptions seem to be an important problem in learning of chemistry, which is very common in chemistry. Especially in teacher-training institutions, teaching chemistry courses superficially or without adequately examining the subject, and explaining it without experimental application, paves the way for the emergence of misconceptions. In order for learning to be at the targeted level and meaningful, there should be no misconceptions (Akgün, 2001). The

use of materials is of great importance, especially during the teaching of the lessons, in eliminating of the misconceptions or preventing of their occurrence.

In the literature, a material prepared for students has been mentioned in order to eliminate the misconceptions about ionic bonds. Considering the misconceptions about ionic bonds, a guide material containing active learning activities with a constructivist approach was prepared and this material was used in learning the subject in the classroom environment. The researchers revealed that as a result of the application of the guide material developed about ionic bonds, the existing misconceptions of the students were eliminated to a great extent, and their analytical thinking, using information, and synthesizing capacities were increased (Kayalı & Tarhan, 2004).

In another study, it is related to the preparation of a guide material based on the constructivist theory for the subject of "Covalent Bonds". In the guide material, the researchers took care to give enough figures, photographs and graphics about the subject by prioritizing the why-why examination of the unit. They included cooperative learning activities and experimental applications, computer animations and reading passages.

After the application, they took the opinions of the students and teachers about the prepared guide material with the post-test and saw that the prepared guide material was successful in eliminating the misconceptions (Ürek & Tarhan, 2005).

Studies in the literature have also shown that efficient and effective teaching of chemistry lessons is directly related to the materials used. Accordingly, it is very important for students and teachers to use effective materials while teaching chemistry. Among the issues to be considered in the process of preparing the material to be used, the suitability of the material to the subject to be explained, the curriculum-subject teaching achievements and outputs can be listed as. It is very important to integrate the technology that we can reach today, as well as the materials prepared in the lectures of chemistry courses are suitable for the subject. Therefore, it is an inevitable fact that our teachers are also technology literate. We have seen the best example of this with the continuation of distance education in our country as well as in the whole world during the covid epidemic. We have witnessed that our teachers, who do not know how to use technology or are distant, have to learn applications in order to continue their lessons. The important conclusion to be drawn from this is that we cannot think of technology separately from education. Then let's talk a little bit about the use of technology in chemistry teaching.

Chemistry Teaching Technology

In the teaching of chemistry science, especially in recent years, with educational technology and products becoming more common, researches on effective learning and knowledge transfer have started to increase. In particular, since 21st century skills are technology-oriented, the question of how information technologies including modern teaching tools and innovative Technologies, can be used to support and enrich education, has led studies in the field of education and educational technology in recent years (Somyürek, 2014). With technology taking its place in the world of education, web 2.0 tools, animations, interactive virtual laboratories and artificial intelligence applications prepared for educational purposes have become the course materials that we use to embody abstract chemistry concepts.

The use of technology in the lessons (with videos, animations and visuals) and the integration of technology into the lesson (pre-planned and prepared applications) are different processes. Applications that are not within the pre-prepared plan in the use of technology in the lesson are randomly presented to the student in a part of the subject (teacher-centered). Applications that are not within the pre-prepared plan in the use of technology in the lesson are randomly presented to the student in a part of the subject (teacher-centered). In this case, the use of technology is hardly needed to complete low-level thinking tasks. In the integration of technology into the lesson, at which stage of the lesson and which acquisition will be supported the material to be used, it is determined by the teacher in advance. Thus, the technology is used by students as a part of the classroom environment to encourage higher-order thinking skills in a planned and purposeful (student-centered) way (Dinçer, 2020). The effect of technology on learning outcomes in education is only possible with the integration of technology into education. As mentioned above, it is important to increase the practical training that will be given to teachers about integrating technology into the lessons of chemistry teaching (Çolak Yazıcı, 2023).

In the study carried out by Kaya and Tarkın Çelikkıran in 2020, the use of instructional technologies in chemistry teaching was discussed and it was aimed to determine the views of chemistry teachers on the use of these technologies while conducting their classes. For this purpose, a qualitative study was carried out semi-structured interviews with 15 chemistry teachers in Patnos district of Ağrı city center. Content analysis method was used in the evaluation of the data obtained from the interviews. According to the results, the majority of chemistry teachers stated that the technological equipment of the schools they work in was insufficient and they could not benefit from them sufficiently because the technological devices were not maintained. Teachers participating

in the study stated that they generally use smart boards and that learning is more permanent and student success increases thanks to smart boards. Most of the teachers see themselves as inadequate in terms of technology use and they think that they need in-service training in order to improve themselves in terms of technology use. In addition, teachers generally stated that the curriculum could not direct them to the use of technology and the budgets allocated to instructional technologies were insufficient (Kaya & Tarkin-Celikkiran, 2020). As seen in this study, the application of technology in chemistry teaching is not only required by the supply of equipment, but also the teachers who will apply it must have sufficient knowledge and skills. In learning environments that include access to information and learning technologies, students discover their knowledge of chemistry through active learning. Thus, they can understand the chemistry more easily and structure their own knowledge in their minds (Ebenezer, 2001). In such learning environments, students actively try to produce, research, experiment and understand. Students find technological tools useful, such as video demonstrations, computer simulations, computer animations showing 3D molecular models (Byers, 1997). These technological tools increase student-student/teacher-student interaction and cooperation (Burke & Greenbowe, 1998; Sutherland, 2004).

Animations and Applications in Chemistry Teaching

Animation is created by connecting consecutive visuals. Animation can be created on anything you want to transfer. As mentioned above, animations can be prepared on topics that are especially difficult to understand or that may seem complicated to the other party (the buyer) while being explained. In addition, it is preferred to transfer information containing abstract expressions to the recipient (such as a student). Animation, in its general meaning, can be defined as the art of giving life and vitality to an object and the revitalization of reality or imagination in an animated style. Animation was defined as “creating many still images that show an object in motion and playing these images in rapid succession to make us think that the object is actually moving” (Bayram, 2012).

Animations are of great importance in teaching and learning the science of chemistry. Because it has the ability to embody and easily understand chemical events that cannot be directly perceived and described as abstract (Ardac & Akaygun, 2004). Animations facilitate the learning and later recall of events, concepts or principles that are difficult to visualize (Rieber, 1990). For example, it is stated that students can fully understand chemistry concepts when three-dimensional animations are used to show molecular structures and reaction

mechanisms (collisions, bond breaking and bond formation) (Ebenezer, 2001). Many studies on chemistry teaching on this subject reveal that it helps students in embodying the abstract, making invisible chemical events that cannot be visualized in the mind understandable, correcting misconceptions and facilitating concept learning (Pekdağ, 2010).

In the study conducted by Karaçöp *et al.* in 2009, the effect of computer animations on the academic achievement of students in the General Chemistry II course was investigated. A total of 122 first year science teaching students in three classes who took the General Chemistry-II course participated in the study, and two measurement tools, namely the Chemistry Academic Achievement Test and the Scientific Thinking Skill Test, were used in the same study. The teaching of the electrochemistry unit was carried out by using computer animation in the experimental groups and using the traditional lecture method in the control group. According to the results obtained in the study, it was concluded that the teaching of the course with the computer aided teaching method using computer animations is more successful than the traditional lecture method (Karaçöp *et al.*, 2009).

As can be seen in the above study, computer animation can be defined as the creation of motion graphics, pictures or visual effects by quickly displaying a series of images and pictures on the computer screen by using various computer software and graphic tools (Bayram, 2012; Tezcan & Yılmaz, 2003). The fact that the developments in computer and communication technology are also reflected in the field of animation makes animation applications easier on the computer (Arıcı & Dalkılıç, 2006). Instructional computer animations are built on moving, visual pictures of subjects and processes to help students better understand the subject. The correct presentation of the events in the science of chemistry is the first step in solving the teaching problem. It is also important for the presentation to be effective and to support the images with explanations as they form the basis of conceptual understanding (Bayram, 2012). The application of animations at any teaching level in chemistry is not common, so the need to develop such teaching materials is attractive for researchers.

In the study by Vermaat *et al.*, the use of animation in chemistry education was mentioned. A central issue in chemistry education is the relation between the macroscopic or real world and the molecular or nanoscopic world. New students could better understand chemistry and apply their chemistry understanding to solve problems if they were able to make deeper connections between these worlds. Animations can be used in chemical education so that students get a better knowledge of molecular processes by making better relations between the macroscopic and the nanoscopic world (Vermaat *et al.*,

2004). The study focuses on understanding the related subject of animations shown to different groups.

Examples of some animation figures created by student groups and shown to them in the work of Vermaat *et al.* are given below.

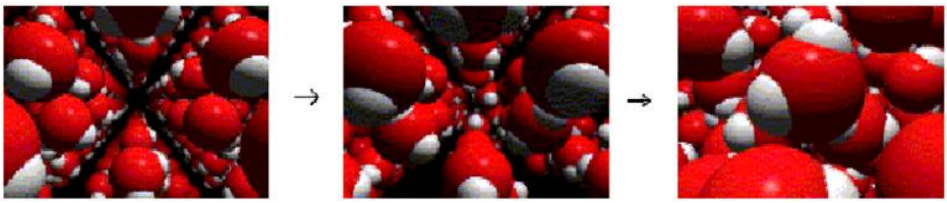

Figure 1: Frames from the animation 'Ice melting' (Vermaat *et al.,* 2004).

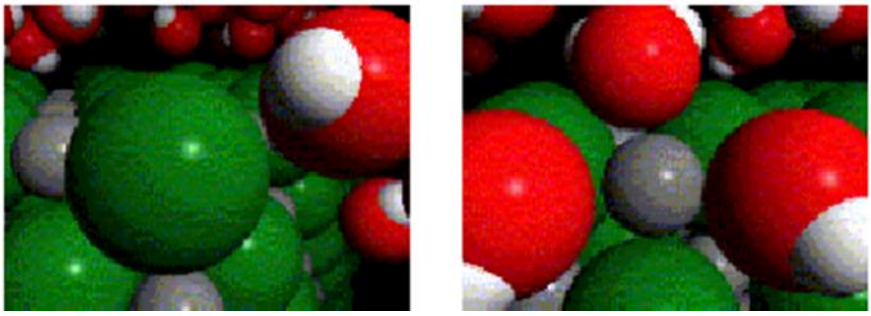

Figure 2: Frames from the animation 'Dissolving of salt' (Vermaat *et al*., 2004).

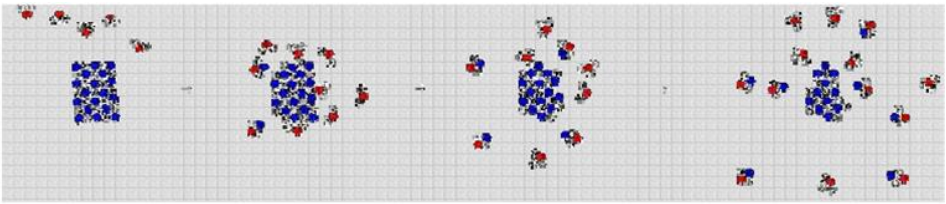

Figure 3: Frames from an animation made by a student of Group 4 (Vermaat *et al*., 2004).

In the study titled “The Effect of Animated Teaching on Science Teacher Candidates' Chemistry Achievements and Learning Persistence” by Yanarates in 2022, the purpose of this study was explained as determining the effect of teaching with animation on science teacher candidates' success in chemistry and learning retention (Yanarateş, 2022). The "General Chemistry Achievement Test" was used as a data collection tool, which developed by Sönmez (2017). According to the obtained results, the research conducted using nonparametric test techniques (Mann Whitney U and Kruskal Wallis) revealed a significant

positive difference in favor of the experimental group to which animation was applied. It is expected that this study will contribute to the studies in the field in accordance with the nature of animation, presentation and computer-assisted teaching method (Öztürk, 2021).

In 2007, Kelly and Jones investigated how animations at the molecular level about the dissolution of sodium chloride affect student explanations. To 18 university general chemistry students in small groups were dissolved in table salt in water and then two animations showing the dissolution of salt were watched to them. Students discussed animations in groups. Before and after watching each animation, students were asked to provide formal, written and verbal explanations about the chemical process at macroscopic and molecular levels. Related to this, the examples drawn by the students before and after watching the animations are given in Table 1 below.

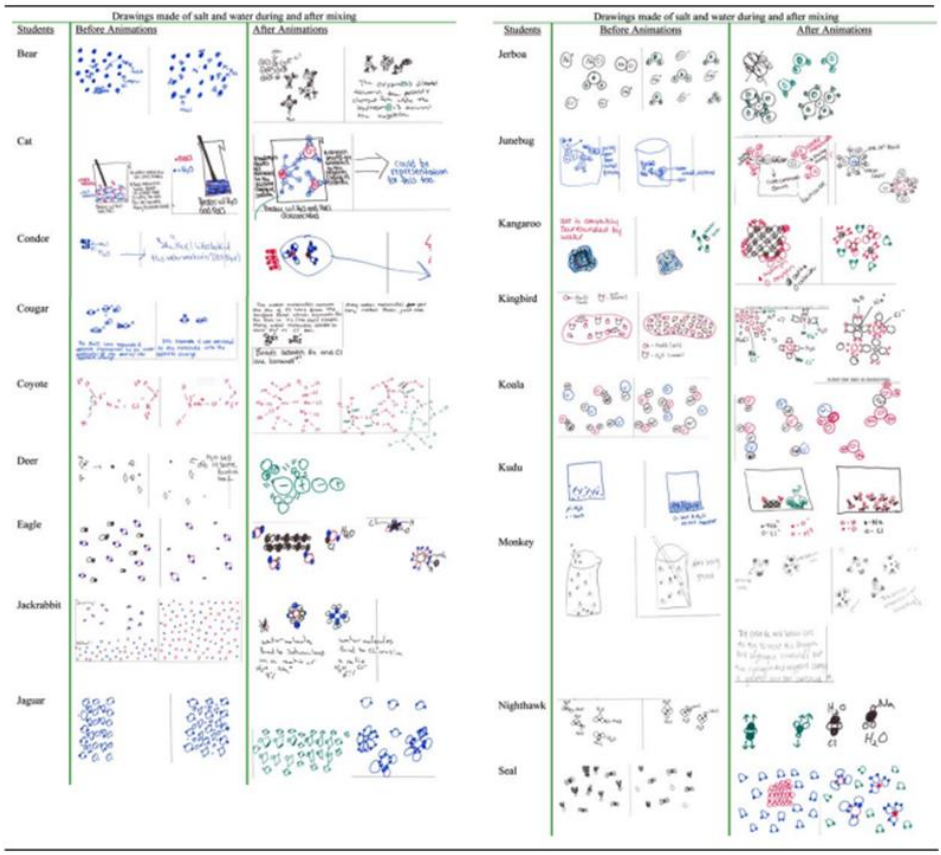

Table 1: Students' drawings before and after viewing the animations

Students exposed to animations included structural and functional features at the microscopic level in their explanations. After watching the animations,

positive and good developments were observed in student explanations. It is reported that animations benefit students in conceptual learning of the subject. While transferring the science of chemistry to the student, the desired information / message must appeal to the auditory and sensory organs, and the student must correctly code and learn by structuring the presented information in her mind.

Conclusion

Reaching permanent knowledge in teaching is the first step, so animations used as teaching materials have an important role. As can be seen in the examples given above, animations play an important role in the correct understanding of the conceptual expressions conveyed to the students by the students, and in delivering the information directly to the recipient without being exposed to any misconceptions or complexity. There are not many studies published under the title of animations in chemistry teaching in the literature, especially in our country. Existing animations offer a scientific field open to development and research, as they appeal to low grade levels and are for limited curriculum topics. It is very clear that animations to be prepared for general chemistry subjects, which are included in the curriculum of Higher Education Board at university level, will make great contributions to students.

References

Akgün, Ş. (2001). Fen bilgisi öğretimi (Geliştirilmiş Yedinci Baskı). *Giresun: Öncü Basımevi*, pp. 91-152.

Alouf, L. J. & Bentley, M. L. (2003). Assessing The Impact of InquiryBased Science Teaching in Professional Development Activities, *PK-12. Paper presented at the Annual Meeting of Association of the Teacher Educators* (Jacksonville, FL, February 17, 2003).

Arıcı, N. & Dalkılıç, E. (2006). Animasyonların bilgisayar destekli öğretime katkısı: Bir uygulama örneği. *Kastamonu Eğitim Dergisi*, 14(2): 421–430.

Ardac, D. & Akaygun, S. (2004). Effectiveness of multimedia-based instruction that emphasizes molecular representations on students' understanding of chemical change. *Journal of Research in Science Teaching*, 41(4): 317-337.

Bayram, K. (2012). Animasyon kullanımının öğretmen adaylarının genel kimya dersindeki erişilerine, tutumlarına ve kalıcılık düzeylerine etkisi. Necmettin Erbakan Üniversitesi Eğitim Bilimleri Enstitüsü İlköğretim Anabilim Dalı, Fen Bilgisi Eğitimi Bilim Dalı, Yüksek Lisans Tezi.

Burke, K. A. & Greenbowe, T. J. (1998). Collaborative distance education: The Iowa chemistry education alliance. *Journal of Chemical Education*, 75(10): 1308-1312.

Byers, D. N. (1997, April). So why use multimedia, the Internet, and lotus notes? Paper presented at the Technology in Education Conference, San Jose, CA. (ERIC Document Reproduction Service No. ED413023).

Çolak Yazıcı, S. (2023). Technology integration in chemistry education. In: Akpınar, A. (ed.), *Research on Mathematics and Science. Özgür Publications*.

Dinçer, S. (2020).Öğretim teknolojileri, Ankara, Pegem Akademi.

Ebenezer, J. V. (2001). A hypermedia environment to explore and negotiate students' conceptions: Animation of the solution process of table salt. *Journal of Science Education and Technology*, 10(1): 73-92.

Kaya, S. & Tarkin-Celikkiran, A. (2020). Investigation of teachers' views on the use of instructional technologies in chemistry teaching. *Trakya Journal of Education*, 10(3): 897-916.

Karaçöp, A., Doymuş, K., Doğan, A. & Koç, Y. (2009). The effects of computer animations and jigsaw technique on academic achievement of students, *GÜ, Gazi Eğitim Fakültesi Dergisi*, 29(1): 211-235.

Kayalı, H. A. & Tarhan, L. (2004). İyonik bağlar konusunda kavram yanılgılarının giderilmesi amacıyla yapılandırmacı-aktif öğrenmeye dayalı bir rehber materyal uygulaması. *Hacettepe Üniversitesi Eğitim Fakültesi Dergisi*, 27: 145-154.

Kelly, R. M. & Jones, L. L. (2007). Exploring how different features of animations of sodium chloride dissolution affect students' explanations. *Journal of Science Education and Technology*, 16(5): 413-429.

Öztürk, B. (2021). Uzaktan eğitimde STEM ve 21. yüzyıl becerileri. A. Yılmaz, B. Ertuğrul Akyol & M. N. Aydede (Eds.). Uzaktan eğitim sürecinde örnek etkinliklerle STEM uygulamaları içinde (s. 69- 95). Pegem Akademi Yayıncılık.

Pekdağ, B. (2010). Kimya öğreniminde alternatif yollar: animasyon, simülasyon, video ve multimedya ile öğrenme. *Journal of Turkish Science Education*, 7(2): 79-110.

Rieber, L. P. (1990). Using computer animated graphics in science instruction with children. *Journal of Educational Psychology*, 82: 135-140.

Sakar, Ç. (2010). Araştırmaya dayalı kimya öğretiminin öğrencilerin akademik başarı ve tutumları üzerine etkisi, Selçuk Üniversitesi Eğitim Bilimleri Enstitüsü Ortaöğretim Fen Ve Matematik Alanlar Eğitimi Anabilim Dalı Kimya Eğitimi Bilim Dalı, Yüksek Lisans Tezi.

Somyürek, S. (2014). Öğrenme sürecinde Z kuşağının dikkatini çekme: artırılmış gerçeklik. *Eğitim Teknolojisi Kuram ve Uygulama*, 4 (1): 63-80.

Sönmez, E. (2017). Argümantasyon tabanlı bilim öğrenme yaklaşımının fen bilimleri öğretmen adaylarının eleştirel düşünmelerine ve genel kimya başarılarına Etkisi [Yayımlanmamış doktora tezi]. Kastamonu Üniversitesi.

Sutherland, R. (2004). Designs for learning: ICT and knowledge in the classroom. *Computers & Education*, 43: 5-16.

Tezcan, H. & Yılmaz, Ü. (2003). Kimya öğretiminde kavramsal bilgisayar animasyonları ile geleneksel anlatım yöntemin başarıya etkileri. *Pamukkale Üniversitesi Eğitim Fakültesi Dergisi*, 14(2): 18-32.

Ürek, R. Ö. & Tarhan, L. (2005). Kovalent bağlar konusundaki kavram yanılgılarının giderilmesinde yapılandırmacılığa dayalı bir aktif öğrenme uygulanması. *Hacettepe Üniversitesi Eğitim Fakültesi Dergisi*, 28: 168-177.

Vermaat, H., Kramers-Pals, H. & Schank, P. (2004). The use of animations in chemical education. *Proceedings of the International Convention of the Association for Educational Communications and Technology*, *Anaheim*, pp. 430-441.

Yanarateş, E. (2022). The effect of animated teaching on science teacher candidates' chemistry achievements and learning persistence, *Educational Policy Analysis and Strategic Research*, 17 (1): 108-126.

Chapter 5

Optical and Structural Properties of Metal-Doped Copper Oxide Semiconductors

İlhan CANDAN[1]

Sezai ASUBAY[2]

[1] Dr. ; Dicle University, Science Faculty, Department of Physics.
ilhan.candan@dicle.edu.tr ORCID No: 0000-0001-9489-5324

[2] Prof. Dr.; Dicle University, Science Faculty, Department of Physics.
sezai.asubay@gmail.com ORCID No: 0000-0003-2171-8479

ABSTRACT

Metal-doped copper oxide semiconductors have emerged as a fascinating class of materials with tailored optical and structural properties, captivating researchers across a spectrum of scientific and technological domains. This chapter presents a comprehensive exploration of the intricate interplay between metal dopants and copper oxide matrices, focusing on their profound impact on optical and structural characteristics. In the realm of optical properties, the chapter unravels how metal dopants ingeniously engineer the absorption spectra and optical bandgaps of copper oxide semiconductors. Plasmonic phenomena arising from noble metal dopants open avenues for heightened light-matter interactions, pivotal in applications like photocatalysis and photovoltaics. Doping-induced defects induce luminescence, offering insights into the electronic structure and charge dynamics. Structurally, the chapter delves into crystal symmetry alterations, lattice parameter shifts, and defect formation brought forth by metal doping. The precise characterization techniques—ranging from X-ray diffraction to electron microscopy—unveil the nanoscale intricacies of these alterations. Defect engineering, coupled with judicious dopant incorporation, underscores the intricate mechanisms governing charge carrier behavior. Applications and prospects highlight the pivotal role of metal-doped copper oxide semiconductors across domains. Photocatalysis exploits efficient charge separation, while photovoltaics harness plasmonic effects. Gas sensing and optoelectronic devices capitalize on tailored optical properties. The chapter concludes with a call to ongoing research and innovation, underscoring the immense potential these materials hold for shaping modern technology landscapes. This chapter navigates the dynamic synergy between metal dopants and copper oxide semiconductors, elucidating their transformative potential in shaping a spectrum of applications from environmental remediation to advanced optoelectronics.

1. INTRODUCTION

Copper oxide (CuO) semiconductors have garnered significant attention in recent years due to their remarkable properties and wide range of applications in fields such as energy conversion (Johan, Suan, Hawari, & Ching, 2011; Septina et al., 2011), catalysis (Muhammad, Wu, El Kasmi, Muhammad, & Tian, 2023; Zabed et al., 2022), and optoelectronics (Patwary et al., 2022; Yadav, Sikarwar, Bhaduri, & Kumar, 2015). The introduction of metal dopants into copper oxide structures offers a powerful means to tailor their optical and structural characteristics, thus enabling fine-tuning for specific applications (Baturay, Candan, & Ozaydın, 2022; Candan, Gezgin, Baturay, & Kilic, 2022; Das & Alford, 2013; Kayani & Aslam, 2021; Mugwang'a, Karimi, Njoroge, Omayio, & Waita, 2012). This chapter aims to provide an in-depth exploration of the optical and structural properties of metal-doped copper oxide semiconductors, delving into their underlying mechanisms and potential applications.

2. OPTICAL PROPERTIES

The optical properties of materials are crucial in determining their interaction with light and electromagnetic radiation. In the context of metal-doped copper oxide semiconductors, these properties play a pivotal role in influencing their behavior in various applications.

Absorption and Bandgap Engineering

One of the key optical parameters of a semiconductor is its optical bandgap, which dictates the energy required for electrons to transition from the valence band to the conduction band (Escobar-Alarcón et al., 2007; Wang et al., 2014). Metal doping in copper oxide semiconductors can effectively modify the bandgap, leading to alterations in their absorption spectra(M. H. Babu, Podder, Dev, & Sharmin, 2020; M. M. H. Babu, Podder, Tofa, & Ali, 2021). The extent of bandgap engineering depends on the choice of metal dopant, concentration, and the resulting changes in the electronic structure. For instance, transition metal dopants such as iron (Fe), nickel (Ni), and cobalt (Co) have been known to induce shifts in the optical bandgap, enabling absorption of a broader range of wavelengths and enhancing the semiconductor's light-harvesting capabilities (Al-Amri et al., 2015; Basith, Vijaya, Kennedy, & Bououdina, 2013; Kabir, Ibrahim, Ayon, Billah, & Neaz, 2022).

CuO optical absorption can be analyzed by using the following expression (Erdoğan & Güllü, 2010):

$$\alpha h\nu = B\left(h\nu - E_g\right)^m \quad (1)$$

Where B is a constant, E_g is the band gap energy, and is thin film's absorption coefficient that can be calculated from optical absorbance. m is a caharacteristic number depending on the transition's nature; m = ½, 2, 3/2, or 3 for transitions of allowed direct, allowed nondirect, forbidden direct, or non direct, respectively.

Plasmonic Effects

Metal-doped copper oxide semiconductors can exhibit plasmonic effects, wherein the interaction between photons and free electrons in the metal dopants leads to enhanced light-matter interactions. This phenomenon is particularly significant in the visible and near-infrared regions of the electromagnetic spectrum. Plasmonic effects can result in increased light absorption, scattering, and localized electromagnetic field enhancements, which find applications in photocatalysis and photovoltaics (Chen, He, Huang, & Zhu, 2016; L. Lu, Luo, Xu, & Yu, 2013). Gold (Au) and silver (Ag) dopants, renowned for their strong plasmonic responses, have been integrated into copper oxide matrices to exploit these effects for enhanced photocatalytic degradation of pollutants and improved photovoltaic device efficiency.

Doping-Induced Defects and Optical Behavior

The introduction of metal dopants into copper oxide semiconductors often leads to the formation of defects within the crystal lattice (Devi, Sellaiyan, et al., 2017; Devi, Selvalakshmi, et al., 2017). These defects can significantly influence the optical behavior of the material by creating energy levels within the bandgap that facilitate charge carrier generation and recombination. Defect-induced optical transitions can result in the emission of visible light, giving rise to luminescence. By analyzing the luminescence properties of metal-doped copper oxide semiconductors, researchers can gain insights into defect concentrations, charge carrier dynamics, and electronic structure modifications.

3. STRUCTURAL PROPERTIES

The structural properties of metal-doped copper oxide semiconductors play a crucial role in determining their overall performance and behavior in practical applications. These properties encompass crystal structure, lattice parameters, and defect formation, among others.

Crystal Structure and Symmetry

Copper oxide semiconductors exhibit various crystal structures, with the most common being monoclinic or orthorhombic (Iqbal et al., 2019; Kumar et

al., 2021). Metal doping can lead to alterations in crystal symmetry and lattice parameters due to the size and charge differences between the dopant and host atoms. For instance, the incorporation of transition metal dopants can induce lattice distortions, affecting the material's electronic and optical properties. Understanding these structural changes is essential for tailoring the properties of metal-doped copper oxide semiconductors to meet specific application requirements.

Characterization Techniques

Characterizing the structural properties of metal-doped copper oxide semiconductors requires advanced analytical techniques. X-ray diffraction (XRD) is a widely used method for determining crystal structure and lattice parameters. XRD patterns can reveal shifts in diffraction peaks, indicative of changes in crystal symmetry or lattice constants due to metal doping (ur Rehman et al., 2021). Transmission electron microscopy (TEM) provides high-resolution images of the material's microstructure, enabling the visualization of defects, dopant distribution, and interfacial interactions at the nanoscale. Additionally, techniques such as X-ray photoelectron spectroscopy (XPS) and Raman spectroscopy offer insights into surface chemistry and vibrational modes, aiding in the identification of structural changes induced by metal dopants.

Defect Engineering and Dopant Incorporation

The introduction of metal dopants into copper oxide semiconductors introduces defects that can influence their electronic and optical properties. Dopants can occupy interstitial or substitutional positions within the crystal lattice, leading to the formation of new energy levels within the bandgap. These defect levels can act as trap states for charge carriers, affecting carrier mobility, recombination rates, and optical behavior. Controlling the type and concentration of defects through precise dopant incorporation strategies is essential for tailoring the material's performance for specific applications.

4. METAL-DOPANT TYPES AND EFFECTS

Metal dopants play a pivotal role in modulating the optical and structural properties of copper oxide semiconductors. The choice of dopant, its concentration, and its interaction with the host material significantly influence the resulting properties.

Transition Metal Dopants

Transition metal dopants, such as iron, cobalt, and nickel, have been extensively studied in copper oxide semiconductors (Khlifi et al., 2022; J. Lu et al., 2019). These dopants can induce various effects, including charge transfer, lattice distortion, and the formation of localized electronic states. The incorporation of transition metals can lead to changes in the electronic band structure, influencing the density of states near the Fermi level. This, in turn, affects the material's conductivity, optical absorption, and charge carrier dynamics. Transition metal dopants can also act as catalytic centers, enhancing the material's photocatalytic activity through surface redox reactions.

Noble Metal Dopants

Noble metals like gold and silver exhibit strong plasmonic responses, making them intriguing candidates for enhancing light-matter interactions in copper oxide semiconductors (Chang et al., 2012; Xu et al., 2020). When incorporated as dopants, noble metals can create localized surface plasmon resonances that enhance light absorption and scattering. This effect is particularly useful in applications where efficient photon absorption is crucial, such as in photovoltaic devices and photocatalysis. Additionally, noble metal dopants can influence the formation of defects and charge carrier behavior, further affecting the material's optical and electronic properties.

Rare Earth and Group III Dopants

Rare earth and Group III dopants, such as lanthanum (La), yttrium (Y), and indium (In), can introduce unique optical and structural characteristics to copper oxide semiconductors (Abu-Zied, Bawaked, Kosa, & Schwieger, 2016; Badawi et al., 2021; Gopalakrishnan & Ashokkumar, 2021). These dopants often possess large ionic radii, leading to lattice strain and modification of crystal symmetry. Rare earth dopants, in particular, can induce luminescence due to their characteristic energy levels and electronic transitions. The incorporation of these dopants can create energy states within the bandgap, influencing the material's optical absorption, emission, and charge carrier dynamics.

Dopant-Defect Interactions

The presence of dopants introduces new defect centers within the crystal lattice, affecting the material's overall electronic and optical behavior. Dopant-defect interactions can lead to the formation of shallow and deep energy levels, influencing charge carrier trapping, recombination, and migration. Understanding these interactions is crucial for harnessing the full potential of

metal-doped copper oxide semiconductors in applications such as gas sensors, photodetectors, and light-emitting devices.

5. APPLICATIONS AND FUTURE PROSPECTS

The tailored optical and structural properties of metal-doped copper oxide semiconductors offer exciting opportunities for various applications across different industries. The ability to manipulate these properties opens doors to innovative technological advancements.

Photocatalysis and Environmental Remediation

Metal-doped copper oxide semiconductors have demonstrated exceptional photocatalytic activity in degrading organic pollutants and pollutants through photocatalytic reactions (George et al., 2022; ur Rehman et al., 2021). The enhanced light absorption and charge carrier dynamics resulting from metal dopants facilitate efficient charge separation and redox reactions. This makes metal-doped copper oxide semiconductors promising candidates for wastewater treatment, air purification, and other environmental remediation processes.

Photovoltaics and Solar Energy Conversion

The plasmonic effects induced by noble metal dopants in copper oxide semiconductors present opportunities for enhancing photovoltaic device performance. Localized surface plasmon resonances can increase light absorption and generate hot electrons, potentially leading to improved energy conversion efficiencies (Azharudeen et al., 2022; Bhardwaj, Barman, & Kaur, 2016). Metal-doped copper oxide semiconductors can be integrated into solar cells, offering a route toward more efficient and cost-effective solar energy conversion technologies.

Gas Sensing and Sensing Technologies

The ability to modify the optical and structural properties of copper oxide semiconductors through metal doping has significant implications for gas sensing applications (Molavi & Sheikhi, 2020; Tang et al., 2018). Metal-doped copper oxide sensors can exhibit enhanced sensitivity and selectivity towards specific gas molecules, making them valuable tools for environmental monitoring, industrial safety, and medical diagnostics. The presence of dopant-induced defect sites can facilitate gas adsorption and chemical reactions, leading to detectable changes in electrical and optical properties.

Optoelectronic Devices and Light Emission

Metal-doped copper oxide semiconductors can be engineered for use in optoelectronic devices, such as light-emitting diodes (LEDs) and lasers(M. H. Babu et al., 2020; Jilani, Jlali, & Guermazi, 2021). The incorporation of dopants with luminescent properties can enable the generation and emission of light within specific wavelength ranges. This opens avenues for the development of energy-efficient lighting solutions, displays, and communication technologies.

6. CONCLUSION

In summary, the optical and structural properties of metal-doped copper oxide semiconductors offer a rich platform for tailoring their behavior to suit a wide range of applications. By carefully selecting dopants and controlling their incorporation, researchers can manipulate band structures, defect concentrations, and plasmonic effects to achieve desired functionalities. As ongoing research continues to uncover new insights into the interactions between metal dopants and copper oxide semiconductors, the potential for technological innovation in fields such as energy, catalysis, and optoelectronics remains promising.

REFERENCES

Abu-Zied, B. M., Bawaked, S. M., Kosa, S. A., & Schwieger, W. (2016). Impact of Gd-, La-, Nd-and Y-doping on the textural, electrical conductivity and N2O decomposition activity of CuO catalyst. *Int J Electrochem Sci, 11*(3), 2230-2246.

Al-Amri, S., Shahnawaze Ansari, M., Rafique, S., Aldhahri, M., Rahimuddin, S., Azam, A., & Memic, A. (2015). Ni-doped CuO nanoparticles: structural and optical characterizations. *Current Nanoscience, 11*(2), 191-197.

Azharudeen, A. M., Badhusha, A., Khan, M. S., Prabhu, S. A., Kumar, P. V., Karthiga, R., . . . Islam, M. R. (2022). Solar power light-driven improved photocatalytic action of Mg-doped CuO nanomaterial modified with polyvinyl alcohol. *Journal of Nanomaterials, 2022*.

Babu, M. H., Podder, J., Dev, B. C., & Sharmin, M. (2020). p to n-type transition with wide blue shift optical band gap of spray synthesized Cd doped CuO thin films for optoelectronic device applications. *Surfaces and interfaces, 19*, 100459.

Babu, M. M. H., Podder, J., Tofa, R. R., & Ali, L. (2021). Effect of Co doping in tailoring the crystallite size, surface morphology, and optical band gap of CuO thin films prepared via thermal spray pyrolysis. *Surfaces and Interfaces, 25*, 101269.

Badawi, A., Alharthi, S. S., Althobaiti, M. G., Alharbi, A. N., Assaedi, H., Alkhammash, H. I., & Al-Hosiny, N. (2021). Structure investigation and optical bandgap tuning of La-doped CuO nanostructured films prepared by spray pyrolysis technique. *Applied Physics A, 127*, 1-9.

Basith, N. M., Vijaya, J. J., Kennedy, L. J., & Bououdina, M. (2013). Structural, optical, and room-temperature ferromagnetic properties of Fe-doped CuO nanostructures. *Physica E: Low-dimensional Systems and Nanostructures, 53*, 193-199.

Baturay, S., Candan, I., & Ozaydın, C. (2022). Structural, optical, and electrical characterizations of Cr-doped CuO thin films. *Journal of Materials Science: Materials in Electronics, 33*(9), 7275-7287.

Bhardwaj, R., Barman, R., & Kaur, D. (2016). Improved photovoltaic effect in CuO/Zn1− xMgxO heterojunction solar cell by pulsed laser deposition. *Materials Letters, 185*, 230-234.

Candan, I., Gezgin, S. Y., Baturay, S., & Kilic, H. S. (2022). Structural, Morphological, Optical Properties and Modelling of Ag Doped CuO/ZnO/AZO Solar Cell. *Journal of Coating Science and Technology, 9*, 26-37.

Chang, C.-C., Hsu, C.-C., Chang, C.-T., Chen, Y.-P., Liaw, B.-J., & Chen, Y.-Z. (2012). Effect of noble metal on oxidative steam reforming of methanol over CuO/ZnO/Al2O3 catalysts. *International journal of hydrogen energy, 37*(15), 11176-11184.

Chen, M., He, Y., Huang, J., & Zhu, J. (2016). Synthesis and solar photo-thermal conversion of Au, Ag, and Au-Ag blended plasmonic nanoparticles. *Energy Conversion and Management, 127*, 293-300.

Das, S., & Alford, T. (2013). Structural and optical properties of Ag-doped copper oxide thin films on polyethylene napthalate substrate prepared by low-temperature microwave annealing. *Journal of applied physics, 113*(24).

Devi, L. V., Sellaiyan, S., Selvalakshmi, T., Zhang, H., Uedono, A., Sivaji, K., & Sankar, S. (2017). Synthesis, defect characterization, and photocatalytic degradation efficiency of Tb doped CuO nanoparticles. *Advanced Powder Technology, 28*(11), 3026-3038.

Devi, L. V., Selvalakshmi, T., Sellaiyan, S., Uedono, A., Sivaji, K., & Sankar, S. (2017). Effect of La doping on the lattice defects and photoluminescence properties of CuO. *Journal of Alloys and Compounds, 709*, 496-504.

Erdoğan, İ. Y., & Güllü, Ö. (2010). Optical and structural properties of CuO nanofilm: its diode application. *Journal of Alloys and Compounds, 492*(1-2), 378-383.

Escobar-Alarcón, L., Arrieta, A., Camps, E., Muhl, S., Rodil, S., & Vigueras-Santiago, E. (2007). An alternative procedure for the determination of the optical band gap and thickness of amorphous carbon nitride thin films. *Applied surface science, 254*(1), 412-415.

George, A., Raj, D. M. A., Venci, X., Raj, A. D., Irudayaraj, A. A., Josephine, R., . . . Chen, T.-W. (2022). Photocatalytic effect of CuO nanoparticles flower-like 3D nanostructures under visible light irradiation with the degradation of methylene blue (MB) dye for environmental application. *Environmental Research, 203*, 111880.

Gopalakrishnan, R., & Ashokkumar, M. (2021). Rare earth metals (Ce and Nd) induced modifications on structural, morphological, and photoluminescence properties of CuO nanoparticles and antibacterial application. *Journal of Molecular Structure, 1244*, 131207.

Iqbal, M., Ali, A., Ahmad, K. S., Rana, F. M., Khan, J., Khan, K., & Thebo, K. H. (2019). Synthesis and characterization of transition metals doped CuO nanostructure and their application in hybrid bulk heterojunction solar cells. *SN Applied Sciences, 1*, 1-8.

Jilani, W., Jlali, A., & Guermazi, H. (2021). Impact of CuO nanofiller on structural, optical, and dielectric properties of CuO/DGEBA hybrid nanocomposites for optoelectronic devices. *Optical and Quantum Electronics, 53*, 1-17.

Johan, M. R., Suan, M. S. M., Hawari, N. L., & Ching, H. A. (2011). Annealing effects on the properties of copper oxide thin films prepared by chemical deposition. *Int. J. Electrochem. Sci, 6*(12), 6094-6104.

Kabir, M. H., Ibrahim, H., Ayon, S. A., Billah, M. M., & Neaz, S. (2022). Structural, nonlinear optical and antimicrobial properties of sol-gel derived, Fe-doped CuO thin films. *Heliyon, 8*(9).

Kayani, Z. N., & Aslam, H. (2021). Investigation of structural, optical, antibacterial, and dielectric properties of V-doped copper oxide thin films: comparison with undoped copper oxide thin films. *Advanced Powder Technology, 32*(7), 2345-2358.

Khlifi, N., Mnif, S., Nasr, F. B., Fourati, N., Zerrouki, C., Chehimi, M., . . . Guermazi, S. (2022). Non-doped and transition metal-doped CuO nano-powders: structure-physical properties and anti-adhesion activity relationship. *RSC advances 12*(36), 23527-23543.

Kumar, P., Inwati, G. K., Mathpal, M. C., Ghosh, S., Roos, W., & Swart, H. (2021). Defects induced enhancement of antifungal activities of Zn doped CuO nanostructures. *Applied Surface Science, 560*, 150026.

Lu, J., Wang, J., Zou, Q., Zhao, Y., Fang, J., He, S., . . . Luo, Y. (2019). Catalytic performance of transition metals (Co, Ni, Zn, Mo) doped CuO-Ce0. 8Zr0. 2O2-based catalysts for CO preferential oxidation in H2-rich streams. *Journal of Alloys and Compounds, 784*, 1248-1260.

Lu, L., Luo, Z., Xu, T., & Yu, L. (2013). Cooperative plasmonic effect of Ag and Au nanoparticles on enhancing the performance of polymer solar cells. *Nano letters, 13*(1), 59-64.

Molavi, R., & Sheikhi, M. (2020). Facile wet chemical synthesis of Al-doped CuO nano leaves for carbon monoxide gas sensor applications. *Materials Science in Semiconductor Processing, 106*, 104767.

Mugwang'a, F., Karimi, P., Njoroge, W., Omayio, O., & Waita, S. (2012). Optical characterization of Copper Oxide thin films prepared by reactive dc magnetron sputtering for solar cell applications.

Muhammad, W., Wu, L., El Kasmi, A., Muhammad, A., & Tian, Z. (2023). Fe-Promoted Copper Oxide Thin-Film Catalysts for the Catalytic Reduction of N2O in the Presence of Methane. *Journal of Thermal Science, 32*(2), 531-541.

Patwary, M. A. M., Hossain, M. A., Ghos, B. C., Chakrabarty, J., Haque, S. R., Rupa, S. A., . . . Tanaka, T. (2022). Copper oxide nanostructured thin films processed by SILAR for optoelectronic applications. *RSC advances, 12*(51), 32853-32884.

Septina, W., Ikeda, S., Khan, M. A., Hirai, T., Harada, T., Matsumura, M., & Peter, L. M. (2011). Potentiostatic electrodeposition of cuprous oxide thin films for photovoltaic applications. *Electrochimica Acta, 56*(13), 4882-4888.

Tang, Q., Hu, X.-B., He, M., Xie, L.-L., Zhu, Z.-G., & Wu, J.-Q. (2018). Effect of platinum doping on the morphology and sensing performance for CuO-based gas sensor. *Applied Sciences, 8*(7), 1091.

ur Rehman, A., Aadil, M., Zulfiqar, S., Agboola, P. O., Shakir, I., Aboud, M. F. A., . . . Warsi, M. F. (2021). Fabrication of binary metal doped CuO nanocatalyst and their application for the industrial effluents treatment. *Ceramics International, 47*(5), 5929-5937.

Wang, Y., Miska, P., Pilloud, D., Horwat, D., Mücklich, F., & Pierson, J. (2014). Transmittance enhancement and optical band gap widening of Cu2O thin films after air annealing. *Journal of Applied Physics, 115*(7).

Xu, H., Liu, T., Bai, S., Li, L., Zhu, Y., Wang, J., . . . Huang, X. (2020). Cation exchange strategy to single-atom noble-metal doped CuO nanowire arrays with ultralow overpotential for H2O splitting. *Nano letters, 20*(7), 5482-5489.

Yadav, B., Sikarwar, S., Bhaduri, A., & Kumar, P. (2015). Synthesis, characterization, and development of optoelectronic humidity sensor using copper oxide thin film. *Synthesis, 2*(11).

Zabed, H. M., Islam, J., Chowdhury, F. I., Zhao, M., Awasthi, M. K., Nizami, A.-S., . . . Qi, X. (2022). Recent insights into heterometal-doped copper oxide nanostructure-based catalysts for renewable energy conversion and generation. *Renewable and Sustainable Energy Reviews, 168*, 112887.

Chapter 6

An Overview of Structure-Activity Relationships in N-Substituted Piperazines as Anticancer and Antidepressant Agents

Sümeyya SERİN[1]

[1] Dr..; Inonu University, Scientific and Technological Research Center.
sumeyya.alatas@inonu.edu.tr ORCID No: 0000-0002-4637-1734

ABSTRACT

Piperazines (1,4-diazacyclohexane) are the most frequently studied class of compounds in heterocyclic chemistry due to their pharmacological importance. Namely, there are many commercial drugs that contain a piperazine core in their structure since they show pharmacological activity in a very wide area. On the other hand, the applications of piperazine derivatives are not limited to the medical field. It is possible to encounter this core in the structure of several agrochemicals.

One of the most common health problems in the world today is cancer and the other is depression. Moreover, both disorders trigger each other. In order to fight these diseases, the discovery studies of more effective drug candidates without undesirable side effects continue to increase day by day. In this context, N-substituted piperazine derivatives have been included in many studies in recent years, considering their broad-spectrum properties. Studies on the determination of pharmacological activity have mostly been accompanied by structure-activity relationships (SAR). SAR, the prediction of bioactivity from structural characteristics, is an important parameter in applied chemistry as it guides the design and discovery studies of new compounds. With these considerations in mind, encouraged by the success of piperazines in therapeutic areas, this study deals with the anticancer and antidepressant applications of N-substituted piperazine derivatives in recent years.

Keywords: Heterocycles, Piperazine, Bioactivity, Structure-Activity Relationship, anticancer

INTRODUCTION

Piperazine (**1**), a crucial heterocyclic motif, has inspired the design and synthesis of new bioactive derivatives in the field of synthetic chemistry because of its symmetry and two nitrogen atoms (Bugaenko, 2017:1277; Solomon et al., 2010:1563). Although it is known that piperazine itself is mainly used as a drug against gout and helminthiasis, its derivatives have not been used for this purpose (Elliott, 2011:430). Namely, piperazine is more commonly used as a building block in drug design studies. For more than two decades, numerous N-substituted piperazine derivatives have been synthesized and their various pharmacological activities have been reported. Especially, anticancer (Akkoç et al., 2012:515; Chen et al., 2010:96) antifungal (Chandrika et al., 2018:158), anti-inflammatory (Migliore et al., 2016:11359), antidiabetic (Tamayo et al., 2015:4462), antidepressant (Ahmed et al., 2012:872), antimalarial (Ibezim et al., 2012:81), anti-Alzheimer (Sergeant et al., 2019:217), anticonvulsant (Mukherjee et al., 2014:567) activities can be cited as examples (Figure 1). The fact that N-substituted piperazine derivatives show a wide range of activities has greatly increased the interest in this field. From this point of view, in this study, the important advances of N-substituted piperazine derivatives in two selected areas (anticancer and anti-depressant) are systematically discussed. At the same time, insights into the structure-activity relationships of piperazine analogs that can guide the design and discovery process of new drug candidates are presented.

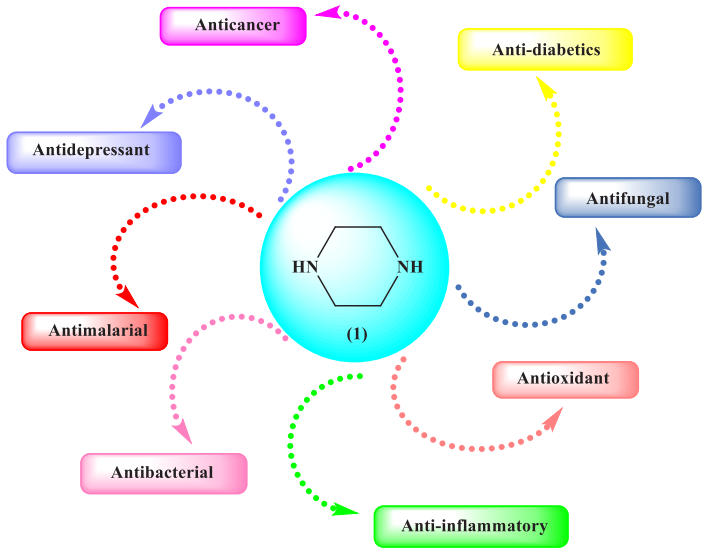

Figure 1: Various Pharmacological Activities of Piperazine Core

Pharmacological Activities of N-Substituted Piperazines

Anticancer Activity

Cancer is a term that defines diseases that occur when cells divide uncontrollably and spread to surrounding tissues. It is also one of the leading causes of death occurring worldwide (Hu et al., 2022:113963). Statistics from the International Agency for Research on Cancer (IARC) indicate that around ten million people worldwide died of cancer in 2020 (Bray et al., 2018:394). This number is increasing day by day. This is why for many years; mankind has been trying to develop effective drugs that can prevent these deaths. On the other hand, despite the use of a wide variety of anticancer drugs in the treatment, increasing resistance to the drugs leads to the failure of chemotherapy. This case reveals the importance of design and discovery studies of effective and selective new anticancer agents with less side effects and low toxicity. In Table 1, some prominent studies in recent years are summarized with their outlines. Besides, some anticancer agents containing piperazine core are depicted in Figure 2 with their chemical structures and IUPAC names.

Table 1: Some Selected Studies on the Anticancer Activities of N-Substituted Piperazines

Aim	Model	Findings
To synthesize various phenolic mono Mannich bases including piperazine motif and to investigate their anticancer activities (Tuğrak et al., 2019:103095)	* Cytotoxicity evaluation * Cell cycle analysis * Carbonic anhydrase enzyme assay * Statistical treatment	Among the five newly synthesized derivatives, the highest TS_2 value (Tumor Selectivity, 59.4) against Ca9-22 cells. was calculated for the derivative containing p-fluorophenyl piperazine group. It is considered that the related compound will be the lead compound for further studies.
To synthesize new 2-benzoylbenzofuran derivatives containing piperazine group and to investigate their anticancer activities (Gao et al., 2019:806)	* In vitro anticancer activity * Evaluation of Apoptosis	A series of new derivatives have been synthesized via aldol condensation and substitution reactions. Among the synthesized compounds, it was determined that the derivatives containing the keto-substituent showed the most anticancer activity. In particular, the SAR study demonstrated that the presence of electron donating substituents increased anticancer activity.
To synthesize rhein-piperazine-dithiocarbamate hybrids and to investigate their anticancer activities against human cancer cells (Wei et al., 2022:114651)	* In vitro cytotoxic activity * Cell apoptosis evaluation * In vivo safety evaluation	SAR analysis performed after a successful synthesis and structure characterization study revealed that the inclusion of ester groups in the structure promotes anticancer activity.
To investigate the effects of piperazine selenium nanoparticles (Pipe@SeNP's) in breast cancer cell lines	* In Silico ADME analysis * Molecular Docking * MTT dye reduction assay * Cytotoxic assay	The results obtained indicate that Pipe@SeNP's can be used for cytotoxic effect on cancer cells. In addition, it was determined that the viability of normal cells

(Prasad et al., 2022:133683)	* Colony-forming assay * Cell migration assay * Evaluation of Apoptosis	was not affected much, that is, it had a protective effect.
To synthesize phthalazine-piperazine-1,2,4-oxadiazole derivatives and to investigate their anticancer activities against human cancer cells (MCF-7, breast cancer; A549, lung cancer; DU-145; prostate cancer) (Samala et al., 2022)	* In vitro anticancer activity * Molecular Docking * In vitro tyrosine kinase EGFR inhibitory activity * In Silico ADMET analysis	Among the 14 derivatives obtained with a yield of 50-78%, promising results were revealed in the anticancer studies of 4 of them. The substituents of the mentioned 4 derivatives are 4-NO_2, 3, 5-diNO_2, 3-NO_2 and 4-CN groups. In addition, molecular docking studies have predicted that the derivative containing the 3, 5-diNO_2 substituent binds strongly to the EGFR protein.
To synthesize new coumarin-piperazine derivatives and to evaluate their in vitro bioactivities (Patel et al., 2023:134755)	* Anticancer activity against MCF-7 * Molecular Docking * MD simulation * In Silico ADME analysis	Within the scope of the study, eleven new compounds were synthesized and their structures were elucidated. It was determined that the derivative containing 4-benzhydrylpiperazine substituent exhibited quite good activity against MCF-7 cell line. It was concluded that derivatives containing mono and di-chlorine did not show activity against breast cancer cells.
To synthesize new nitrobenzoxadiazole-piperazine hybrids and to evaluate their in vitro anticancer activities against MCF-7, HepG2, and A549 cells (Chen et al., 2023:133393)	* In vitro anti-proliferative activity *Flow cytometric analysis of apoptosis * Western blotting analysis * Colony formation * Cell migration	The activities of the synthesized hybrids against breast, liver and lung cancer cell lines were investigated. Almost all of the 23 new derivatives showed a moderate activity. It has been determined that the derivative containing 4-chloromethylphenyl substituent is highly effective against all three cancer cells. IC_{50} values against MCF-7, HepG2 and A549 cells were determined as 7.58, 3.50 and 4.73 μM, respectively. It was concluded that the mentioned compound is promising as an anticancer agent.
To synthesize novel benzofuran-piperazine derivatives and to evaluate their anticancer activities (Schumacher et al., 2023:129425)	* In vitro anti-proliferative activity * Colony formation * Evaluation of Apoptosis	It was determined that most of the compounds synthesized by choosing electron-withdrawing and electron-donating groups as substituents displayed good cell proliferation inhibition.
To synthesize piperazine-substituted silicon phthalocyanines (Sipc) and to evaluate their anticancer activities (Nalçaoğlu et al., 2022:102734)	* Photodynamic therapy application * Cell viability assay * Evaluation of Apoptosis * Determination of ROS generation * Long-term colony formation assay * In vitro scratch assay * Western blotting analysis * Statistical analysis	Two new piperazine-substituted silicon phthalocyanine derivatives were successfully synthesized and their structures elucidated by FTIR, UV–vis, LC–MS/MS, MALDI–TOF and NMR spectroscopy. The analysis results reveal that both derivatives can exhibit selective cytotoxic effects on breast cancer cells.
To synthesize N-acyl substituted indole based piperazine, thiazole and	* Antibacterial activity studies * Antifungal activity	N-acyl indole-based piperazine, tetrazole, and thiazole derivatives were successfully synthesized and their structures elucidated.

tetrazoles derivatives and to evaluate their bioactivity properties (Jagadeesan and Karpagam, 2023:134013)	studies * Antioxidant activity studies * Cytotoxic activity studies * Molecular Docking	The bioactivity evaluation concluded that the newly synthesized derivatives showed higher cytotoxic activity than the doxorubicin standard (lower IC_{50} value).
To synthesize novel triazole–piperazine derivatives (Mishra et al., 2017:753)	* In vitro cytotoxicity studies * Evaluation of Apoptosis * Determination of ROS generation * In vivo anticancer action * Toxicity Evaluation	Twelve new derivatives with a wide variety of substituents have been synthesized. The newly synthesized hybrid molecules were determined to exhibit moderate to excellent cytotoxicity against studied cell lines. The most effective results were obtained with benzoyl group substitution in in vivo and in vitro models. On the other hand, it was determined that the derivative containing electron-donating methyl substitution on the phenyl ring could not produce effective cytotoxicity.
To synthesize benzenesulfonyl piperazine derivatives and to investigate their pharmacological activities (Nandi et al., 2023:134671)	* Cytotoxic activity studies * In Silico ADME analysis * Molecular Docking	Within the scope of the study, sixteen new derivatives were synthesized and their structures were characterized. For cytotoxicity studies, 4 derivatives with high hMAO inhibitory potential were selected and their effects against SH-SY5Y cells were evaluated. Mentioned derivatives contain -$CH_2C_6H_5$, $C(CH_3)_3$, CH_3, and -2,5-di$CH_3C_6H_5$ as substituents. Since low IC_{50} values were recorded for these compounds, it can be stated that these compounds are not toxic to SH-SY5Y neuronal cells.
To synthesize benzimidazole-based piperazine derivatives and to examine their cytotoxicity against human breast cancer cell lines (Ambala et al., 2023: e202302393)	* Molecular Docking * In Silico ADME analysis * Cytotoxicity Screening * Morphological Screening	14 new benzimidazole-piperazine derivatives were synthesized and their structures were characterized by several spectroscopic methods. The 4-(trifluoromethyl)benzyl substituted derivative (IC_{50} =7.29±0.20 μM and 6.92±4.80 μM) exhibited the strongest activity against MCF-7 and MDA-MB-231 cell lines. It has been reported that no negative impacts were observed in toxicity tests. Besides, molecular docking studies have confirmed the experimental findings.

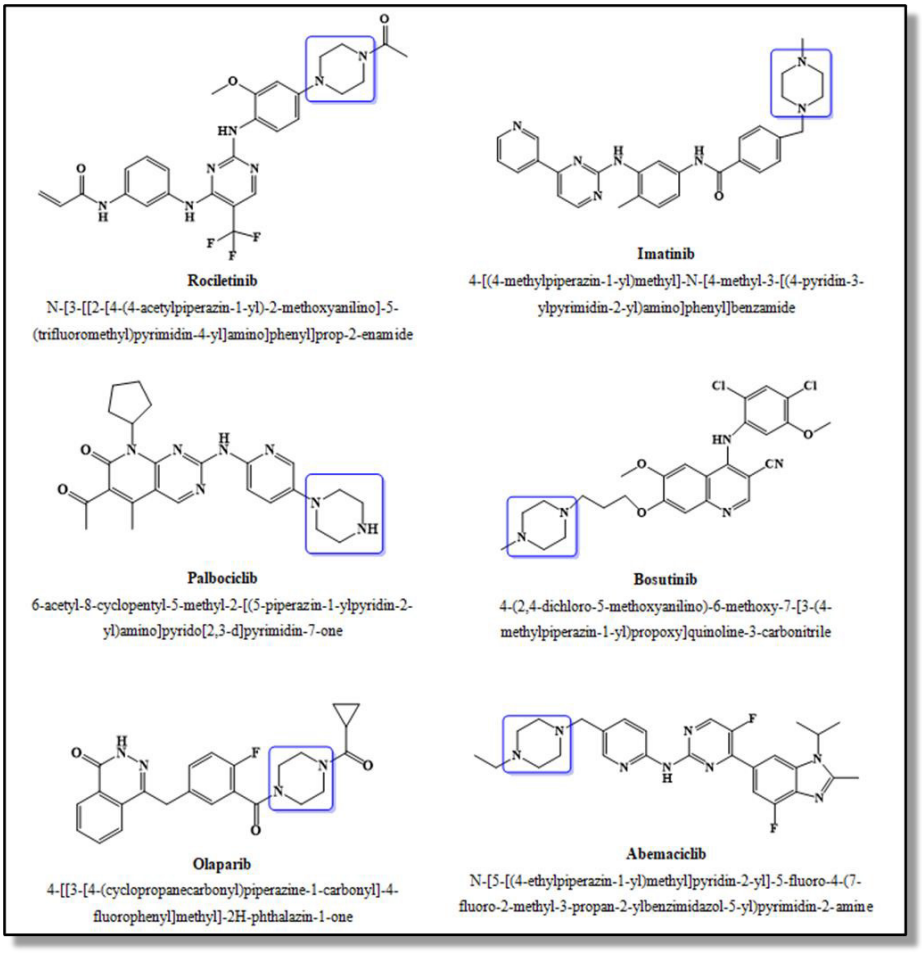

Figure 2: Some Anticancer Agents Containing Piperazine Core

Antidepressant Activity

Depression (clinical depression or major depressive disorder (MDD)) is a mental disorder that presents with symptoms of loss of energy, sleep and appetite disturbances, and mood lability (Guerrera et al., 2020:857). This situation affects human life negatively for a long time. The data have shown that depression, which is a chronic disorder, can become more severe in the later stages and cause suicide (Kumar et al., 2021:1878). Two types of depression are known, unipolar and bipolar. Unipolar depression is a mood disorder that affects only one side of the brain. It usually begins in young adulthood and lasts for at least six months. Bipolar disorder, also known as manic-depressive disorder, is a psychological-psychiatric disorder that affects a person's mood, energy, concentration, and ability to perform daily activities. Factors that cause

depression include chemical imbalances in the brain, genetic transmission, and triggering factors (Sahu et al., 2023:106544). Depending on the state of depressive episodes, depression can be treated with medications or a combination of medication and psychotherapy (Gelenberg, 2010:15). In addition, the design and discovery studies of new and effective drugs that can minimize undesired side effects for the treatment of depression have gained momentum in recent years. From this point of view, the effects of N-substituted piperazines on the central nervous system (CNS) reveal the potential of the related compounds in the treatment of depression (Moreira et al., 2021:113066). Keeping these aspects in mind, this section of the study outlines some recent studies on the antidepressant effects and SAR analyses of N-substituted piperazines. The studies discussed are listed comparatively in Table 2 under the headings of aim, model, and findings. Also, some antidepressant agents containing piperazine core are depicted in Figure 3 with their chemical structures and IUPAC names.

Table 2: Some Selected Studies on the Antidepressant Activities of N-Substituted Piperazines

Aim	Model	Findings
To synthesize novel phenoxyalkyl or phenoxyethoxyethyl piperazine derivatives and to examine their pharmacological activities (Panczyk et al., 2018:2039)	* Receptor studies * In vivo testing * Molecular modeling	11 new compounds were synthesized via multi-step chemical synthesis and studied in vivo for their antidepressant-like and anxiolytic-like properties. Nine of the synthesized derivatives were found to exhibit anxiolytic activity. Lipophilicity ($logP_{ow}$) estimates were made for each derivative from the results of in silico studies. In the light of the findings, it can be said that the values are sufficient to show activity in the central nervous system. It was determined that 1-[3-(2,4,6-trimethylphenoxy) propyl]-4-(4-methoxyphenyl) piperazine dihydrochloride derivative showed both anxiolytic and anticonvulsant activity in mice.
To design and to synthesize LQFM104, a piperazine derivative, as an antidepressant and antianxiety precursor and to investigate its activity behaviors (Silva et al., 2018:546)	* Open field test (OFT) * Elevated plus maze test (EPM) * Forced swimming test (FST) * Tail suspension test (TST) * Receptor studies * Statistical analysis	The synthesis of LQFM104 and the structure elucidation studies have been successfully completed. According to the research findings, the newly synthesized piperazine derivative showing both anti-anxiety and antidepressant-like activities provides the properties sought in new psychoactive drugs.
To synthesize new aralkyl piperazine and piperidine derivatives and to examine their antidepressant activities (Gu et al., 2019:126703)	* Receptor studies * Forced swimming test (FST) * Tail suspension test (TST)	Within the scope of the study, 14 new derivatives containing different substituents were synthesized. It was determined that 5-fluoro-3-(3-(4-(5-fluoro-[1,1'-biphenyl]-2-yl) piperidin-1-

		yl) propyl)-1H-indole showed the strongest effect in in vivo tests compared to other derivatives.
To design and synthesize novel xanthone derivatives containing piperazine moiety and to examine their activities in the CNS (Zelaszczyk et al., 2019:126679)	* Receptor studies * Forced swimming test (FST) * Four plate test (FPT) * In Silico ADME analysis	In summary, it was concluded that chlorine and methoxy substitution in the xanthone moiety of the synthesized compounds were determinants of the activity.
To evaluate the activity of the newly synthesized LQFM212 compound (piperazine derivative) in the CNS. (Moreira et al., 2020:112827)	* Receptor studies * Elevated plus maze test (EPM) * Light-dark box (LDB) test * Molecular Docking * Statistical analysis	As a result, the research findings determined that the compound LQFM212 (2,6-di-tert-butyl-4-((4-(2-hydroxyethyl) piperazin-1-yl) methyl) phenol) could be an effective prototype in the treatment of anxiety. Besides, molecular docking studies revealed that the related molecule has more interaction with the $GABA_A$ receptor.
To evaluate antidepressant activity of LQFM212 and to investigate its side effects (Moreira et al., 2021:113066)	* Forced swimming test (FST) * ELISA measurements of BDNF * Quantification of GSH levels in the liver * Determination of liver and kidney function indicators * Statistical analysis	According to the research findings, the LQFM212 molecule shows antidepressant-like activity, most likely involving monoaminergic pathways.
To synthesize piperazine derivatives containing oxadiazole moiety and evaluate their bioactivity (Sahu et al., 2021:1878)	* Forced swimming test (FST) * Tail suspension test (TST) * Molecular Docking	Effective results were obtained in the in vivo tail suspension test investigations of the derivatives containing phenyl and methyl substituents among the synthesized compounds. In addition, molecular docking studies predicted stable complex formation between MAO-A and related derivatives. Therefore, it is concluded that among the synthesized derivatives, there are promising candidates for further studies.
To synthesize benzenesulfonyl piperazine derivatives and to investigate their pharmacological activities (Nandi et al., 2023:134671)	* hMAO inhibition study * Reversibility studies * Forced swimming test (FST) * Tail suspension test (TST) * In Silico ADME analysis * Molecular Docking	Within the scope of the study, sixteen new derivatives were synthesized and their structures were characterized. In vivo investigations determined that the two synthesized derivatives exhibited potent antidepressant activity ($p < 0.05$) in FST and TST tests.
To synthesize indole-2-carbonyl piperazine urea derivatives and to examine its effects in the treatment of depression and pain (Shang et al., 2022:106031)	* Molecular dynamics analysis * Acute safety assessment * Liver microsome stability analysis *In vivo antidepressant activity analysis	Thirty of the thirty-nine new compounds synthesized in the study have a piperazine moiety in their structure. Pharmacological tests revealed the discovery of a derivative with higher selectivity and stronger activity compared to BIA 10-2474 used as reference substance. There are 5-Cl, -CH_3, and 3-pyridyl groups as substituents in the structure of abovementioned derivative. SAR analyses revealed that

		the related compound could be evaluated as an effective lead compound for further research in the treatment of depression and pain.
To synthesize a series of new aryl piperazine derivatives and to evaluate pharmacological activities (Penjisevic et al., 2023:104636)	* In Silico ADMET analysis * Molecular Docking * Cytochrome P450 site of metabolism analysis * 5-HT_{1A} receptor affinity	Eight of the synthesized derivatives caused a remarkable increase in 5-HT_{1A} affinity. The results of in silico ADMET analysis suggested that some compounds may not be suitable as drug candidates due to their toxicity.
To synthesize a series of compounds containing arylpiperazine scaffolds and 5-oxygen-substituted oxoisoaporphine moieties and to evaluate pharmacological activities (Sun et al., 2022:13385)	* Molecular Docking * In vitro/in vivo toxicity analysis * Neurocytoprotective Effects * Forced swimming test (FST) * Tail suspension test (TST) * Novel Tank Test (NTT) * Open-Field Test (OFT)	15 new compounds were synthesized and their structures were elucidated by various spectroscopic methods. According to the results of bioactivity analysis, most of the synthesized compounds did not exhibit remarkable cytotoxic activity to SH-SY5Y, PC12 and L02. On the other hand, it was determined that the derivative with a 5-carbon linker between arylpiperazine and oxoisoaporphine and a fluorine substituent on the phenyl ring showed antidepressant activity in in vitro tests. Molecular docking studies also support these findings. Therefore, it can be stated that the mentioned derivative is a promising candidate in this field.

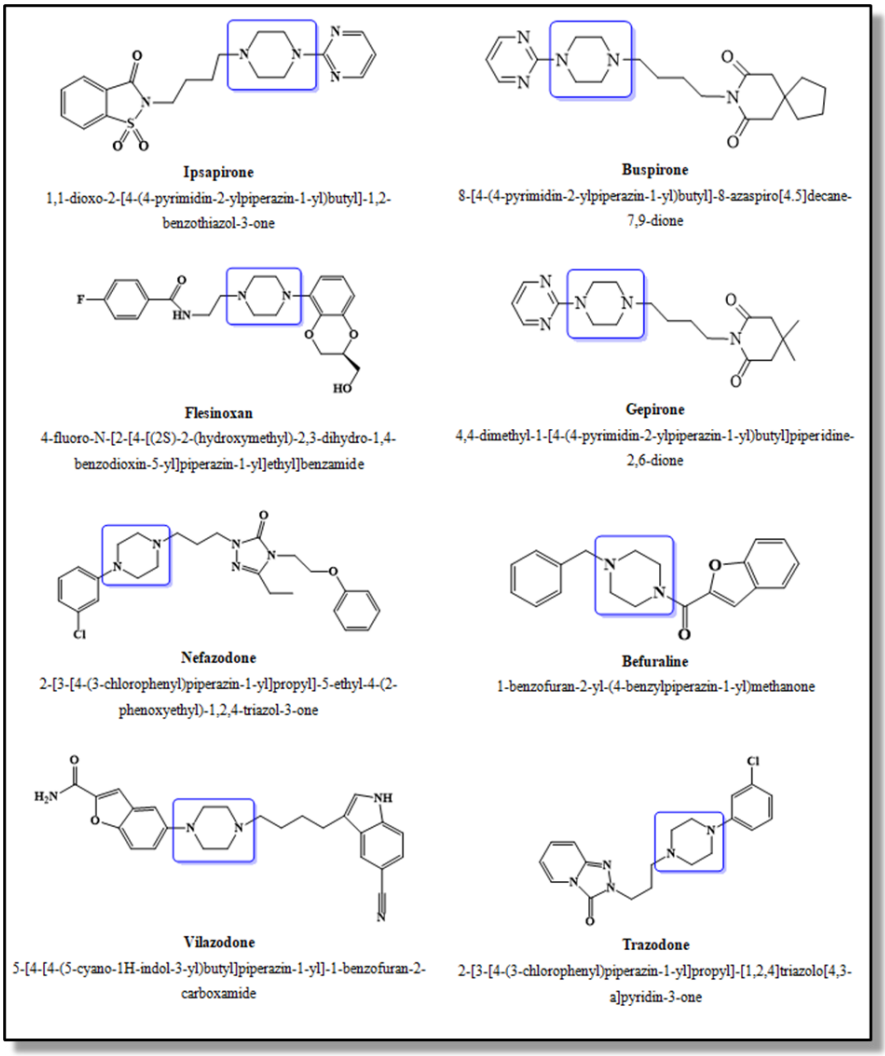

Figure 3: Some Antidepressant Agents Containing Piperazine Core

CONCLUSIONS

It can be expressed that the first step of the drug discovery process is the design stage. During the design stage, molecules that have the potential to exhibit activity in accordance with the main target are screened. In this context, hybridization studies and/or studies to determine structure-activity relationships guide the development of new bioactive molecules. Therefore, interest in these issues has increased considerably in recent years. Herein, inspired by the success of N-substituted piperazine derivatives in pharmacological activities, some recent studies on their anticancer and antidepressant effects and SAR

properties were discussed comparatively. In the studies, it is remarkable that computational methods are used as well as in vivo and in vitro analyses. Although the information obtained from computational methods cannot replace the experimental knowledge of medicinal chemistry, it can provide new perspectives for effective structural alterations. Moreover, the approaches mentioned in the studies can be a source of inspiration for researches in similar fields. We hope that this study, which emphasizes the role of the piperazine core in the development of new drug candidates against cancer and depression, will guide further research.

REFERENCES

Ahmed, A., Molvi, K. I., Nazim, S., Baig, I., Memon, T., and Rahil, M. (2012). The importance of six membered saturated nitrogen containing ring in psychological disorders. *Journal of Chemical and Pharmaceutical Research*, 4(1), 872-880.

Akkoç, M.K., Yüksel, M.Y., Durmaz, I., and Atalay, R.C. (2012). Design, synthesis, and biological evaluation of indole-based 1,4-disubstituted piperazines as cytotoxic agents. *Turkish Journal of Chemistry*, 36, 515-525.

Ambala, S., Thumma, V., Mallikanti, V., Aitha, S., Matta, R., and Pochampally, J. (2023). Design, synthesis, and cytotoxicity of some new benzimidazole-piperazine conjugate analogues against human breast adenocarcinoma. *ChemistrySelect,* 8, e202302393.

Bray, F., Ferlay, J., Soerjomataram, I., Siegel, R.L., Torre, L.A., and Jemal, A. (2018). Global cancer statistics 2018: GLOBOCAN estimates of incidence and mortality worldwide for 36 cancers in 185 countries. *CA: A Cancer Journal for Clinicians*, 68, 394-424.

Bugaenko, D.I. (2017). 1,4-Diazabicyclo [2.2.2] octane in the synthesis of piperazine derivatives (microreview). *Chemistry of Heterocyclic Compouds*, 53, 1277–1279.

Chandrika, N.T., Shrestha, S.K., Ngo, H.X., Tsodikov, O.V., Howard, K.C., and Garneau-Tsodikova, S. (2018). Alkylated piperazines and piperazine-azole hybrids as antifungal agents, *Journal of Medicinal Chemistry*, 61, 158–173.

Chen, F., Zhang, L., Qiang, L., Yang, Z., Wu, T., Zou, M., Tao, L., You, Q., Li, Z., Yang, Y., and Guo, Q.L. (2010). Reactive oxygen species-mitochondria pathway involved in LYG-202-induced apoptosis in human hepatocellular carcinoma HepG2 cells. *Cancer Letters*, 296, 96–105.

Chen, Y., Pan, W., Ding, X., Zhang, L., Xia, Q., Wang, Q., Chen, Q., Gao, Q., Yan, J., Lesyk, R., Tang, Z., and Han, X. (2023). Design, synthesis, and anticancer evaluation of nitrobenzoxadiazole-piperazine hybrids as potent pro-apoptotic agents. *Tetrahedron,* 138, 133393.

Elliott, S. (2011). Current awareness of piperazines: pharmacology and toxicology. *Drug Testing and Analysis*, 3, 430–438.

Gao, H., Zhang, X., Pu, X.J., Zheng, X., Liu, B., Rao, G.X., Wan, C.P., and Mao, Z.W. (2019). 2-Benzoylbenzofuran derivatives possessing piperazine linker as anticancer agents. *Bioorganic & Medicinal Chemistry Letters*, 29, 806–810.

Gelenberg, A. J. (2010). A review of the current guidelines for depression treatment. *The Journal of Clinical Psychiatry*, 71(7), 26478.

Gu, Z.S., Wang, W.T., Qian, H., Zhou, A.N., Sun, H.B., Zhang, Q.W., and Li, J.Q. (2019). Synthesis and antidepressant effect of novel aralkyl piperazine and piperidine derivatives targeting SSRI/5-HT_{1A}/5-HT_7. *Bioorganic & Medicinal Chemistry Letters*, 29, 126703.

Guerrera, C.S., Furneri, G., Grasso, M., Caruso, G., Castellano, S., Drago, F., Di Nuovo, S. and Caraci, F. (2020). Antidepressant drugs and physical activity: A possible synergism in the treatment of major depression? *Frontiers in Psychology*, 11:857.

Hu, L., Fan, M., Shi, S., Song, X., Wang, F., He, H., and Qi, B. (2022). Dual target inhibitors based on EGFR: promising anticancer agents for the treatment of cancers (2017-). *European Journal of Medicinal Chemistry*, 227, 113963.

Ibezim, E., Duchowicz, P.R., Ortiz, E.V., and Castro, E.A. (2012). QSAR on aryl-piperazine derivatives with activity on malaria. *Chemometrics and Intelligent Laboratory Systems*, 110, 81–88.

Jagadeesan, S., and Karpagam, S. (2023). Novel series of N -acyl substituted indole based piperazine, thiazole and tetrazoles as potential antibacterial, antifungal, antioxidant and cytotoxic agents, and their docking investigation as potential Mcl-1 inhibitors. *Journal of Molecular Structure*, 1271, 134013.

Kumar, R.R., Sahu, B., Pathania, S., Singh, P.K., Akhtar, M.J., and Kumar, B. (2021). Piperazine, a key substructure for antidepressants: its role in developments and structure-activity relationships. *ChemMedChem*, 16, 1878–1901.

Migliore, M., Pontis, S., Fuentes de Arriba, A.L., Realini, N., Torrente, E., Armirotti, A., Romeo, E., Di Martino, S., Russo, D., Pizzirani, D., Summa, M., Lanfranco, M., Ottonello, G., Busquet, P., Jung, K.-. M., Garcia-Guzman, M., Heim, R., Scarpelli, R., and Piomelli, D. (2016). Second-generation non-covalent NAAA inhibitors are protective in a model of multiple sclerosis, *Angewandte Chemie*, 128, 11359–11363.

Mishra, C.B., Mongre, R.K., Kumari, S., Jeong, D.K., and Tiwari, M. (2017) Novel triazole-piperazine hybrid molecules induce apoptosis via activation of the mitochondrial pathway and exhibit antitumor efficacy in osteosarcoma xenograft nude mice mode. *ACS Chemical Biology*, 12, 753−768.

Moreira, L.K., Brito, A.F., Fontana, C., Carvalho, F.S., Sanz, G., Vaz, B.G., Lião, L.M., Rocha, F.F., Verli, H., Menegatti, R., and Costa, E.A. (2020).

Neuropharmacological assessment in mice and molecular docking of piperazine derivative LQFM212. *Behavioural Brain Research*, 394, 112827.

Moreira, L.K.S., Brito, A.F., Silva, D.M., Siqueira, L., Silva, D.P.B., Cardoso, C.S., Florentino, I.F., Carvalho, P.M.G., Ghedini, P.C., Menegatti, R., and Costa, E.A. (2021). Potential antidepressant-like effect of piperazine derivative LQFM212 in mice: Role of monoaminergic pathway and brain-derived neurotrophic factor. *Behavioural Brain Research*, 401, 113066.

Mukherjee, D.E., Mukhopadhyay, A., Shridhara, K.B., Shridhara, A.M., and Rao, K.S. (2014). Synthesis, characterization and anticonvulsant activity of substituted 4-chloro-2-(4-piperazin-1-yl) quinazolines. *International Journal of Pharmaceutical Sciences*, 6, 567–571.

Nagendra Prasad, H.S., Ananda, A.P., Sumathi, S., Swathi, K., Rakesh, K.J., Jayanth, H.S., and Mallu, P. (2022). Piperazine selenium nanoparticle (Pipe@SeNP's): A futuristic anticancer contender against MDA-MB-231 cancer cell line. *Journal of Molecular Structure*, 1268, 133683

Nalçaoğlu, A., Sarı, C., Değirmencioğlu, I., and Celep Eyüpoğlu, F. (2022). Novel piperazine-substituted silicon phthalocyanines exert anti-cancer effects against breast cancer cells. *Photodiagnosis and Photodynamic Therapy*, 37, 102734

Nandi, N.K., Bhatia, R., Saini, S., Rawat, R., Sharma, S., Raj, K., Rangra, N., and Kumar, B. (2023). Design, synthesis, pharmacological and in silico screening of disubstituted-piperazine derivatives as selective and reversible MAO-A inhibitors for treatment of depression. *Journal of Molecular Structure*, 1276, 134671.

Panczyk, K., Pytka, K., Jakubczyk, M., Rapacz, A., Sałat, K., Furgała, A., Siwek, A., Głuch-Lutwin, M., Grybos, A., Słoczynska, K., Pekala, E., Zmudzki, P., Bucki, A., Kołaczkowski, M., Zelaszczyk, D., Marona, H., and Waszkielewicz, A.M. (2018). Synthesis and activity of di- or trisubstituted N-(phenoxyalkyl)- or N-{2-[2-(phenoxy)ethoxy]ethyl}piperazine derivatives on the central nervous system. *Bioorganic & Medicinal Chemistry Letters*, 28, 2039–2049.

Patel, K.B., Mukherjee, S., Bhatt, H., Rajani, D., Ahmad, I., Patel, H., and Kumari, P. (2023). Synthesis, docking, and biological investigations of new coumarin-piperazine hybrids as potential antibacterial and anticancer agents. *Journal of Molecular Structure*, 1276, 134755.

Penjisevic, J.Z., Sukalovic, V.B., Dukic-Stefanovic, S., Deuther-Conrad, W., Andric, D.B., and Kostic´-Rajacic, S.V. (2023). Synthesis of novel 5-

HT_{1A} arylpiperazine ligands: Binding data and computer-aided analysis of pharmacological potency. *Arabian Journal of Chemistry*, 16, 104636.

Sahu, B., Bhatia, R., Kaur, D., Choudhary, D., Rawat, R., Sharma, S., and Kumar, B. (2023). Design, synthesis and biological evaluation of oxadiazole clubbed piperazine derivatives as potential antidepressant agents. *Bioorganic Chemistry*, 136 106544.

Samala, R., Nukala, S.K., Thirukovela, N. S., Dasari G., and Bandari, S. (2022). One-Pot synthesis of some new phthalazine-piperazine-1,2,4-oxadiazole hybrids: anticancer evaluation, molecular docking and ADMET studies. *Polycyclic Aromatic Compounds*, 1-18.

Schumacher, T.J., Sah, N., Palle, K., Rumbley, J., and Mereddy, V.R. (2023). Synthesis and biological evaluation of benzofuran piperazine derivatives as potential anticancer agents. *Bioorganic & Medicinal Chemistry Letters,* 93, 129425.

Sergeant, N., Vingtdeux, V., Eddarkaoui, S., Gay, M., Evrard, C., le Fur, N., Laurent, C., Caillierez, R., Obriot, H., Larchanché, P.E., Farce, A., Coevoet, M., Carato, P., Kouach, M., Descat, A., Dallemagne, P., Buée-Scherrer, V., Blum, D., Hamdane, M., Buée, L., and Melnyk, P. (2019). New piperazine multi-effect drugs prevent neurofibrillary degeneration and amyloid deposition, and preserve memory inanimal models of Alzheimer's disease. Neurobiology of Disease, 129, 217–233.

Shang, Y., Wang, M., Hao, Q., Meng, T., Li, L., Shi, J., Yang, G., Zhang, Z., Yang, K., and Wang, J. (2022). Development of indole-2-carbonyl piperazine urea derivatives as selective FAAH inhibitors for efficient treatment of depression and pain. *Bioorganic Chemistry*, 128, 106031.

Silva, D.M., Sanz, G., Vaz, B.G., Carvalho, F.S., Lião, L.M., Oliveira, D.M., Moreira, L.K.S., Cardoso, C.S., Brito, A.F., Silva, D.P.B., Rocha, F.F., Santana, I.G.C., Galdino, P.M., Costa, E.A., and Menegatti, R. (2018). Tert-butyl 4-((1-phenyl-1H-pyrazol-4-yl) methyl) piperazine-1-carboxylate (LQFM104)– New piperazine derivative with antianxiety and antidepressant-like effects: Putative role of serotonergic system. *Biomedicine & Pharmacotherapy*, 103, 546–552.

Solomon, V. R., Hu, C., and Lee, H. (2010). Design and synthesis of anti-breast cancer agents from 4-piperazinylquinoline: a hybrid pharmacophore approach. *Bioorganic & Medicinal Chemistry*, 18(4), 1563-1572.

Sun, X., Li, N., Zhong, P., Chen, L., and Sun, J. (2022). Development of MAO-A and 5-HT_{2A}R dual inhibitors with improved antidepressant activity. *Journal of Medicinal Chemistry*, 65, 13385−13400.

Tamayo, N. A., Norman, M.H., Bartberger, M.D., Hong, F.T., Bo, Y., Liu, L., Nishimura, N., Yang, K.C., Tadesse, S., Fotsch, C., Chen, J., Chmait, S., Cupples, R., Hale, C., Jordan, S.R., Lloyd, D.J., Sivits, G.,Van, G., and St. Jean, D.J. (2015). Small Molecule Disruptors of the Glucokinase–Glucokinase Regulatory Protein Interaction: 5. A Novel Aryl Sulfone Series, Optimization Through Conformational Analysis, *Journal of Medicinal Chemistry*, 58, 4462–4482.

Tugrak, M., Gul, H.I., Bandow, K., Sakagami, H., Gulcin, I., Ozkay, Y., and Supuran, C.T. (2019). Synthesis and biological evaluation of some new mono Mannich bases with piperazines as possible anticancer agents and carbonic anhydrase inhibitors. *Bioorganic Chemistry*, 90, 103095.

Wei, M.X., Zhou, Y.X., Lin, M., Zhang, J., and Sun, X. (2022). Design, synthesis and biological evaluation of rhein-piperazine-dithiocarbamate hybrids as potential anticancer agents. *European Journal of Medicinal Chemistry,* 241, 114651.

Żelaszczyk, D., Jakubczyk, M., Pytka, K., Rapacz, A., Walczak, M., Janiszewska, P., Pańczyk, K., Żmudzki, P., Słoczyńska, K., Marona, H., and Waszkielewicz, A.M. (2019). Design, synthesis and evaluation of activity and pharmacokinetic profile of new derivatives of xanthone and piperazine in the central nervous system. *Bioorganic & Medicinal Chemistry Letters,* 29, 126679.

Chapter 7

Investigation of Heavy Metal Interference Effects on Acetic Acid Quantification Method[1]

Türkan BÖRKLÜ BUDAK[2]

[1] This study was supported by Yıldız Technical University, Scientific Research Projects Coordination Office, project number FBA-2021-4720.

[2] Res. Assist. Dr.; Yildiz Technical University, Faculty of Art and Science, Departmant of Chemistry, Istanbul, Turkiye. turkanborklu@yahoo.com, ORCID No: 0000-0002-1294-2682

SUMMARY

Ethanoic acid, also known as acetic acid, is a compound with many different uses. Acetic acid with the chemical formula CH_3COOH is used in the plastics industry as well as in the food industry for preservative purposes with the code number E260. Acetic acid, or vinegar as it is called in the food industry, actually has a high cost and a time-consuming process when obtained naturally. For this reason, it contains the possibility of fraudulent structures by mixing lower cost acids as impurities.

In line with the objectives of the study presented at this stage, it is aimed to detect fraudulent structures quickly and practically with a single potentiometric titration. During this process, it was investigated whether heavy metal cations; Cu^{2+}, Ni^{2+}, Co^{2+}, Cd^{2+}, Fe^{3+} and Fe^{2+}, which may be present in the environment, have any interference effect.

In addition, the effect of vinegar types obtained from different sources and storage conditions on the limit of determination was investigated with different vinegar types obtained from the market. In this way, the method, which has a low limit of rapid determination and whose applicability is supported by experimental data, has been successfully studied.

Key words: Acetic acid, hydrochloric acid, vinegar, heavy metal.

1. INTRODUCTION

Acetic acid with the formula CH_3COOH is one of the smallest carboxylic acids in organic acids. The odour of pure acetic acid is quite sharp. It generally has a colourless or light yellow appearance. While its boiling point is 118 °C, its freezing point is -16,7 °C. It can be mixed with water at the desired ratio. It can be obtained by oxidation of carbohydrates through fermentation and can also be produced synthetically by petrochemical method (Santos et al., 2020). Acetic acid can be obtained by three main chemical processes. These methods can be listed as I. oxidation with n-butanol, II. methanol carbonylation and III. acetaldehyde oxidation (Cheryan et al., 1997).

Acetic acid is an important acid with many different industrial uses (Patil and Kulkarni, 2014). Latex is a raw material used in processes such as the manufacture of adhesives in the dye and textile industry (Shi et al., 2005). When the literature data are analysed, many current studies are found. For example, parts such as leaves, peels and seeds found in food process wastes were analysed and acetic acid was obtained from mango peels by evaluating their high degradation capacity. Thus, it has been possible to utilise solid wastes which are a big problem. In the mentioned publication, the titration method with sodium hydroxide, which is a classical method for determining the amount of acetic acid, was used (Jennifer et al., 2021; Giulia et al., 2021). In another study, acetic acid doped component is used in the polymerisation process to increase the elasticity of carbon fibre. Curing, strength effect and environmentally friendly recyclability effect were investigated. The strength effect was repeated with different trials containing acetic acid and could be increased from 47% to 89% (Mingfei et al., 2021). The effect of acetic acid containing impurities, which is among the objectives of the proposed project, has not been examined. With the method developed within the scope of the proposed project, studies can be examined with acetic acid solution, which is found to contain different amounts of strong acid.

Vinegar, a type of acetic acid used in the food industry, is an important fermentation product produced by acetic acid bacteria by fermentation of raw fruits and dates back to 3000 years ago, to the ancient Babylonian civilisation (Budak et al., 2014; Nakayama, 1959; Bourgeois and Barja, 2009). Thanks to its antioxidant properties, vinegar reduces the risk of disease by preventing the formation of free radicals (Gao et al., 2021). The positive effects of vinegars obtained by fermenting from different sources are also different. Total acidity effect is an important parameter in this context (Gong et al., 2021). In the aforementioned study, the effects of the organic acids contained in the vinegar obtained from rice on total acidity and thus on its utilisation were examined.

During the experiments, the total acidity was determined by titrimetric method using a standard solution of sodium hydroxide. Potentiometric titration with sodium formate, the conjugated base of acetic acid, is not available in the literature. However, a strong acid that may be present as an impurity in the total acidity can be elucidated in this way.

In fact, many different fermentation products that are desired to be produced need time (Hongbo et al., 2021). During this time, the amount of acetic acid that gives vinegar its sour flavour also changes. There is no method in the literature in which the analysis method within the scope of the project is studied by spiking vinegar samples obtained at different times. In another publication, vinegars obtained from many different sources such as pumpkin, wild plum, pear and cabbage were examined and their structures were tried to be elucidated by spectroscopic methods (Öztürk, 2021). In addition, the effect of the bottle containing the vinegar on the vinegar structure was examined and as a result, vinegar samples containing micro plastics were found (Pouran et al., 2021). However, it is obvious that these have negative effects on human health. Again, the results of the titration of the method to be developed in different types of bottles, vinegar samples obtained from different sources, impurity spiking and titration with conjugated base are also worthy of investigation.

Acetic acid, which has so many different uses, is a very expensive acid considering the market prices. For this reason, in order to reduce the cost, sometimes mixtures containing cheaper impurities can be made. In a previous study, potentiometric titration of acetic acid, hydrochloric acid mixture with sodium formate was carried out (Budak, 2005). However, the scope of this study is to investigate the effects of heavy metal interference on this mixture as single, double or triple mixtures and to investigate the existence of applications with vinegar samples of different structures obtained from the market.

2. EXPERIMENTAL

2.1. Materials and reagents

Sodium hydroxide, sodium acetate, hydrochloric acid and acetic acid used in the experiments were obtained from Sigma-Aldrich and all heavy metal solutions were obtained from Merck. Distilled water was obtained by using Millipore (USA) purification system. In addition, working solutions were prepared by diluting the stock acid and base solutions as necessary. pH measurements were carried out with pH 720 (inoLab) wtw series. All experiments were carried out at room temperature with magnetic stirrer.

2.2. Experimental Procedure

In order to examine the heavy metal interference effect, single additions were made from the solutions prepared at a concentration of 1000 mg/L. Cu^{2+}, Co^{2+}, Ni^{2+}, Fe^{3+}, Fe^{2+} and Cd^{2+} solutions were prepared at a concentration of 1000 mg/L by taking the required weights. Then HCl, CH_3COOH, NaOH and CH_3COONa solutions were prepared with a target concentration of 0.1 M. The actual concentrations were found by adjusting against NaOH determined using potassium hydrogen phthalate.

As mentioned in previous studies, mixtures of different amounts of CH_3COOH and HCl, which may be present as impurities, were prepared and titrated with CH_3COONa, the conjugated base of acetic acid, a weak acid. Again, as in the literature, the amount of strong acid was reduced and it was determined up to what percentage it could be determined.

In the ongoing studies, titrations were carried out by adding single, double and triple heavy metal mixtures in order to examine whether there is a heavy metal interference effect on this determination limit. In addition, the applicability to real vinegar samples was investigated and the effect of storage conditions was examined.

3. RESULTS AND DISCUSSION

3.1. Titrations of mixtures containing different amounts of impurities with conjugated base

Mixtures containing 0.0901 M CH_3COOH and different amounts of 0.0988 M HCl solutions were titrated with 0.0991 M CH_3COONa using a pH metre. The data obtained are shown in Figure 1 in accordance with the literature.

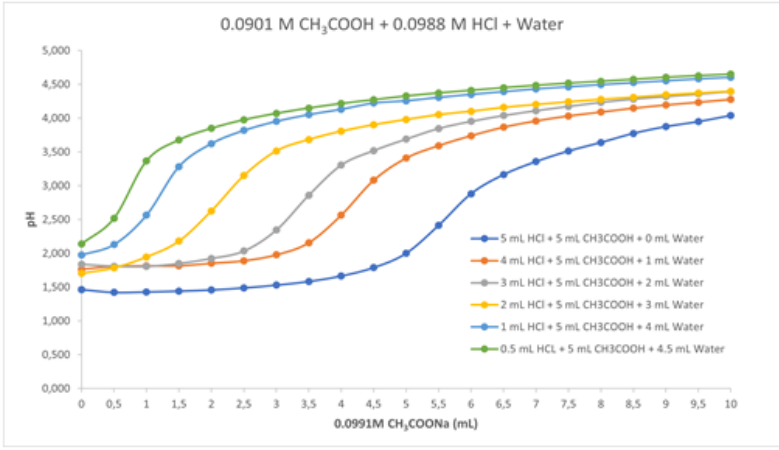

Figure 1: Titration of CH_3COOH solutions containing different amounts of impurity (HCl) with conjugated base.

Accordingly, although there is a single turning point involving the amount of strong acid, the method continues to give successful results in accordance with previous studies even if the strong acid ratio is reduced to approximately 9.10 %, as shown in the graph indicated by green dots.

3.2. Single analyses of heavy metal interference effect

It is foreseen that heavy metal impurities may sometimes be present in the environment, although it varies depending on places such as the areas that may arise from the use of acetic acid in different industrial areas. Even in these cases, in order to understand to what extent the method can indicate the turning point of the strong acid, the sensitivity of the method was examined by adding single heavy metal solutions as shown in Figure 2 and Figure 3.

As can be seen in Figure 2, the turning point cannot be followed during the titration of the mixture in which 0.5 mL of 0.0988 M HCl solution to which Cu^{2+} cation is added as an impurity. At this point, Cu^{2+} had a negative interference effect, while no negative effect was observed on the titration of

other acid mixtures. When the effects of Ni^{2+} and Fe^{3+} cations in Figure 2 are analysed, it can be seen that they do not have a negative effect on the slope points of the titration graph.

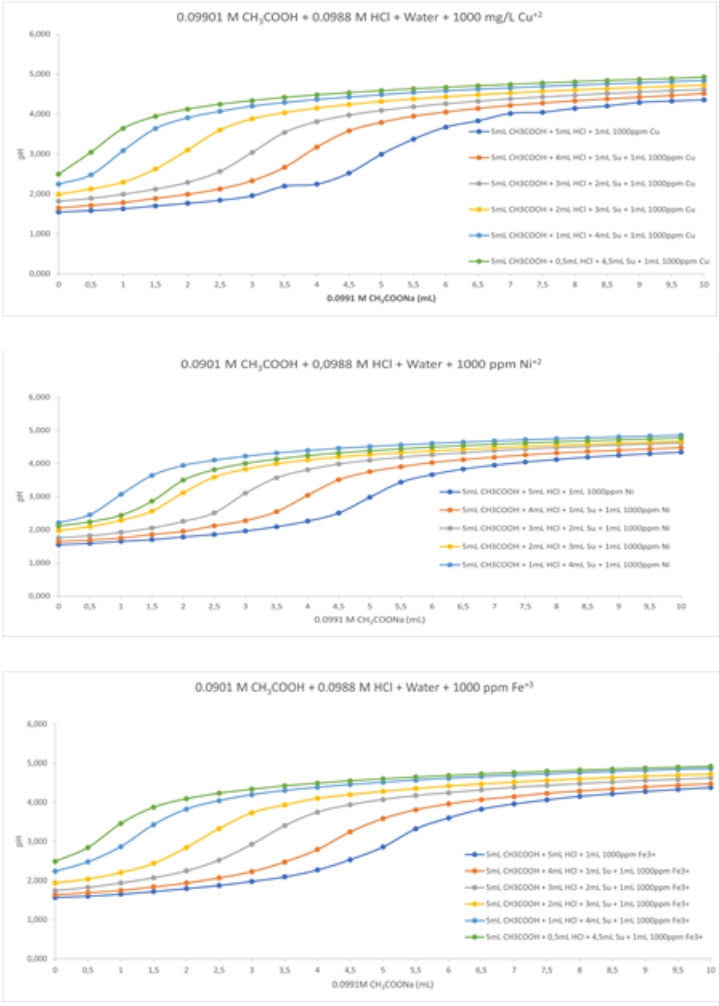

Figure 2: Investigation of Cu^{2+}, Ni^{2+} and Fe^{3+} interference effects on the studied method

When the data in Figure 3 are analysed, the turning points cannot be followed in the titration of the mixture in which 0.5 mL 0.0988 M HCl solution containing Fe^{2+} cation is added as an impurity and in the titration of the mixture containing 1 mL 0.0988 M HCl containing Co^{2+} cation. In both operating

curves, there are negative interference effects of Fe^{2+} and Co^{2+} cations, respectively, while no negative effect is observed in the titration of Cd^{2+} and other acid mixtures, and turning points equivalent to the curves shown in Figure 1 are observed.

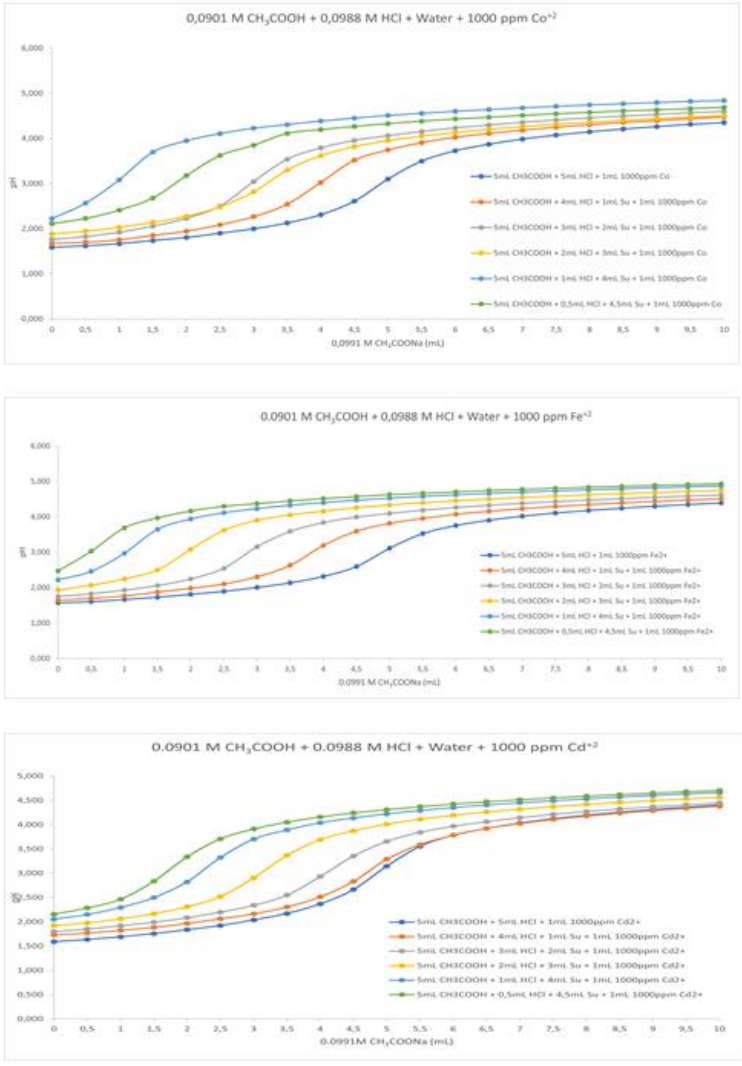

Figure 3: Investigation of Co^{2+}, Fe^{2+} and Cd^{2+} interference effects on the method

3.2. Investigation of interference effects of binary and ternary heavy metal mixtures

In order to see the effect of different environments that can be studied during the applications, the effects of binary and ternary heavy metal mixtures on the titration curve turning point were investigated. The data of the studies carried out for this purpose are shown in Figure 4 and Figure 5.

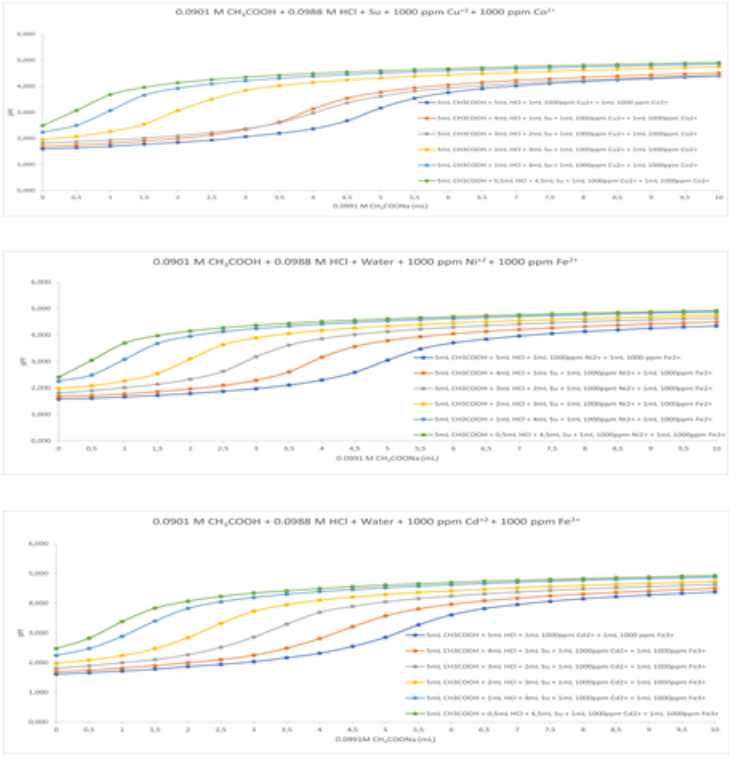

Figure 4: Investigation of the interference effects of Cu^{2+}- Co^{2+}, Ni^{2+}- Fe^{2+} and Cd^{2+}- Fe^{3+} binary metal mixtures on the studied method

As can be seen in Figure 4, although there is no turning point in the green-rected titration curves in which 0.5 mL of 0.0988 M HCl solution containing Cu^{2+}- Co^{2+} and Ni^{2+}- Fe^{2+} heavy metals from binary metal mixtures is added as impurity, the titration curves of the mixtures containing strong acid in other ratios can be observed positively. Again, it was observed that there was no problem in the interference effect containing Cd^{2+}- Fe^{3+} and the curves were in a determinable structure.

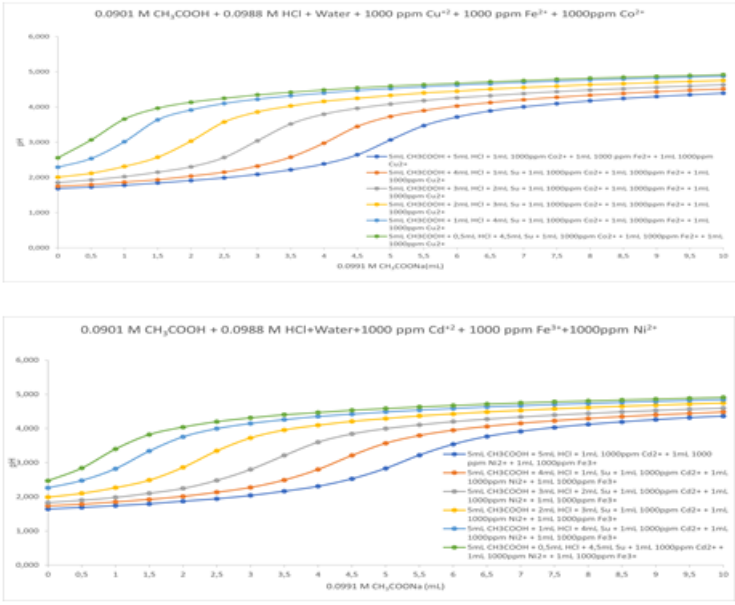

Figure 5: Investigation of the interference effects of Cu^{2+}- Fe^{2+}- Co^{2+}, Cd^{2+}- Fe^{3+}- Ni^{2+} ternary metal mixtures on the studied method

When the effects of the ternary metal mixtures in Figure 5 were examined, it was found that the turning point could not be observed only in the structure containing Cu^{2+}- Fe^{2+}- Co^{2+} in the acid mixture containing 0.0988 M, 0.5 mL HCl solution (green coloured curve). On the other hand, at other ratios of the same trimetal and interference effects containing Cd^{2+}- Fe^{3+}- Ni^{2+}, no problems occurred and the equivalent point indicating the amount of strong acid that may be an impurity could be successfully observed.

3.3. Real Sample Application

In order to find out whether different vinegar types and storage conditions affect the determination limit, the experiments were repeated using apple cider vinegar (in glass bottle), apple cider vinegar (in PET bottle), grape vinegar and white vinegar obtained from the market. The results obtained are shown in Figure 6.

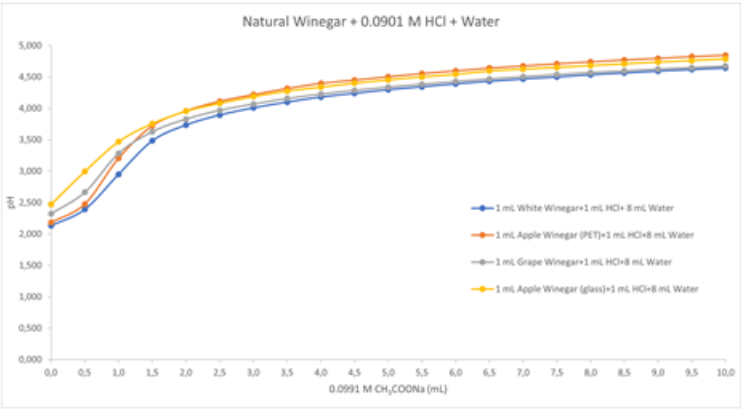

Figure 6: Real vinegar samples applications

When the titration data of apple cider vinegar (in glass bottle), apple cider vinegar (in PET bottle), grape vinegar and white vinegar samples in Figure 6 were analysed, it was concluded that only in the mixture with apple cider vinegar (in glass bottle), the turning indicating the amount of strong acid could not be observed, but in the other vinegars it could be successfully detected.

4. CONCLUSION

According to the results of the study, the determination of the amount of hydrochloric acid, which can be found as an impurity in acetic acid solutions, can be successfully determined even in environments that may cause some interference effects. Accordingly, heavy metal interference effects including Cu^{2+}, Co^{2+}, Ni^{2+}, Fe^{3+}, Fe^{2+} and Cd^{2+} cations, which may be present in the medium in single, double or triple form, were analysed. As a result, except for a few titrations described above, the study has successfully achieved its objectives and the turning point that will indicate the amount of hydrochloric acid can be seen.

In addition, according to the titration data with apple cider vinegar (in glass bottle), apple cider vinegar (in PET bottle), grape vinegar and white vinegar samples produced from different sources obtained from the market, it was concluded that the method could be successfully applied, except for apple cider vinegar (in glass bottle). In addition, in terms of storage conditions, it is thought that it may be promising to repeat the experiments using a more dilute conjugated base for the analysis of the real vinegar sample in the glass bottle.

REFERENCES

Bourgeois, J.F., and Barja, F. (2009). The history of vinegar and of its acetification systems. Archives des Sci., 62 (2) 147–160.

Budak, H. (2005). Asit karışımlarının titrasyonla analizi. Yıldız Teknik Üniversitesi, Fen bilimleri Enstitüsü, Yüksek Lisans Tezi, İstanbul.

Budak, N. H., Aykin, E., Seydim, A. C., Greene, A. K., and Guzel-Seydim, Z. B. (2014). Functionalproperties of vinegar. J. FoodSci., 79 (5) 757–764.

Cheryan, M., Parekh, S., Shah, M., and Witjitra, K. (1997). Production of acetic acid by clostridium thermo aceticum, Adv. Appl. Microbiol., 43, 1-33.

Gao, H., Wang, W., Xu, D., Wang, P., Zhao, Y., Mazza, G., and Zhang, X. (2021). Taste-active indicator sand their correlation with antioxidant ağabeylity during the *Monascus* rice vinegar solid-state fermentation process. Journal of Food Composition and Analysis, (104) 104133.

Giulia, M., Alessandro, B., Alessia, A., and Francesca, B. (2021). Acetic acid bioproduction: The technological innovation change. Science of The Total Environment, (798), 149292.

Gong, M., Zhou, Z.L., Liu, S.P., Zhu, S.H., and Mao, J., (2021). Formation pathways and precursors of furfural during Zhenjiang aromatic vinegar production. Food Chem., 354 (2), 129503.

Hongbo, L., Xujia, M., Zhenbin, L., Long, X., Dan, X., Liangbin, H.,

Haizhen, M., and Xiaohui, Z. (2021). Accelerating vinegar aging by combination of ultrasonic and magnetic field assistance. Ultrasonics Sonochemistry, (78) 105708.

Jennifer, P.F., Dominica, D.M.D., Daisic, D.B., and Kathleen, J.L.D.S. (2021). Utilization of pesticide-free calamansi (Citrus microcarpa) and mango (Mangifera indica) peels for the production of acetic acid with potential industrial application. Bioresource Technology Reports, (15), 100806.

Mingfei, X., Zixin, L., Guohang , Z., Yajie, D., Chun, C., and Yaping, W. (2021). Recycling of carbon fiber-reinforced epoxy resin composite via a novel acetic acid swelling technology. Composites Part B: Engineering, (224), 109230.

Nakayama, T. (1959). Studies on acetic acid-bacteria I. Biochemical studies on ethanol Oxidation. J. Biochem. 46 (9) 1217–1225.

Öztürk, M. (2021) Evaluation of quality the pumpkin, wild plum, pear, cabbage traditional homemade vinegars using the spectroscopy and rheology methods. Spectrochimica Acta Part A: Molecular and Biomolecular Spectroscopy, 259, 119896.

Patil, K.D., and Kulkarni, B.D. (2014). Review of recovery methods for acetic acid from industrial waste streams by reactive distillation. J. Water Pollut. Purificat. Res., (1), 13–18.

Pouran, M., Milad, N., Kamyar, G., Mahsa, M., Ahmadreza, Y., and Hooshyar, H. (2021). Micro-plastic occurrence in bottled vinegar: Qualification,quantification and human risk exposure. Process Safety and Environmental Protection, (152) 404–413.

Santos, D.L.U., Dobladez, J.A.D., Mate, V.I.A., Torrellas, S.A., and Martinez, M.L. (2020). Recovery and purification of acetic acid from aqueous mixtures by simulated moving bed adsorption with methanol and water as desorbents. Separation and Purification Technology, (237), 116368.

Shi, Y., Fan, M., Li, N., Brown, R.C., and Sung, S. (2005). The recovery of acetic acid with sulfur dioxide. Biochem. Eng. J., (22), 207–210.

Chapter 8

Statistical Method of Color Substances Used in Medicines Determination

Güzide PEKCAN[1]

[1] Doç.Dr., Süleyman Demirel Üniversitesi, Fen-Edebiyat Fakültesi, Kimya Bölümü, guzideertokus@sdu.edu.tr, ORCID No: 0000-0001-9230-5634.

ABSTRACT

INTRODUCTION

Drugs are chemical preparations used in the prevention of disease or in the treatment of already existing disease with the use of auxiliary substances such as colorants together with their active ingredients (Kapucu vd., 2009). Colorants used as auxiliary substances in medicines are used to strengthen the natural color on the product, to increase the perception of the consumer and to restore the lost color of the product during production or to color the colorless product (Yurttagul ve Ayaz, 2008).

In this study, the color substances of titanium dioxide and indigotine were determined by the classical least squares method (CLS) (Dinç et al., 2002; 2005; 2007) by using spectrophotometric data from the drug tablet sample. Titanium dioxide, TiO2, is a substance that is also used as a pigment with a mineral structure (Berik, 2018). Indigotin is a pigment of natural origin obtained from the leaves of the "Indigofera Tinctoria" plant (Ceppioğlu and Yurdun, 2012).

1. MATERYAL VE METOT

In this study, UV/VIS spectrophotometry and chemometry methods were used to determine the color substances used on the outer surface of drugs. The obtained data were calculated with the Minitab 17 program. The UV – Vis spectra were determined using the UV 1700 PHARMASPEC SHIMADZU spectrophotometer equipped with a computer-controlled 1 cm long cell, and the spectrum values were applied to determine the amount of titanium dioxide used as color substances in medicines.

Chemicals of analytical purity were used in the experiments (in solution at 100 µg/mL). The chemicals used in the study (Table 1.) are also given.

Table 1. Chemicals used in the study and their formulas

Name of The Compound	**Formula of The Compound**	**Name of The Compound**	**Formula of The Compound**
Titanium dioxide	TiO_2	Indigotine	$C_{16}H_{10}N_2O_2$

In this study, spectra of titanium dioxide and indigotin substances were taken by spectrophotometric measurements, first one by one and then by artificial mixtures prepared in different ratios. As a final process, measurements were made for the determination of color substances used in medicines. The obtained data were evaluated by different chemometric methods. In the first step, the calibration (reset process) of the UV spectrophotometer device was carried out.

The calibration process was first performed against the air by leaving both cells blank. Then the same process was done by placing a blind sample prepared with our solvent in both light paths. In all readings, the blind is always prepared in this way. In order to eliminate the effects of interference during blind selection, solvent was preferred blindly. Color substances were determined and absorbance reading was performed.

2. RESULT

In order to determine the spectroscopic properties of color substances, solutions in the range of 2-10 µg/mL for titanium dioxide, 1-5 µg/mL for Indigotine were prepared and the relationship between absorbance-concentration of color substances was examined. Titanium dioxide gives maximum absorption at 220 nm and indigotine at 630 nm. (Figure 1. and Figure 2.).

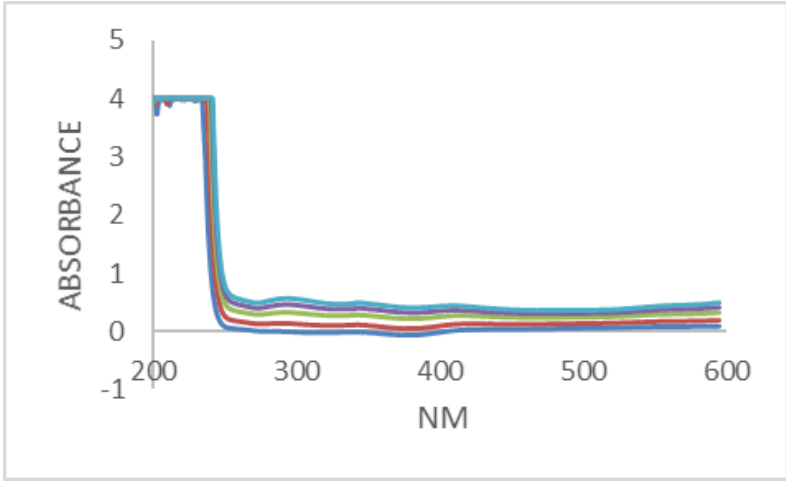

Figure 1. Absorption spectrum of the active ingredient of indigotine

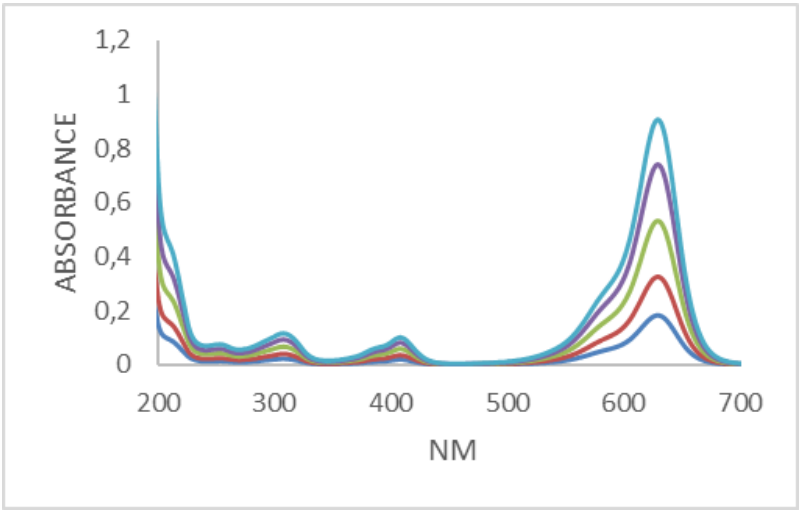

Figure 2. Absorption spectrum of the active ingredient of titanium dioxide

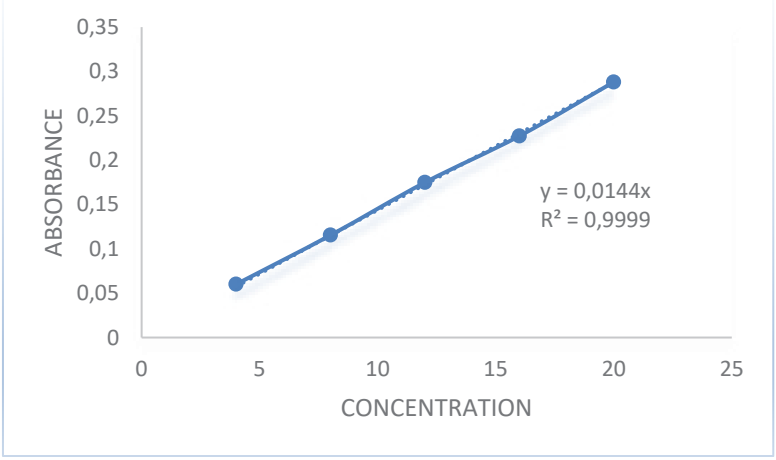

Figure 3. Absorbance-concentration graph of titanium dioxide material

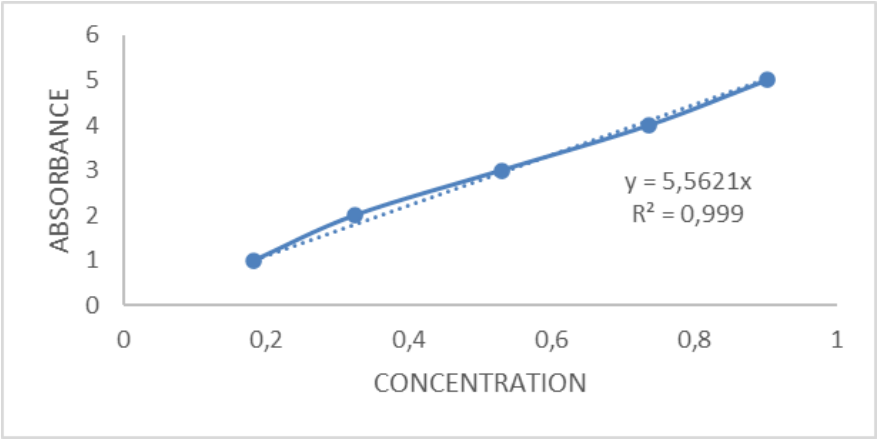

Figure 4. Absorbance-concentration graph of indigote

In the absorbance-concentration plots for Indigotin and Titanium dioxide, the linear relationship between absorbance-concentration (Sharma, 2017) is confirmed by the regression coefficient (Miao, 2018) being close to one (Figure 3., 4.).

The calculated recovery and relative standard deviation (BSS) values for each chemometric method are shown in Table 2. Accuracy and accuracy values have been checked. While calculating the concentrations against the additional concentrations, the cross-validation process was applied to prevent the error that may occur (Porfire, 2015 and Tarhan, 2017).

Table 2. Results calculated by CLS calibration of color substances in artificially prepared mixture

Mix No	Titanium dioxide Recovery %	Indigotine Recovery %
1	97,5	95,62
2	89,9	96,45
3	88,9	97,23
4	97,6	92,56
5	96,5	91,85
6	98,8	96,22
7	96,5	96,78
8	94,5	92,89
9	96,8	98,47
10	94,5	97,89
11	96,5	96,58
12	95,6	96,85
13	92,5	96,52
14	91,6	98,56
15	97,3	97,31
Mean (χ)	95,00	96,12
Relative Standard Deviation (RSD)	0,031	0,021

In this study, spectrophotometric analyzes of color substances used in drugs were performed and the findings obtained were calculated by classical least squares method from chemometric methods. UV spectra of titanium dioxide and Indigote color agents absorbance values were taken. For titanium dioxide and indigote, using the chemometric method, the method was statistically supported. When artificial mixtures are examined from the obtained results, the recovery values are large enough and the relative standard deviation values are small enough. This study is a preliminary study for the analysis of color substances used in drugs. In the next method, the classical least squares method can be applied to drug tablets and biological samples such as urine along with other chemometric methods.

BIBLIOGRAPHY

Berik, N. (2018). *Possible Damages of Using Titanium Dioxide and Nano Titanium Dioxide on Aquaculture*, Journal of Marine Science and Fisheries, 1(2): 59-65.

Ceppioglu S.K., Yurdun T. (2012). *In Vitro Testing for Genotoxicity of Indigoid Dyes by Comet Assay*, MUSBED, 2(3): 108-112.

Dinç, E. (2003). *Linear regression analysis and its application to the multivariate spectral calibrations for the multiresolution of a ternary mixture of caffeine, paracetamol and metamizol in tablets*, Journal of Pharmaceutical and Biomedical Analysis, 33:605-615, 2003.

Dinç, E., Baleanu, D. (2002). *Spectrophotometric quantitative determination of cilazapril and hydrochlorothiazide in tablets by chemometric methods*, Journal of Pharmaceutical and Biomedical Analysis, 30: 715-723.

Dinç, E., Özdemir, A., Baleanu, D. (2005). *Comparative study of the continuous wavelet transform, derivative and partial least squares methods applied to the overlapping spectra for the simultaneous quantitative resolution of ascorbic acid and acetylsalicylic acid in effervescent tablets*, Journal of Pharmaceutical and Biomedical Analysis, 37(3): 569-575.

Kapucu, E., Kahveci, H., Susam, Ö., Çanta, Y., (2009). *İlaçların ve Kozmetik Ürünlerin Geliştirilme Süreçleri ve Doğa Üzerine Etkileri.* Dokuz Eylül Üniversitesi Eğitim Fakültesi, 33s, 1-2.

Porfire, A., Muntean, D., Achim, M., Vlase, L., Tomuta, I. (2015). *Simultaneous Quantification of Simvastatin and Excipients in Liposomes Using Near Spectroscopy and Chemometry,* Journal of Pharmaceutical and Biomedical Analysis*,* v107, 40-49.

Sharma, D., Singh, R. Garg, R. (2017). *Development and validation of stability indicating UV spectro-photometric method for the estimation of benzydamine hydrochloride in bulk and in pharmaceutical dosage form: a novel analytical technique for conducting in-vitro quality control tests*, International Journal Of Pharmaceutical Sciences And Research, 9(2), 678-686.

Tarhan, I., Kara, A.A.I.H. (2017). *Quantitative Determination of Free Fatty Acids in Extra Virgin Olive Oils by Multivariate Methods and Fourier Transform Infrared Spectroscopy Considering Different Absorption Modes*, International Journal of Food Properties, 1-8.

Yurttagul, M., Ayaz, A. (2008)**.** *Katkı Maddeleri:Yanlıslar ve Doğrular.* Hacettepe Üniversitesi Sağlık Bilimleri Fakültesi Beslenme ve Diyetetik Bölümü, Ankara, 30 s.